ALLSENSORS 2025

The Tenth International Conference on Advances in Sensors, Actuators, Metering and Sensing

ISBN: 978-1-68558-273-9

May 18 - 22, 2025

Nice, France

ALLSENSORS 2025 Editors

Valentina Zhukova, University Basque Country, San Sebastian, Spain

Paulo Estevao Cruvinel, Brazilian Corporation for Agricultural Research, Brazil

ALLSENSORS 2025

Forward

The Tenth International Conference on Advances in Sensors, Actuators, Metering and Sensing (ALLSENSORS 2025), held between May 18th, 2025, and May 22nd, 2025, in Nice, France, continued a series of events covering related topics on theory, practice, and applications of sensor devices, techniques, data acquisition and processing, and on wired and wireless sensors and sensor networks.

Sensors and sensor networks have a great potential of providing diverse services to broad range of applications, not only in science and engineering, but equally importantly on issues related to critical infrastructure protection and security, healthcare, the environment, energy, food safety, and the potential impact on the quality of all areas of life.

We take here the opportunity to warmly thank all the members of the ALLSENSORS 2025 technical program committee, as well as all the reviewers. The creation of such a high-quality conference program would not have been possible without their involvement. We also kindly thank all the authors who dedicated much of their time and effort to contribute to ALLSENSORS 2025. We truly believe that, thanks to all these efforts, the final conference program consisted of top-quality contributions. We also thank the members of the ALLSENSORS 2025 organizing committee for their help in handling the logistics of this event.

We hope that ALLSENSORS 2025 was a successful international forum for the exchange of ideas and results between academia and industry for the promotion of progress in the field of sensors, actuators, metering, and sensing.

ALLSENSORS 2025 Chairs

ALLSENSORS 2025 Steering Committee
Michael Niedermayer, Berliner Hochschule für Technik, Germany
Paulo E. Cruvinel, Embrapa Instrumentation, Brazil
Matteo Tonezzer, CNR-IMEM, Trento, Italy
Sandrine Bernardini, Aix Marseille University, France
Almudena Rivadeneyra, Universidad de Granada, Spain
Laura Garcia, Universidad Politécnica de Cartagena, Spain
Sung Ho Cho, Hanyang University, South Korea

ALLSENSORS 2025 Publicity Chairs
José Miguel Jiménez, Universitat Politècnica de València, Spain
Francisco Javier Díaz Blasco, Universitat Politècnica de València, Spain
Ali Ahmad, Universitat Politècnica de València, Spain
Sandra Viciano Tudela, Universitat Politècnica de València, Spain
Laura Garcia, Universidad Politécnica de Cartagena, Spain

ALLSENSORS 2025
Committee

ALLSENSORS 2025 Steering Committee

Michael Niedermayer, Berliner Hochschule für Technik, Germany
Paulo E. Cruvinel, Embrapa Instrumentation, Brazil
Matteo Tonezzer, CNR-IMEM, Trento, Italy
Sandrine Bernardini, Aix Marseille University, France
Almudena Rivadeneyra, Universidad de Granada, Spain
Laura Garcia, Universidad Politécnica de Cartagena, Spain
Sung Ho Cho, Hanyang University, South Korea

ALLSENSORS 2025 Publicity Chairs

José Miguel Jiménez, Universitat Politècnica de València, Spain
Francisco Javier Díaz Blasco, Universitat Politècnica de València, Spain
Ali Ahmad, Universitat Politècnica de València, Spain
Sandra Viciano Tudela, Universitat Politècnica de València, Spain
Laura Garcia, Universidad Politécnica de Cartagena, Spain

ALLSENSORS 2025 Technical Program Committee

Francesco Aggogeri, University of Brescia, Italy
Otman Aghzout, National School of Applied Sciences of Tetouan, Morocco
Amin Al-Habaibeh, Nottingham Trent University, UK
Youssef Altherwy, Prince Sattam bin Abdulaziz University, Saudi Arabia
Darius Andriukaitis, Kaunas University of Technology, Lithuania
Federico Aromolo, Scuola Superiore Sant'Anna, Pisa, Italy
Piotr Artiemjew, University of Warmia and Mazury, Poland
Farzad Asgarian, University of Michigan, Ann Arbor, USA
Herve Aubert, Laboratory for Analysis and Architecture of Systems (LAAS-CNRS), France
Yang Bai, University of Maryland College Park, USA
Roberto Beghi, Università degli Studi di Milano, Italy
Artur Bejger, Maritime University of Szczecin, Poland
Roc Berenguer Pérez, TECNUN - Technological Campus of the University of Navarra, Spain
Sandrine Bernardini, Aix Marseille University, France
Mourad Bezzeghoud, University of Évora, Portugal
Xavier Boddaert, Mines Saint Etienne | Centre Microélectronique de Provence (CMP), France
Muhammad Ali Butt, Warsaw University of Technology, Poland
Maria Candelaria Hernandez Goya, Universidad de La Laguna, Spain
Juan Vicente Capella Hernández, Universitat Politècnica de València, Spain
Vítor Carvalho, 2AI-EST-IPCA / Algoritmi Research Centre - UM, Portugal
Paula María Castro Castro, Universidade da Coruña, Spain
Debashish Chakravarty, IIT Khaargpur, India
M Girish Chandra, TCS Research, India

Nan-Fu Chiu, National Taiwan Normal University,Taiwan
Sung Ho Cho, Hanyang University, South Korea
Susana Costa, University of Minho, Portugal
Paulo E. Cruvinel, Embrapa Instrumentation, Brazil
Luca Davoli, University of Parma, Italy
Udhaya Kumar Dayalan, Trane Technologies, USA
Marcos Antonio de Oliveira Junior, Federal University of Pelotas, Brazil
Francesco G. Della Corte, University of Napoli Federico II, Italy
Emiliano Descrovi, Polytechnic University of Turin, Italy
Chérif Diallo, Université Gaston Berger (UGB), Senegal
Toan Dinh, University of Southern Queensland, Australia
Yvan Duroc, University Claude Bernard Lyon 1, France
Raafat Elfouly, Rhode Island College, USA
Abdelali Elmoufidi, Sultan Moulay Slimane University, Morocco
Ahmed Fakhfakh, Digital Reasearch Center of Sfax, Tunisia
Olga A. Fedorova, A. N. Nesmeyanov Institute of Organoelement Compounds, Moscow, Russia
Attilio Frangi, Politecnico di Milano, Italy
Orlando Frazão, INESC TEC, Porto, Portugal
Kelum Gamage, University of Glasgow, UK
Ivan Ganchev, University of Limerick, Ireland / University of Plovdiv / IMI-BAS, Bulgaria
Jiechao Gao, University of Virginia, USA
Félix J. García Clemente, University of Murcia, Spain
Laura Garcia, Universidad Politécnica de Cartagena, Spain
Pietro Garofalo, Turingsense EU LAB s.r.l., Italy
Dominik Roy George, Eindhoven University of Technology, The Netherlands
Mojtaba Ghodsi, University of Portsmouth, UK
Patrick Goh, Universiti Sains Malaysia, Malaysia
Pranjol Sen Gupta, University of Texas at Arlington, USA
Sanaz Haddadian, Heinz Nixdorf Institute | University of Paderborn, Germany
Kuan He, Apple Inc., USA
Daniel Hill, Aston University, UK
Carmen Horrillo-Güemes, Grupo de Tecnología de Sensores Avanzados (SENSAVAN) | ITEFI-CSIC, Madrid, Spain
Pengpeng Hu, Vrije Universiteit Brussel, Belgium
Rui Igreja, Universidade NOVA de Lisboa, Portugal
Dimosthenis Ioannidis, CERTH/ITI, Thessaloniki, Greece
Ahmed Abu Ismaiel, Municipality of Abasan Al-Kabira, Gaza, Palestine
Nikos Kalatzis, Neuropublic S.A. / National Technical University of Athens, Greece
Grigoris Kaltsas, University of West Attica, Greece
Liuwang Kang, University of Virginia, USA
M-Tahar Kechadi, University College Dublin (UCD), Ireland
Anwesha Khasnobish, TCS Research, Kolkata, India
Jan Kubicek, VSB - Technical University of Ostrava, Czech Republic
Kai Lin, eBay Inc., USA
Paula Louro, ISEL/IPL & CTS/UNINOVA, Portugal
Vladimir Lukin, National Aerospace University, Kharkov, Ukraine
Dandan Ma, Northwestern Polytechnical University, China
Wei Ma, The Hong Kong Polytechnic University, Hong Kong

Stephane Maag, Télécom SudParis, France
Adnan Mahmood, Macquarie University, Australia
Marco Manso, PARTICLE Summary, Portugal
Jan Mareš, University of Chemistry and Technology, Prague, Czech Republic
Vincenzo Marletta, ST Microelectronics - Catania site, Italy
Nader Mbarek, University of Bourgogne Franche-Comté, France
Javier Medina Quero, University of Jaén, Spain
Massimo Merenda, CNIT - Consorzio Nazionale Interuniversitario per le Telecomunicazioni / University Mediterranea of Reggio Calabria, Italy
Lyudmila Mihaylova, University of Sheffield, UK
Carolina Miozzi, University of Rome Tor Vergata / RADIO6ENSE srl, Italy
Dhananjay Nahata, Rakuten, India
Igor Nazareno Soares, University of São Paulo, Brazil
Michael Niedermayer, Berliner Hochschule für Technik (BHT), Germany
Marek R. Ogiela, AGH University of Science and Technology, Krakow, Poland
Anna Ostaszewska-Liżewska, Warsaw University of Technology, Poland
Mehmet Akif Özdemir, Izmir Katip Celebi University, Turkey
Lorenzo Palazzetti, University of Perugia, Italy
Udayan Sunil Patankar, TalTech University of Technology, Tallinn, Estonia
D. R. Patil, Rani Laxmibai Mahavidyalaya Parola | North Maharashtra University, Jalgaon, India
Pablo Pérez García, Instituto de Microelectrónica de Sevilla, Spain
Vengadesh Periasamy, Low Dimensional Materials Research Centre (LDMRC) | Institute of Ocean, Earth and Sciences (IOES) | University of Malaya, Malaysia
Patrick Pons, CNRS-LAAS, Toulouse, France
Rüdiger Pryss, University of Würzburg, Germany
Parvaneh Rahimi, Institute of Electronic - and Sensor Materials | TU Bergakademie Freiberg, Germany
Càndid Reig, University of Valencia, Spain
Almudena Rivadeneyra, University of Granada, Spain
David Rivas-Lalaleo, Universidad de las Fuerzas Armadas ESPE, Ecuador
Alexandra Rivero García, Universidad de La Laguna, Spain
Christos Riziotis, National Hellenic Research Foundation, Greece
Bahram Djafari Rouhani, Université de Lille Sciences et Technologies, France
Gonzalo Sad, CIFASIS / CONICET / FCEIA | Universidad Nacional de Rosario, Argentina
Markus Santoso, University of Florida, USA
Iván Santos González, Universidad de La Laguna, Spain
Jagannathan Sarangapani, Missouri University of Science and Technology, USA
Sudipta Saha Shubha, University of Virginia, USA
Bruno M. C. Silva, University of Beira Interior, Portugal
Jan Steckel, Universiteit Antwerpen, Belgium
Mu-Chun Su, National Central University, Taiwan
Nur Syazreen Ahmad, Universiti Sains Malaysia (USM), Malaysia
Roman Szewczyk, Warsaw University of Technology, Poland
Alessandro Tognetti, University of Pisa, Italy
Matteo Tonezzer, CNR-IMEM, Trento, Italy
Anish Chand Turlapaty, Indian Institute of Information Technology Sri City, Chittoor, India
Sumarga K. Sah Tyagi, University of South Florida, USA
Sathishkumar V E, Sunway University, Malaysia
Harsh Vardhan, Vanderbilt University, USA

Diego Vergara, Universidad Católica Santa Teresa De Jesús De Ávila, Spain
Sudip Vhaduri, Fordham University, USA
Manuel Vieira, CTS-ISEL, Portugal
Manuela Vieira, ISEL-IPL/CTS-UNINOVA, Portugal
Stefanos Vrochidis, Information Technologies Institute - CERTH, Greece
Guang Wang, Florida State University, USA
Xianpeng Wang, Hainan University, China
Ulf Witkowski, South Westphalia University of Applied Sciences, Germany
Marcin Wozniak, Silesian University of Technology, Poland
Qingsong Xu, University of Macau, Macau, China
Murat Kaya Yapici, Sabanci University,Istanbul, Turkey
Sergey Yurish, Excelera, S. L. | IFSA, Spain
Kristina Žagar Soderžnik, Jožef Stefan Institute, Slovenia
Lan Zhang, AIST, Japan
Qingxue Zhang, Purdue School of Engineering and Technology, USA
Shichen Zhang, Michigan State University, USA
Shuai Zhao, Sun Yat-sen University, China
Jingjing Zheng, CISTER Research Centre, Portugal

Copyright Information

For your reference, this is the text governing the copyright release for material published by IARIA.

The copyright release is a transfer of publication rights, which allows IARIA and its partners to drive the dissemination of the published material. This allows IARIA to give articles increased visibility via distribution, inclusion in libraries, and arrangements for submission to indexes.

I, the undersigned, declare that the article is original, and that I represent the authors of this article in the copyright release matters. If this work has been done as work-for-hire, I have obtained all necessary clearances to execute a copyright release. I hereby irrevocably transfer exclusive copyright for this material to IARIA. I give IARIA permission or reproduce the work in any media format such as, but not limited to, print, digital, or electronic. I give IARIA permission to distribute the materials without restriction to any institutions or individuals. I give IARIA permission to submit the work for inclusion in article repositories as IARIA sees fit.

I, the undersigned, declare that to the best of my knowledge, the article is does not contain libelous or otherwise unlawful contents or invading the right of privacy or infringing on a proprietary right.

Following the copyright release, any circulated version of the article must bear the copyright notice and any header and footer information that IARIA applies to the published article.

IARIA grants royalty-free permission to the authors to disseminate the work, under the above provisions, for any academic, commercial, or industrial use. IARIA grants royalty-free permission to any individuals or institutions to make the article available electronically, online, or in print.

IARIA acknowledges that rights to any algorithm, process, procedure, apparatus, or articles of manufacture remain with the authors and their employers.

I, the undersigned, understand that IARIA will not be liable, in contract, tort (including, without limitation, negligence), pre-contract or other representations (other than fraudulent misrepresentations) or otherwise in connection with the publication of my work.

Exception to the above is made for work-for-hire performed while employed by the government. In that case, copyright to the material remains with the said government. The rightful owners (authors and government entity) grant unlimited and unrestricted permission to IARIA, IARIA's contractors, and IARIA's partners to further distribute the work.

Table of Contents

Reducing the Dead Zone Time Effect of Actuators in Sensor-Based Agricultural Sprayers under S-shaped Functions Gain Scheduling Management of a Generalized Predictive Control (GPC) Strategy

Deniver R. Schutz*,†, Vilma A. Oliveira†, Paulo E. Cruvinel*

*Embrapa Instrumentation
Brazilian Agricultural Research Corporation, São Carlos, SP, Brazil
† Department of Electrical and Computer Engineering
São Carlos School of Engineering
University of São Paulo, São Carlos, SP, Brazil
Email: deniver@usp.br, voliveira@usp.br, paulo.cruvinel@embrapa.br

***Abstract*—This paper presents a study on the relationship between sensors, control systems and actuators for agricultural spraying. Sensors associated with appropriate control systems can be used to support decision-making processes for nozzles in relation to the correct application of pesticides. In such a context, results related to a comparison were evaluated considering not only an adaptive generalized predictive control based on both fuzzy and sigmoid-based strategies for scheduling management but also the enhancement of the dead zone management improving actuators performance in relation to the nozzles stitching's processes. These systems involving sensors, controllers and switching are essential for the automation of agricultural sprayers, especially for those that work with variable rate application, in management based on precision agriculture. A Sigmoid-based Generalized Predictive Control (SGPC) is proposed for flow rate regulation in agricultural pesticide sprayers. Evaluated against conventional Fuzzy Logic-based GPC (FGPC), the SGPC shows reduced Integral Absolute Error (IAE) and faster rise time despite higher overshoot in certain scenarios. Results indicate enhanced tracking accuracy and dynamic response compared to traditional fuzzy logic approaches. This framework demonstrates potential for improving precision in agricultural spraying systems. Such results can be valuable for the current machinery agricultural industry, which needs to improve productivity and quality gains and reduce negative externalities in favor of food security and sustainability.**

Keywords-Agricultural sensors; Agriculture actuators; Predictive controller; Agricultural sprayers; Precision agriculture.

I. Introduction

Pesticide application using agricultural sprayers is traditionally performed at a constant rate (liters per hectare), independent of the spatial variability in pest and disease density into a crop field. This approach often leads to inefficiencies, as it does not account for localized needs, potentially resulting in over-application or even an under-application of chemicals [1].

Considering precision agriculture applications, the Variable Rate Application (VRA) systems leverage prescription maps, sensor data, and real-time actuator adjustments to tailor pesticide application rates based on the specific spatial distribution of pests and diseases across one crop agricultural field. By dynamically controlling flow rate and pressure, VRA enhances precision and reduces losses, aligning with the principles of precision agriculture [2].

Effective control of flow rate and pressure in agricultural spraying systems is critical for multiple reasons. Accurate flow regulation ensures that the correct amount of pesticide can be applied, reducing production costs and minimizing environmental impact. Similarly, precise pressure control improves spray quality by optimizing droplet size and distribution, which directly influences the effectiveness of the application. In addition, together with these factors, one may find a way to contribute to minimizing resource losses, enhancing application efficiency, and promoting sustainable farming practices [3].

The reliability of instruments responsible for monitoring flow and pressure, such as flowmeters and pressure sensors, as well as that regulating system performance, such as proportional valves, is critical. Malfunctions in these components can lead to significant errors in pesticide application, including either over-application, which increases costs and environmental risks, or under-application, which compromises pest control. Such inaccuracies not only jeopardize crop health but also can raise the risk of contaminating neighboring ecosystems due to drift or runoff [1].

From the perspective of automatic control, the performance of a spraying system can be evaluated based on parameters such as overshoot, steady-state error, rise time, and settling time. Issues such as overshoot and a high positive steady-state error are associated with overapplication, a phenomenon in which the applied volume exceeds the desired rate. This leads to waste of inputs, increased operational costs, and negative environmental impacts. On the other hand, an elevated rise time combined with a negative steady-state error can result in underapplication, compromising the effectiveness of phytosanitary treatments and negatively affecting crop development [4] [5].

In fact, the regulation of flow rate and pressure in agricultural sprayers are predominantly achieved using the Proportional-Integral-Derivative (PID) controllers. However, actuator control valves are inherently nonlinear systems, which can impair the performance of linear controllers, such as PID or even a Generalized Predictive Control (GPC) in regulating application rates [6]–[8].

Courtesy of IARIA Board and IARIA Press. Original source: ThinkMind Digital Library https://www.thinkmind.org

On the other hand, advanced control strategies, such as those leveraging adaptive algorithms, can further enhance sprayer system reliability and adaptability to varying field conditions. Recent works have explored the use of Artificial Neural Networks (ANNs) to introduce non-nonlinearities into GPC strategies. For instance, [9] and [10] investigate ANNs for modeling the dynamic behaviors and adapting to changing conditions and disturbances. However, the use of ANNs can be challenging due to the extensive data requirements for training.

In [11], an adaptive GPC controller is introduced, discrete-time fuzzy model with parameter estimation. Additionally, in [12], where a predictor error approach based on the recursive least squares method is proposed for microclimatic control in a fan-ventilated tunnel greenhouse. In [5], results are presented utilizing fuzzy logic for scheduling the parameters λ and δ of the GPC controller.

In this paper, a study is presented replacing a fuzzy logic based GPC by a sigmoid function to simplify gain scheduling and reduce the time processing required for the adaptive parameters. Additionally, the stability analysis is presented. Finally, a sensitivity function analysis is also conducted to determine boundary values for λ and δ to satisfy robustness conditions against noise and disturbances.

In this work, following the introduction, Section II presents a preliminary study of the main components of the Generalized Predictive Controller (GPC). Section III introduces an S-shaped function to implement gain-scheduling of the GPC parameters λ and δ, aiming to reduce the influence of dead zones. Section IV provides a discussion of the simulation results obtained using MATLAB®. Finally, conclusions and future research directions are outlined in Section V.

II. Preliminaries

A model-based GPC is defined by its capability to anticipate the future behavior of dynamic systems through mathematical modeling. This is achieved by computing an optimal control sequence that minimizes a predefined objective function. The GPC framework employs a receding horizon approach, also referred to as a sliding horizon, where the control horizon is continuously updated as the system evolves. In this strategy, only the first element of the computed control sequence is implemented at each time step [13] [14].

The prediction of future outputs relies on the system model, meaning that the accuracy of the model directly influences the precision of the predictions. More specifically, the closer the predicted output is to the actual system response, the more effective the control strategy becomes. At each time step k, the predicted output sequence $\overrightarrow{y}(k)$ is computed based on the past input increments $\Delta\overleftarrow{u}(k-2)$, past output sequence $\overleftarrow{y}(k-1)$, and future control increments $\Delta\overrightarrow{u}(k-1)$. The control signals and their respective increments are determined over a predefined control horizon to ensure that the plant output closely follows the desired reference trajectory $\overrightarrow{r}(k-1)$.

The control law in GPC is derived by minimizing a quadratic cost function [14]. For Single-Input Single-Output (SISO) systems, this cost function is formulated as:

$$J(\Delta u, r, y) = \sum_{k=1}^{N_p} \delta \|(\overrightarrow{r}(k) - \overrightarrow{y}(k))\|_2^2 + \sum_{k=1}^{N_c} \lambda \|\Delta\overrightarrow{u}(k-1)\|_2^2 \quad (1)$$

where J represents the cost function, N_p is the prediction horizon, and N_c is the control horizon. The parameters $\delta > 0$ and $\lambda > 0$ are weightings associated with the error sequence $\overrightarrow{e}(k) = \overrightarrow{r}(k) - \overrightarrow{y}(k)$ and the future control increment sequence $\Delta\overrightarrow{u}(k-1)$, respectively. The tuning process of parameters λ and δ, including their impact on the control law, is detailed in Section III.

Using this cost function, the control law for the GPC is formulated as follows:

$$\Delta u(k) = P_r \overrightarrow{r}(k) - D_k \Delta\overleftarrow{u}(k-2) - N_k \overleftarrow{y}(k-1) \quad (2)$$

where $P_r = E_1^T \left(\delta H^T H + \lambda I\right)^{-1} \delta H^T$, $D_k = P_r P$, and $N_k = P_r Q$. The matrix $E_1^T = \begin{bmatrix} I & 0 & \cdots & 0 \end{bmatrix}$ ensures that only the first control increment $\Delta u(k)$ from the computed control sequence $\underset{\rightarrow}{\Delta u}(k)$ is applied to the system input. To reduce computational effort and operational costs, the control law in (2) can be simplified by limiting the calculations to the control horizon:

$$\Delta u(k) = -E_1^T S^{-1} a \quad (3)$$

where $S = \delta H_1^T H_1 + \lambda I$ with $H_1 = H(1 : N_P, 1 : N_c)$ with $H = C_A^{-1} C_b \in \mathbb{R}^{N_p \times N_p}$, and $a = X[\Delta\overleftarrow{u}(k-2)\ \overleftarrow{y}(k-1)\ \overrightarrow{r}(k)]^T$ with $X = \begin{bmatrix} \delta H_1^T P & \delta H_1^T Q & -\delta H_1^T L \end{bmatrix}$ with $L = \begin{bmatrix} 1 & 1 & \cdots & 1 \end{bmatrix}^T$, $P = C_A^{-1} H_b \in \mathbb{R}^{N_p \times n_b}$ and $Q = -C_A^{-1} H_A \in \mathbb{R}^{N_p \times n_a}$, the matrices $C_b \in \mathbb{R}^{N_p \times N_p}$, $H_b \in \mathbb{R}^{N_p \times n_b}$, $H_A \in \mathbb{R}^{N_p \times n_a}$ and $C_A \in \mathbb{R}^{N_p \times N_p}$ are obtained through the polynomials $\tilde{A}(z)$ and $B(z)$ from the Controlled Auto-regressive Integrated Moving Average (CARIMA) model and Toeplitz and Hankel matrices as described in [15].

This formulation ensures that the control action is efficiently computed while maintaining the desired tracking performance.

Given the plant transfer function $G(z) = \frac{b(z)}{a(z)}$, the closed-loop characteristic polynomial, is expressed as:

$$P_c(z) = D_k(z)\Delta a + bN_k(z) \quad (4)$$

Considering the loop transfer function $G(z)\phi(z)$, where $\phi(z) = \frac{N_k(z)}{D_k(z)\Delta}$, the sensitivity functions to noise and disturbances are given as follows [14]:

$$S_d = \frac{\phi(z)}{1 + G(z)\phi(z)} = -\frac{aN_k(z)}{P_c(z)} \quad (5)$$

$$S_n = \frac{1}{1 + G(z)\phi(z)} = \frac{aD_k(z)\Delta}{P_c(z)} \quad (6)$$

These sensitivity functions characterize the system's response to external perturbations and uncertainties, playing a crucial role in the robustness analysis of the control strategy.

The stability of the constrained GPC can be established through Theorem 1 and Corollary 1.1, which utilize the method of Lagrange multipliers. These theoretical foundations provide a rigorous framework for ensuring stability while

Courtesy of IARIA Board and IARIA Press. Original source: ThinkMind Digital Library https://www.thinkmind.org

accounting for system constraints, thereby enhancing the robustness and reliability of the control strategy in practical applications [5].

Theorem *1:* Let matrices C and r_t be as in [5]. Assume that there exists an optimal minimization solution that satisfies the Karush-Kuhn-Tucker (KKT) conditions along an infinite trajectory for given weightings λ and δ . The optimum constrained cost function of the GPC at the k-th instant given by:

$$\begin{aligned} J(k) = \min_{\Delta u(k+i), i=0,1,\cdots} & \textstyle\sum_{i=1}^{\infty} \delta(e(k+i))^2 \\ & + \textstyle\sum_{i=1}^{N_c} \lambda(\Delta u(k+i-1))^2 \\ \text{subject to} \quad & C\Delta \overrightarrow{u}(k-1) \leq r_t \end{aligned} \tag{7}$$

is a monotonic decreasing function.

Corollary *1.1:* Let S and a be defined as in (3). The constrained GPC is stable if there exists an optimal solution that satisfies the KKT conditions such that the control law can be written as:

$$\begin{bmatrix} S & C^T \\ C & 0 \end{bmatrix} \begin{bmatrix} \Delta \overrightarrow{u}(k-1) \\ \overrightarrow{\phi}(k) \end{bmatrix} = \begin{bmatrix} -a \\ r_t \end{bmatrix}. \tag{8}$$

III. S-shaped function based GPC Strategy

The developed S-shaped function based GPC strategy incorporates a gain scheduling stage for the cost weighting parameter λ, to update the matrix of the standard GPC. The configuration of the proposed GPC approach is illustrated in Figure 1, where a sigmoid output is used to adjust the S matrix of the GPC.

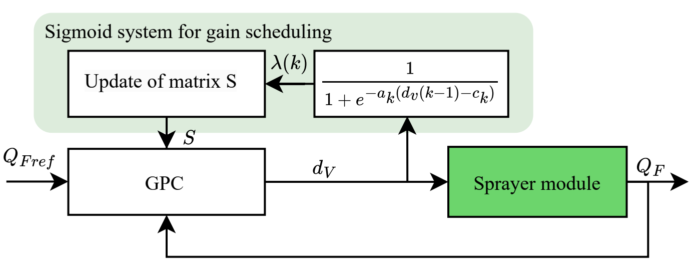

Figure 1. Adaptive GPC with λ scheduling via a sigmoid function, based on the last control signal dv.

The proposed sigmoid-based GPC is formulated as the following optimization problem:

$$\min_{\Delta u(k+i), i=0,1,\cdots} J(\Delta u, r, y) =$$

$$\sum_{i=1}^{N_p} \delta \|\overrightarrow{r}(k) - \overrightarrow{y}(k)\|_2^2 + \sum_{i=1}^{N_c} \hat{\lambda}(k) \|\Delta \overrightarrow{u}(k-1)\|_2^2 \tag{9}$$

subject to

$$C\Delta \overrightarrow{u}(k-1) \leq r_t$$

$$\forall\ \lambda(k) = \lambda_{min} + (\lambda_{max} - \lambda_{min}) \cdot f(u(k-1))$$

where λ_{max} and λ_{min} are predefined bound values for the estimates of λ established by the designer to enhance the controller's efficiency in handling nonlinearities, mainly in the dead-zone region. The function $f(u(k-1))$ represents the output of a sigmoid function, resulting values between zero and one that span the range between λ_{min} and λ_{max}, depending on the previous control input

The control strategy is implemented in conjunction with an S-shaped function known as the sigmoid function, a commonly used activation function in neural networks. The sigmoid function ensures continuity and differentiability of the system, particularly around the dead zone region, enabling smooth transitions and improved adaptability in system behavior [16]. The sigmoid function is described as:

$$f(d_v(k-1), a_k, c_k) = \frac{1}{1 + e^{-a_k(d_v(k-1)-c_k)}} \tag{10}$$

where the parameter a_k determines the inclination or spread of the transition region, while c_k specifies the midpoint of the sigmoid region.

Figure 2 illustrates the sigmoid function with varying slopes (a_k), demonstrating how the slope influences the transition between states. Smaller values of a_k result in a smoother transition (broader curves), while larger values of a_k produce a sharper transition (narrower curves). The midpoint of the sigmoid function is chosen to be around ± 20 in order to encompass the dead zone at small values of $\lambda(k)$.

The general idea of the sigmoid S-shaped function based GPC is that smaller values of $\lambda(k)$ should be adopted for the dead zone regions, causing larger control variations $\Delta u(k)$. This is because, in such cases, the ideal scenario is $\delta > \lambda(k)$, which results in larger control variations $\Delta u(k)$, driving the control signal d_v away from the dead zone. Outside the dead zone, larger values of $\lambda(k)$ stabilize the system by reducing unnecessary control activity.

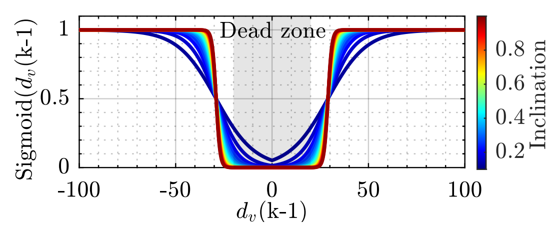

Figure 2. Proposed sigmoid S-shaped function with different inclinations.

The reason for keeping one weighting gain fixed while modifying only the other, instead of adjusting both gains simultaneously, is simplifying the system design. This simplification arises from the fact that the control signal $\Delta u(k)$ varies depending on the ratio $\frac{\lambda}{\delta}$:

- When $\delta > \lambda(k)$, the emphasis is on minimizing the tracking error, promoting aggressive control actions.
- When $\delta \leq \lambda(k)$, the ontrol effort is penalized more heavily, leading to smoother but potentially slower responses.

Fixing one parameter and dynamically adjusting the other, the complexity of tuning both parameters is reduced, while still achieving the desired balance between tracking performance and control effort.

Courtesy of IARIA Board and IARIA Press. Original source: ThinkMind Digital Library https://www.thinkmind.org

A. Stability analysis of constrained GPC with variable λ gain

The stability of the constrained GPC with a variable $\lambda(k)$ weighting gain is ensured through the careful design of the cost function and the dynamic adjustment of $\lambda(k)$. By exploiting the properties of the sigmoid function and bounding $\lambda(k)$ within predefined limits, the controller achieves a balanced trade-off between tracking performance and control effort. The stability analysis can be accomplished by Theorem 1 e Corollary 1.1 proposed in [5] for the constrained GPC, extended to the case of varying $\lambda(k)$.

Since the optimization problem involves minimizing a quadratic cost function (7), if matrix S is positive definite, the problem is convex, ensuring a global minimum solution. Since λ interferes with the main diagonal of the matrix S, to guarantee that the variation of $\lambda(k)$ does not affect the positive definiteness of S, $\lambda(k)$ is treated as a parametric uncertainty. Specifically, λ_{min} must be greater than zero, and λ_{max} must be less than a design-specified value, where the range between λ_{min} and λ_{max} is known to be stable and robust. Consequently, as long as S remains positive definite, the problem remains convex with a global minimum solution, and the stability is guaranteed.

B. Sensitivity analysis

To illustrate the effects of varying λ and δ on the robustness of the system, sensitivity analyzes were conducted, as depicted in Figures 3 and 4. These analyzes provide insights into how these parameters influence the system's ability to handle noise and disturbances. The agricultural spraying system model is considered to be described by the discrete ARMAX model obtained using 14 spray nozzles of the model 422SFC11005-ARAG and a sampling period of 300 ms:

$$A(z)y(t) = B(z)u(t) \tag{11}$$

where

$$\begin{aligned} A(z) &= 1 - 14.67 \cdot 10^{-2} z^{-1} + 24.52 \cdot 10^{-2} z^{-2} \\ &+ 22.22 \cdot 10^{-2} z^{-3}, \\ B(z) &= 0.277 \cdot 10^{-2} z^{-3} + 19.54 \cdot 10^{-5} z^{-4} \end{aligned}$$

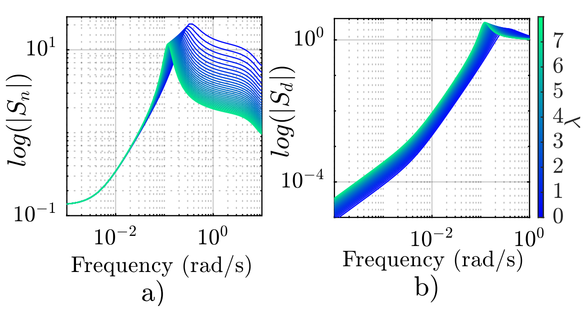

Figure 3. Sensitivity analysis curves for noise a) and disturbance b) with variable λ.

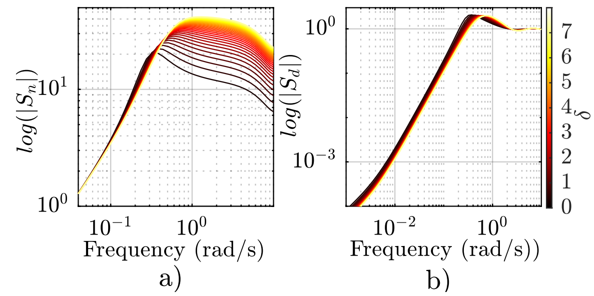

Figure 4. Sensitivity analysis curves for noise a) and disturbance b) with variable δ.

Figures 3 and 4 analyze the effects of varying λ and δ on system robustness, revealing a trade-off between noise suppression and disturbance rejection. In Figure 3, with δ held constant ($\delta = 1$) and λ varied within $0 < \lambda \leq 8$, higher values of λ reduce the amplitude of the noise sensitivity function (S_n) at high frequencies, enhancing robustness against high-frequency noise by penalizing abrupt control signal variations and promoting smoother actions. However, this comes at the expense of increased sensitivity to low-frequency disturbances, as indicated by the rise in the disturbance sensitivity function (S_d). Conversely, Figure 4 examines the impact of varying δ while keeping λ fixed ($\lambda = 1$) within $0 < \delta \leq 8$. Smaller δ increases S_n at high frequencies, reducing noise robustness due to more aggressive control adjustments that amplify high-frequency components, whereas larger δ improves robustness to low-frequency disturbances by decreasing S_d, though it may increase susceptibility to high-frequency noise. Together, these results highlight the opposing roles of λ and δ and the need for careful parameter tuning to balance performance across different operating conditions.

The opposing behaviors of λ and δ highlight the necessity for careful tuning to strike an optimal balance between noise suppression and disturbance rejection. Furthermore, system nonlinearities can introduce regions where λ and δ become inefficient for specific tuning scenarios, complicating the parameter adjustment process. This emphasizes the importance of considering gain scheduling for these parameters to address such limitations and ensure robust performance across varying operating conditions.

IV. RESULTS AND DISCUSSIONS

A simulation was conducted in MATLAB® to evaluate the regulation of a proportional valve in a sprayer module. The performance of the proposed sigmoid-based GPC is compared with that of the conventional GPC and fuzzy-based GPC controllers. The block diagram of the sprayer system is presented in Figure 5. The proportional valve actuator consists of a Direct Current motor and an H-bridge with gain K_{pH}, including a saturation block to limit the piston angle between $\theta_v = 0$ and 94.2 rad. The flow rate Q_F and pressure P_S depend on the proportional valve's fluidic resistance K_{VP}, the total equivalent fluidic resistance K_{Teq}, and the pump flow Q_B.

Courtesy of IARIA Board and IARIA Press. Original source: ThinkMind Digital Library https://www.thinkmind.org

Parameters α_0, α_1, and β define the valve's fluidic resistance curve, obtained experimentally. The parameters of the sprayer system were identified and are described in detail in [8], with the key parameters summarized in Table I.

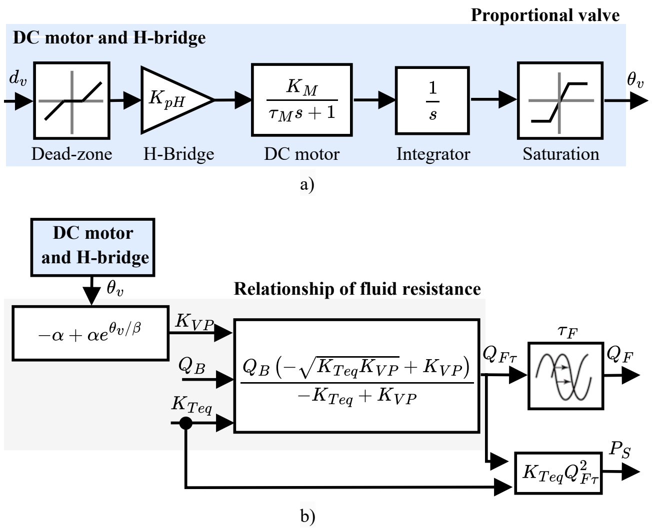

Figure 5. Block diagram of the sprayer module. Adapted from [15].

The standard GPC was tuned to minimize overshoot, achieve a faster response time, and ensure accurate predictions, with parameters set as $N_c = 4$, $N_p = 20$, $\lambda = 1$, and $\delta = 5$. For the fuzzy GPC and Sigmoid GPC designs, the same prediction and control horizons (N_p and N_c) were used. However, δ and λ were dynamically adjusted: λ was scheduled according to the fuzzy system proposed in [5], and the Sigmoid function described in Section III was employed for adaptive weighting, using $c_k = 16$, $a_k = 0.4$, $\lambda_{min} = 0$ and $\lambda_{max} = 5$.

TABLE I
PARAMETERS OF SPRAYER MODULE [8].

Parameter	Value
α	2.8110^{-6}
β	6.53
K_M	1.10 rad/V
T_M	5.0010^{-2}
K_{pH}	0.12
τ_F	0.6 s
Q_B	40 l/min
K_{Teq} (CH0.5)	5.71 kPa/(l/min)^2
K_{Teq} (CH01)	1.91 kPa/(l/min)^2
K_{Teq} (CH03)	0.97 kPa/(l/min)^2
K_{Teq} (CH06)	0.48 kPa/(l/min)^2

The simulations were repeated for each controller using two bars, each equipped with seven MagnoJet® nozzles. Constraints on the control input were handled using the Accelerated Dual Gradient-Projection Method (GPAD for short), with the input restricted to $-100 < dv(k) < 100$ due to limitations in the duty cycle of the Pulse Width Modulation (PWM) signal. A step variation was used as the reference signal using four different spray nozzles. This type of reference was chosen to approximate the problem to a real-world scenario, based on pesticide prescription maps. The simulation results are presented in Figure 6 from a) to d) for the M063/1 CH6, M061 CH3, M059 CH1, and M059/1 CH0.5 nozzles, in this sequence. The GPAD method [17] is used for handling constraints in the controllers.

For most simulations, the sigmoid based GPC controller exhibits a shorter rise time and lower steady-state error. However, for the CH0.5 nozzle in Figure 6 d), the sigmoid based GPC controller showed oscillations around the dead zone in the interval between 10 and 22 seconds. Table II provides a numerical comparative analysis of the Integral Absolute Error (IAE), Overshoot (OS), and rise time for the simulations conducted with the four nozzles.

TABLE II
PERFORMANCE OF THE CONTROLLERS WITH DIFFERENT NOZZLES

Controller	IAE (l/min)	OS (l/min)	Rise time (s)
CH06			
GPC	2.11	0.51	11.1
SGPC	1.61	0.62	8.4
FGPC	1.96	0.51	8.6
CH03			
GPC	2.22	0.6	11.4
SGPC	1.73	0.51	8.4
FGPC	2.00	2.00	9.9
CH01			
GPC	2.22	0.6	11.4
SGPC	2.00	0.61	8.5
FGPC	2.17	0.51	9.9
CH0.5			
GPC	2.48	0.2	12.7
SGPC	2.18	2.4	9.6
FGPC	2.31	0.1	11.1

The analysis of Table II reveals that the Sigmoid-based GPC (SGPC) generally outperforms the standard GPC and Fuzzy GPC (FGPC) in terms of IAE and rise time across most nozzle configurations. For instance, with the CH06 nozzle, SGPC achieves a 23.7% and 7.1% reduction in IAE compared to GPC and FGPC and a slightly faster rise time (8.4 s vs. 11.1 s and 8.6s). Similarly, for CH01, SGPC reduces IAE by 10.8% compared to GPC, while maintaining a comparable rise time. However, overshoot varies significantly: SGPC exhibits higher OS in some cases, such as CH05, where it reaches 2.4 l/min, contrasting sharply with FGPC's 0.1 l/min. This suggests a trade-off between error minimization and transient response smoothness.

Across all nozzles, FGPC demonstrates moderate performance, balancing IAE and OS but often failing to match the IAE reductions achieved by SGPC. For example, in CH03, FGPC shows a high OS of 2.0 l/min, indicating potential instability or excessive control effort despite reducing IAE by 10.4% compared to GPC. Overall, SGPC emerges as the most effective controller for minimizing IAE and rise time, achieving improvements of up to 23.7% in IAE, though its higher OS in certain scenarios may require further tuning to optimize robustness.

Courtesy of IARIA Board and IARIA Press. Original source: ThinkMind Digital Library https://www.thinkmind.org

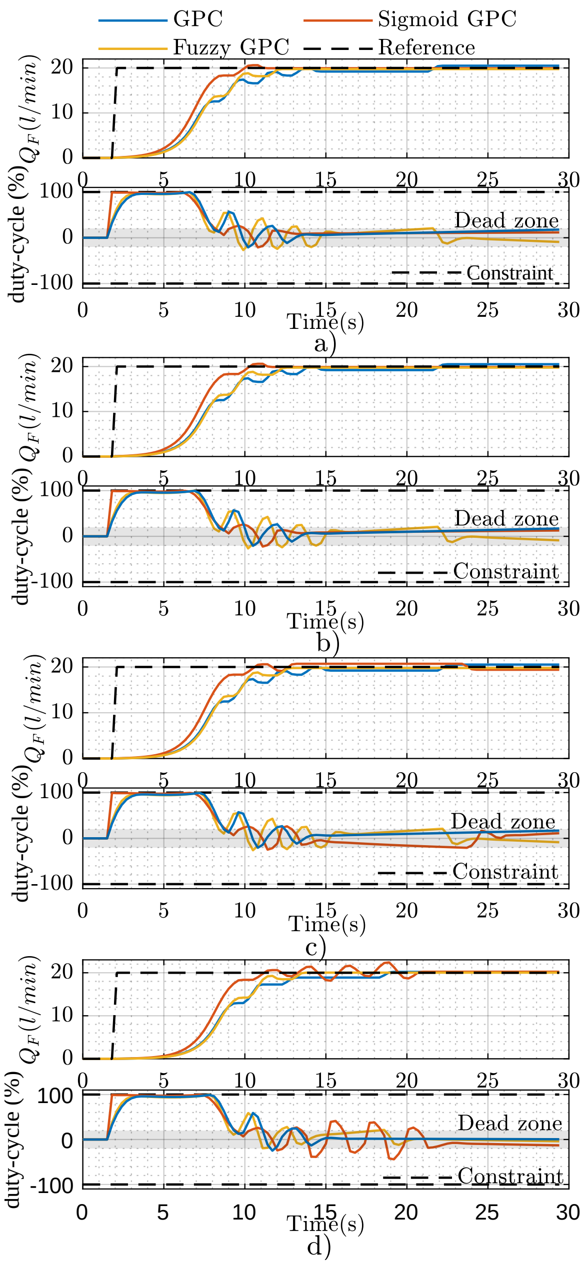

Figure 6. Step response to MagnoJet ® nozzles.

V. CONCLUSION AND FUTURE WORK

In this paper, the performance of GPC, fuzzy-based GPC, and a sigmoid-based GPC controller for regulating flow rate in agricultural sprayers is discussed and compared. The simulation results demonstrate the feasibility of using the sigmoid function to schedule the GPC parameter λ, enhancing system response and addressing dead zone nonlinearities.

The incorporation of the sigmoid function enables the inclusion of bounds for the GPC parameters in the stability analysis, as discussed. Furthermore, the sensitivity analysis provides insights into determining the bounds of the sigmoid-based GPC parameters while considering the system's response to noise and disturbances. The results confirm the practical effectiveness of the sigmoid-based GPC in agricultural sprayers, reducing actuator wear and minimizing application errors caused by abrupt reference changes.

For future research, an embedded programmable sigmoid-based GPC is proposed for real-time processing. The sigmoid S-shape function simplifies the embedded implementation of adaptive systems, requiring minimal code and reducing processing time compared to fuzzy logic, which often depends on lookup-table searches or surface inference methods. This method is promising for real-time applications in resource-constrained environments.

ACKNOWLEDGMENTS

This research was supported by the Brazilian Agricultural Research Corporation (Embrapa Instrumentation, under grant SEG, Process 11.14.09.001.05.06.001 Development of advanced automated models, tools and instruments for precision agricultural spraying), the National Counsel of Technological and Scientific Development (CNPq, under grant 88887.703189/2022-00) and São Paulo Research Foundation (FAPESP, under grant 2023/06759-0).

REFERENCES

[1] E. A. Straw, E. Kelly, and D. A. Stanley, "Self-reported assessment of compliance with pesticide rules," *Ecotoxicology and Environmental Safety*, vol. 254, 2023.

[2] E.-C. Oerke, R. Gerhards, G. Menz, and R. A. Sikora, *Precision crop protection - the challenge and use of heterogeneity*. Boon: Springer, 2010, vol. 5.

[3] M. Grella et al., "Field assessment of a pulse width modulation (pwm) spray system applying different spray volumes: duty cycle and forward speed effects on vines spray coverage," *Precision Agriculture*, vol. 23, no. 1, pp. 219–252, 2022.

[4] P. Wang, A. Saiful Hanif, S.-H. Yu, C.-G. Lee, Y. Ho Kang, D.-H. Lee, and X. Han, "Development of an autonomous drone spraying control system based on the coefficient of variation of spray distribution," *Computers and Electronics in Agriculture*, vol. 227, p. 109529, 2024. [Online]. Available: https://www.sciencedirect.com/science/article/pii/S0168169924009207

[5] D. R. Schutz, H. V. Mercaldi, E. A. Peñaloza, L. J. Silva, V. A. Oliveira, and P. E. Cruvinel, "Advanced embedded generalized predictive controller based on fuzzy gain scheduling for agricultural sprayers with dead zone nonlinearities," *Journal of Process Control*, vol. 135, no. 103164, pp. 1–11, 2024.

[6] Y. Shi, A. Liang, H. Yuan, C. Zhang, and J. Li, "Modeling and simulation for a variable sprayer rate system," *Computer and Computing Technologies in Agriculture II*, vol. 1, no. 293, p. 573–584, 2009.

[7] A. E. Aissaoui, F. Lebeau, L. Elbahir, M. F. Destain, and K. Houmy, "A feasibility study of developing direct injection spraying technology for small scale farms," in *2nd international conference on agricultural engineering, Synergy in the Technical Development of Agriculture and Food Industry*. Godollo, Hungary, 2011, pp. 9–15.

[8] K. R. Felizardo, H. V. Mercaldi, V. A. Oliveira, P. E. Cruvinel, and B. L. Steward, "Modeling and model validation of a chemical injection sprayer system," *Applied Engineering in Agriculture*, vol. 32, no. 3, pp. 285–297, 2016.

[9] Q. Zhao, Q. Liu, N. Cao, F. Guan, S. Wang, and H. Wang, "Stepped generalized predictive control of test tank temperature based on back-propagation neural network," *Alexandria Engineering Journal*, vol. 60, no. 1, pp. 357–364, 2021.

[10] S. Xie, Y. Xie, T. Huang, W. Gui, and C. Yang, "Generalized predictive control for industrial processes based on neuron adaptive splitting and merging RBF neural network," *IEEE Transactions on Industrial Electronics*, vol. 66, no. 2, pp. 1192–1202, 2018.

Courtesy of IARIA Board and IARIA Press. Original source: ThinkMind Digital Library https://www.thinkmind.org

[11] J. Mendes, R. Araújo, and F. Souza, “Adaptive fuzzy generalized predictive control based on discrete-time TS fuzzy model,” in *2010 IEEE 15th Conference on Emerging Technologies & Factory Automation (ETFA 2010)*. IEEE, 2010, pp. 1–8.
[12] S. F. Ramezani, E. Vafa, M. Fakhroleslam, and M. Shahrokhi, “Adaptive predictive control of a fan-ventilated tunnel greenhouse with evaporative cooling,” *Journal of Process Control*, vol. 129, 2023.
[13] E. F. Camacho and C. Bordons, *Model predictive control*. London: Springer Science & Business Media, 2013.
[14] J. A. Rossiter, *Model-based predictive control: a practical approach*. Washington, D.C.: CRC press, 2003.
[15] D. R. Schutz, H. V. Mercaldi, E. A. Penaloza, V. A. Oliveira, and P. E. Cruvinel, “An intelligent fuzzy-GPC control for agricultural sprayers: comparison between GPC and PID fuzzy controllers,” in *15th APCA International Conference on Automatic Control and Soft Computing, July 6-8, 2022, Caparica, Portugal*. Springer, 2022, pp. 272–284.
[16] L. J. R. Silva, M. V. R. Campos, B. M. Zilli, T. A. Fagundes, R. V. A. Neves, R. Q. Machado, and V. A. Oliveira, “A sigmoid-weighted-consensus for balancing multiple battery energy storage systems,” *IEEE Transactions on Industrial Electronics*, 2024.
[17] V. B. Peccin, D. M. Lima, R. C. C. Flesch, and J. E. Normey-Rico, “Fast generalized predictive control based on accelerated dual gradient projection method,” *IFAC-PapersOnLine*, vol. 52, no. 1, pp. 480–485, 2019.

Courtesy of IARIA Board and IARIA Press. Original source: ThinkMind Digital Library https://www.thinkmind.org

Copyright (c) IARIA, 2025. **ISBN: 978-1-68558-273-9**

Evaluation of an IoT System Used with Sensors for the Recognition of Invasive Plants in Groundnut Crops

Bruno M. Moreno*†, Paulo E. Cruvinel*†, and Augusto G. F. Costa‡

* Embrapa Instrumentation (CNPDIA), São Carlos, SP, Brazil
† Postgraduate Program in Computer Science, Federal University of São Carlos, São Carlos, SP, Brazil
‡ Embrapa Cotton, Campina Grande, PB, Brazil
Emails: bruno.moreno@estudante.ufscar.br, paulo.cruvinel@embrapa.br, augusto.costa@embrapa.br

***Abstract*—Sensors are quite important for data collection from the physical agricultural world, and also a key part of the Internet of Things (IoT) ecosystem. The IoT has enabled monitoring and automation in agriculture, supporting the implementation of precision agriculture applications using sensors in the field. However, the effectiveness of these systems depends on the accurate verification and assessment of network parameters such as connectivity, sensor reliability, and data integrity. Ensuring the proper functioning of IoT devices is crucial to maintaining efficiency, reducing costs, and improving overall agricultural outcomes. This study highlights factors to consider when developing an IoT system based on an experimental field study for pattern recognition of invasive plants in groundnut crops, resulting in classifiers with an accuracy of approximately 80%.**

Keywords-IoT sensor; IoT communication; pattern recognition; precision agriculture; weed management.

I. Introduction

Since its initial conception, the Internet of Things (IoT) has enabled a range of application possibilities in different areas, as the concept of devices acquiring data from the environment, communicating with each other, and performing actions based on this exchange of information would allow for a multitude of control and surveillance actions, managed locally and in an automated manner. With the new opportunity landscape driven by lower hardware prices, advanced computing, cloud storage, higher speed and lower connectivity costs, current investments in IoT applications are predicted to contribute to an annual global growth of 0.99% Gross Domestic Product (GDP) by 2030 [1].

Such applications make use of a variety of sensors capable of wireless communication with other devices. The main objectives of these sensors are to obtain information of interest from the external physical environment, sample internal signals from the system, and interpret the data, allowing decision-making performance [2]. Sensors must be part of a wireless network with other devices, not necessarily connected to the Internet, as there is data exchange. Therefore, it is important to highlight that there are three key points in IoT systems: capture and processing of data collected by sensors; communication between devices; and aggregation, processing and interpretation of data from different sensors.

Sensors used in IoT can vary greatly, as long as there is the possibility that their output can be transmitted wirelessly. For agricultural applications, for example, position sensors can be used to detect the location of the device when attached to a drone or an animal; temperature, chemical and humidity sensors to know what the environmental situation is in real time in the field; water quality sensors to monitor water reservoirs; and infrared and optical sensors to monitor crops or livestock in the field [3].

The use of IoT sensors can help address one of the challenges in groundnut (*Arachis hypogaea*) cultivation, which is invasive plant interference, since the crop is highly susceptible to competition due to its slow initial growth [4]. The presence of invasive plants in groundnut crops can result in productivity losses greater than 90% and can interfere with the harvesting process, increasing production costs and potentially impacting product quality [5]. Optical and position sensors can then be used to assist in the use of computer vision, based on the development of systems that recognize invasive plants in the environment and allow specific and localized decisions on how to treat the crop [6].

In the literature, many studies propose methods to combine weed detection and classification with IoT systems. Most of them focus more on processing operations but leave aside IoT assessments and sensor data management, focusing more on hypothetical applications of the algorithms in an IoT model. Kansal *et al.* proposed an IoT-Fog computing-enabled robotic system for weed and soybean classification during normal and foggy seasons, processing well hazy images [7], while Tiwari *et al.* also developed a system using IoT camera sensors and cloud computing for a Deep Learning (DL) weed classification for a public dataset of 12 weed species [8]. On the other hand, Dankhara *et al.* proposed a model using a Raspberry Pi (RPi) 3 with a camera sensor and a sprayer for use with a weed classifier controlled remotely with the help of an Internet connection to an external server [9].

Kulkarni *et al.* developed a system capable of acquiring images using a RPi, detecting weeds by a Convolutional Neural Network (CNN) model trained offline, and the weed segments are marked and sent to farmers via email by the Global System for Mobile Communications (GSM) module [10]. Likewise, Farooq *et al.* built a fast and high-performance DL model that required less computing power on a RPi 4 to enable on-device machine learning, using a public dataset for weed detection [11]. All these studies used images acquired

Courtesy of IARIA Board and IARIA Press. Original source: ThinkMind Digital Library https://www.thinkmind.org

from existing databases, not testing the proposed systems in real field conditions using their own sensors, and therefore their IoT specifications and limitations were not considered and prioritized, except for those related to the computational cost of data processing and strategies to reduce it.

Moreno and Cruvinel presented previous studies related to a stereo camera's system using IoT principles, specifying the optical sensor bias correction process [12], and the development of a software based on semantic computing concepts for the segmentation of invasive plants [13]. Expanding the previous studies, this work aims to develop an IoT system for recognizing more than one invasive plant species in groundnut crops capable of acquiring stereo images in a real-field operation, providing processing in real images acquired from wireless commands in an experimental field. Therefore, the limitations regarding handling data obtained by IoT sensors in practical application are considered more carefully.

This paper is structured as follows. Section II presents the materials and methods used, including IoT sensor data insights, IoT communication protocols, camera sensor specifications, and method for recognition of invasive plants. Section III presents the results and discussion of the IoT system developed and the classifiers utilized, with the final conclusions and proposed future works in Section IV.

II. Material and Methods

This section will delve into the specifications and points of interest when collecting and managing data from IoT sensors, important protocols for IoT communication, and specifications of the devices and camera sensors used. Furthermore, an overview of the algorithm for invasive plant recognition is presented, including the experimental setup for collecting and working with data collected by the camera sensors in a real cultivation environment.

A. IoT Sensor Data Insights

The development of IoT systems must take into account the quality and quantity of data generated by sensors in order to generate useful information that can be verified as a whole. Data is also transmitted over a network, and therefore both aspects related to the transmission and storage of this data and those related to the security of the network as a whole must be considered. Therefore, when analyzing sensor data, the following characteristics need to be points of interest in the system development stages:

1) Security: The network and its transmitted data must guarantee the privacy of information, that is, sensor data will only be transmitted to trusted devices. Data cannot be transmitted or captured by other devices outside the configured and trusted network, while data on the network must remain authentic, not suffering from external attacks with the injection of erroneous data packets. Data must also remain intact, considering the transmission errors inherent in wireless networks. Measures that can be taken include Secure Sockets Layer/Transport Layer Security (SSL/TLS), Datagram Transport Layer Security (DTLS), Blockchain and Elliptic Curve Cryptography (ECC) [14].

2) Scalability: Because the sensor network includes data sources from multiple sensors and actuators, it must be scalable to handle the exponential growth of devices and data handling. Latency should not be so high that it hinders processing steps to the point of making operations and decision-making, especially in real time, impractical [15].

3) Bandwidth Availability: Bandwidth can be a bottleneck in the transmission path, resulting in many problems such as sensor data loss, delays and congestion. It is necessary to correctly predict which communication path between devices will have the most information being transmitted or to develop algorithms to be able to dynamically change the bandwidth availability of the paths, creating a reallocation plan according to a set of criteria such as data importance and data volume. If system latency and bandwidth are not critical, a cloud computing scenario can be enough [16].

4) Battery Life: Devices and sensors in an IoT system must be energy efficient and capable of low-power communication with low-cost on-node processing. They can be battery-powered, capable of alerting when power is low to allow for early battery replacement, or harvest energy from the environment, for example, using a solar cell.

5) Data Volume: Due to the large volume of data generated by sensors, it is necessary to pass them through cleaning, noise removal and outlier detection processes to obtain only the relevant information. This volume can generate both an increase in the computational cost of the system in these steps and overload the transmission network. In addition, this data and the processing results can be saved on the devices, which means that their memory and storage capacity must be considered when building the system, even in cases where the data is partially saved in the cloud.

6) Exposure Risk: Technical constraints of devices, such as sensor size, make them vulnerable and prone to failure, attack and breakage. Therefore, it is recommended to use protective cases against unwanted external elements, especially for field operations where sensors may be exposed to rain, dust, extreme temperatures and even damage from animals. IoT systems must also be secure so that they cannot be accessed inappropriately or subject to fraud by human action, ensuring reliable information.

B. IoT Communication Protocols

The general structure of an IoT system can be exemplified by Figure 1, in which fog processing can be performed near or at the sensor node. In the Edge Computing node, the data can be stored and processed locally, allowing only useful data to be transmitted to other devices or to the cloud, while the Fog Computing node waits for a considerable amount of local computation, storage, and communication to complete before performing the transmission over the web.

The Bluetooth used communication can support up to 7 devices connected simultaneously, supporting a maximum transfer rate of 1 Mbps, with a signal range of 10 m away from the device indoors and up to 50 m outdoors.

Courtesy of IARIA Board and IARIA Press. Original source: ThinkMind Digital Library https://www.thinkmind.org

Copyright (c) IARIA, 2025. ISBN: 978-1-68558-273-9

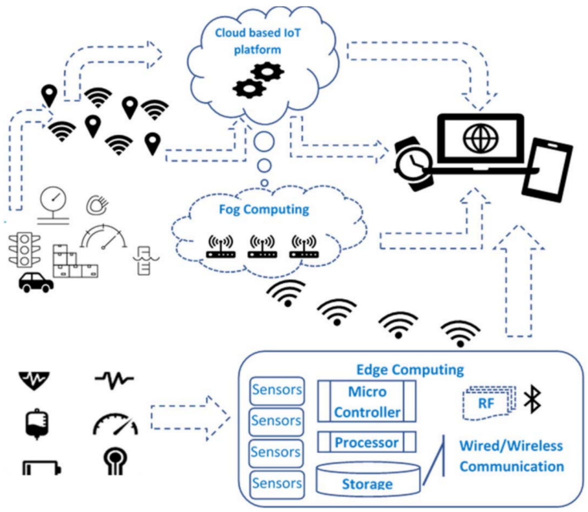

Figure 1: Example of IoT systems structure, with sensor data processing level node [14].

One of the protocols used is Radio Frequency Communication (RFCOMM). The RFCOMM protocol is a serial interface to the Bluetooth transport layer, emulating an RS-232 interconnect cable. RFCOMM is built upon the ETSI 07.10 standard, which allows the emulation and multiplexing of multiple serial ports on a single transport [17]. Additionally, the OBEX protocol (OBject EXchange) is utilized for file transfer, which is a software implementation of the File Transfer Protocol (FTP) network protocol, which runs on top of RFCOMM.

C. Camera Sensor Specifications

For the task of invasive plant recognition, an optical sensor in the visible spectrum is capable of capturing sufficient data. Therefore, an RGB camera and a control device for managing the sensor (responsible for turning on, adjusting settings, and triggering the camera) and the wireless data transmission are required in the development of the IoT system. Thus, the RPi 3 model B+ and Pi Camera v1 were chosen as the device and the sensor, as can be seen in Figure 2.

The use of the RPi in agriculture has been observed because it is a state-of-the-art computer with numerous practical applications in all areas of activity [18]. The embedded computer, combined with its sensors, allows both image capture and processing in the same module, allowing applications in stereo systems and precision agriculture [19]. The RPi requires a 5 V power supply and up to 2.5 A to power itself and the attached optical sensor, with its own operating system installed, the RPi OS, known as Raspbian.

The RPi model has a 64-bit BCM2837B0 Cortex-A53 (ARMv8) processor, 1 GB of SDRAM, and a processor speed of 1.4 GHz. The size of the internal memory is determined by the capacity of the chosen micro SD card, with a minimum of 8 GB being recommended. The RPi supports Local Area Network (LAN) and Bluetooth Low Energy (BLE) wireless communication from a Cypress CYW43455 chip. The Pi camera has a fixed focal length of 3.60 mm, a maximum sensor resolution of 2592 x 1944 *pixels*, and a camera aperture angle of 53.50º horizontally and 41.41º vertically. In addition, the camera's ideal focus is 1 m - ∞ and its signal-to-noise ratio is 36 dB. Another important detail is that the RPi automatically adjusts the camera's brightness and white balance, but if necessary, it is possible to correct these values via software. These and other specifications can be seen in Table I.

D. Recognition of Invasive Plant

1) Experimental Setup: For the practical experiment, two invasive plants of groundnut crops (cultivar IAC OL3) were chosen for analysis: velvet bean (*Mucuna aterrima*), a plant with broad and dark green leaves; and signal grass (*Urochloa decumbens*), a plant with long and blade-shaped leaves. The experiment was carried out in the municipality of Jaboticabal-SP, Brazil. Pest and disease management was carried out according to specific recommendations for the crop [20]. The groundnut cultivation area selected for the experiment totals 72 m^2 and, to simulate the presence of the invasive plants, they are sown together and separately with the groundnuts. Once grown, field images are captured from this simulation.

2) Feature Extraction: Once collected, the images are preprocessed, filtering out noise and biases derived from the intrinsic characteristics of the sensor.

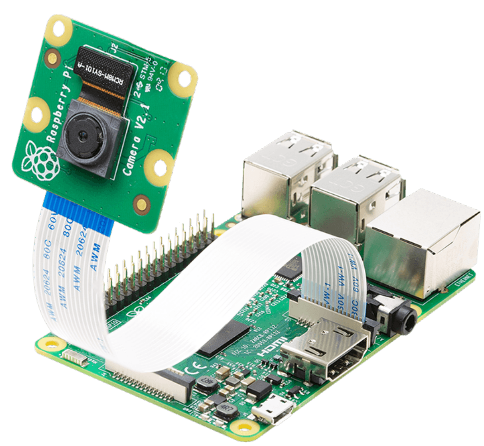

Figure 2: Sensor and connected device.

TABLE I: Pi Camera Characteristics

Size	25 x 24 x 9 mm
Resolution	5 MP
Video modules	1080p30, 720p60, 640x480p60/90
Sensor	OmniVision OV5647
Sensor resolution	2592 x 1944 pixels
Sensor image area	3.76 x 2.74 mm
Pixel size	1.4 μm x 1.4 μm
Optical size	1/4”
Full-frame SLR equivalent	35 mm
S/N Ratio	36 dB
Dynamic range	67 dB @ 8 times gain
Fixed focus	1 m - ∞
Focal length	3.60 ± 0.01 mm
Horizontal field of view (HFOV)	53.50° $\pm$ 0.13°
Vertical field of view (VFOV)	41.41° $\pm$ 0.11°
Focal ratio (F-stop)	2.9

Courtesy of IARIA Board and IARIA Press. Original source: ThinkMind Digital Library https://www.thinkmind.org

The object of interest is selected from a histogram threshold segmentation, in which the original image is converted to the Hue-Saturation-Value (HSV) color space and a range in the H channel corresponding to the colors of the plants is selected. This method presents a better result when segmenting plants, reducing the impact of variations in illumination and saturation in different images [21]. To improve the result, morphological closing and opening operations are applied to reduce small holes and objects present, respectively.

From this point on, the segmented image is used as a mask on the original image, and based on the intensity of the remaining pixels, the features of the imaged plants are extracted using a texture descriptor and a shape descriptor. The texture descriptor used is based on five Haralick moments: energy, entropy, contrast, homogeneity and correlation [22]. The shape descriptor is the Local Binary Patterns (LBP), applied on the edges of the leaves obtained by the Canny edge detection algorithm [23][24].

3) Pattern Recognition: The descriptor data are grouped into vectors, corresponding to windows present in the image, which are used to train a classifier that assists in the separation of invasive plant species from families. Each window is manually and binary labeled with the presence or absence of each plant. The classifier used was the Support Vector Machine (SVM) [25], varying the internal parameters and dividing the samples into 80% for training and 20% for testing. As the main evaluation metric, the accuracy of the classifier is used, in which the rate of correct predictions is analyzed in relation to the total number of samples tested. Other metrics, such as precision, sensitivity and F-score, are also considered for evaluating the robustness of the classifier, weighting both false positives and false negatives predictions.

III. Results and Discussion

The system was evaluated in relation to the modeling of IoT systems and its experiment in real field application, analyzing the hardware used in its construction and the operational parameters, including the communication protocols and sensor data management. In addition, the results of the classifier for the experimental groundnut cultivation plot were obtained, with its metrics, processed digital images, and application cost analysis.

A. IoT System Evaluation

The IoT system developed consists of two camera sensors each one attached to an RPi with a 32 GB micro SD card, power supplied by a 12 V 60 Ah battery with voltage converted to 5 V, an Android cell phone for user control, and a structure and protective case to house the sensors. The cameras are pointed downwards to correctly capture the crop area. One of the RPis was defined as master, responsible for managing the network via Bluetooth, communicating with the other devices (the slave RPi and the cell phone).

The system was then evaluated, considering each of the topics of interest in IoT sensors. In terms of power, each RPi had a power consumption of around 3 W, and the total system, including other peripherals and converters, reached a maximum of 18 W. Thus, the battery was able to power the system uninterruptedly for 15 hours. The structure in which the sensors are located does not yet have autonomous movement and requires human supervision during its operation. However, if the equipment is coupled to a vehicle, robot or drone, its power supply may be shared with them, requiring a new evaluation of the energy consumption.

Regarding the volume of data, it was decided that each captured image would have a resolution of 1280 x 960 pixels, a resolution chosen so that the digital image would still contain a good amount of information without generating files that require a lot of storage capacity, using the PNG compression format. The data captured by both sensors was stored on the master RPi, because if it were necessary to perform stereo processing of the data, it would already be stored there. In this way, the system was able to save 6,000 images in memory.

To ensure system security, it is connected only to trusted equipment, using each device's Media Access Control (MAC) address and specific ports when creating wireless communication sockets. The devices automatically initiate their connection algorithms and protocols during their boot. If it is necessary to allow pairing of new mobile phones, the embedded systems must be accessed directly, which requires a fixed username and password to access the operating system.

Once communication was established, image capture was controlled via the cell phone, as shown in the pseudocodes in Figure 3. The Android application had buttons that, when pressed, sent a sequence of commands to the Master RPi via Bluetooth and serial communication. Each command consisted of a five word string. This command was used to capture images, transmit files to the cell phone, or shut down the system. The app interface can be shown in Figure 4, and is a Bluetooth serial controller that allows customization by the user, adding buttons and commands as needed.

Each operation had a 15-second delay to ensure that file management operations (especially saving the image file) were performed correctly by the devices. Wireless communication allowed data transmission to be performed uninterruptedly when manually requested by the user, avoiding corrupted files received. If the operator needed to view the image captured on his device only to monitor the system operation, a command could be sent that returned an image with a resolution of 320 x 240 pixels. This option ensured wireless communication during field operations with lower latency, in addition to allowing the user to check the number of images saved in memory based on the file name. In this way, the system was controlled wirelessly and thus able to capture and form a stereo image database relating to the groundnut cultivation field analyzed.

Compared to existing IoT models, the decision was made to store the data on the device instead of sending it to an external server or cloud. Furthermore, capturing real data using the system's own sensors allows for a more problem-focused assessment, acquiring images to train the classifier that represent the real challenges of the weed recognition

Courtesy of IARIA Board and IARIA Press. Original source: ThinkMind Digital Library https://www.thinkmind.org

```
function IMAGE CAPTURE ON THE MASTER RPI(comd, resol, dir)
begin function
    while True do
        if comd == 'captr' then
            send(comd, Slave)                         ▷ sync trigger
            img ← capture_image(resol)
            save_image(img, dir)
            img2 ← receive_data(Slave)
            wait_operation()
            save_image(img2, dir)
        else if comd == 'send1' then
            send(img, cell_phone)
            wait_operation()
        else if comd == 'send2' then
            send(img2, cell_phone)
            wait_operation()
        else if comd == 'slres' then
            send(lower_resolution(img), cell_phone)
            wait_operation()
        else if comd == 'shutd' then
            send(comd, Slave)
            wait_operation()
            shutdown_system()
        end if
    end while
end function

function IMAGE CAPTURE ON THE SLAVE RPI(resol, dir)
begin function
    while True do
        comd = receive_data(Master)
        if comd == 'captr' then
            img2 ← capture_image(resol)
            save_image(img2, dir)                     ▷ optional
            send(img2, Master) ▷ via OBEXFTP protocol
            wait_operation()
        else if comd == 'shutd' then
            shutdown_system()
        end if
    end while
end function
```

Figure 3: Pseudocode for image capture on both RPis controlled by bluetooth.

Figure 4: Android application interface for wireless communication.

task. Thus, the results of the classifiers will be more robust when compared to classifiers trained with images that may not accurately represent the variability found in real environments.

B. Classifier Results

Sixty-four georeferenced images of 1280 x 960 pixels were obtained, representing the crop field where the plants grew. Each image captured 0.76 m² of the experimental area, forming an 8 by 8 grid. The ideal threshold range for the segmentation process was H channel values between 25 and 70; morphological operations eliminated objects with less than 75 pixels in area and holes smaller than 150 pixels. By dividing the images into square windows of 100 pixels (eliminating the regions where the foot of the device responsible for the capture was located), a total of 6912 samples were obtained (108 per image), of which 5529 were separated for training the classifiers and 1383 for testing. The vector obtained by the feature extraction stage had a size equal to 14 per window.

For the SVM classifiers, three kernels were analyzed: linear, Gaussian and Radial Basis Function (RBF). The kernel functions aim to better deal with non-linear patterns of similarity between elements of the same class. Analyzing all of them and considering the processing time and accuracy, the best configuration for weed classification was the RBF kernel (C = 1000 and $\gamma = 0.01$), with an accuracy of 79.2% for signal grass and 81.1% for velvet bean.

Table II shows the final result of the SVM classifiers for each invasive plant, with the total values and individuals for each class, considering that for the samples the null hypothesis $\mathcal{H}_0$ corresponds to the case of no invasive plant, while the alternative hypothesis $\mathcal{H}_1$ is when there is presence of the invasive plant in the sample window of the image. It can be observed that, although they have good accuracy and precision, the sensitivity for invasive plants is low, which could be improved by using a feature vector with more elements (adding more descriptors at the expense of processing time).

Figure 5 shows an example of the original image, the label used for training, and the results of the classifiers (black is not an invasive plant, false color is). In the labeled image, the green pseudocolor represents velvet bean, the blue represents signal grass, and the red represents other plants (including the groundnut plant).

Regarding the costs of a possible herbicide application, the control of signal grass was considered using Cletodim (0.4 L/ha) and mineral oil as adjuvant (0.5 L/ha) and the control of velvet bean with Imazapic (140 g/ha) and adjuvant (0.25 L/ha). The costs for the control of signal grass were estimated at USD 11.19/ha, and for velvet bean they were USD 51.43/ha. Since the experimental area was 72 m^2, if the product were applied uniformly throughout the area, the total cost of the weed management would be USD 0.45. Using the developed system, the classifiers obtained an area of occupation of signal grass of 4.12%, and of the velvet bean of 14.54%. Thus, if the herbicide application followed the proposed method and applied the product only where there are invasive plants, the cost of weed control would be USD 0.057 for the same area.

Courtesy of IARIA Board and IARIA Press. Original source: ThinkMind Digital Library https://www.thinkmind.org

TABLE II: SVM classifier results

Classifier	Precision	Sensitivity	F-score	Samples	Accuracy
SVM velvet bean				1383	81.1%
$\mathcal{H}_1$	0.80	0.41	0.54	349	80.2%
$\mathcal{H}_0$	0.83	0.97	0.89	1034	82.8%
SVM signal grass				1383	79.2%
$\mathcal{H}_1$	0.72	0.14	0.23	313	71.7%
$\mathcal{H}_0$	0.80	0.98	0.88	1070	79.6%

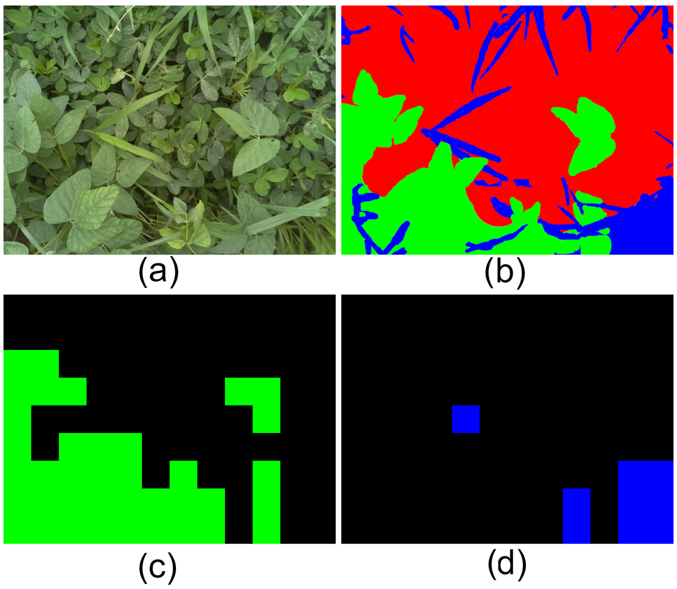

Figure 5: Recognition of invasive plants: (a) original image captured by the system, (b) manually labeled image, (c) classifier result for velvet bean, and (d) classifier result for signal grass.

It is possible to refine even more this result, using the information provided by the stereo sensors-based images to utilize the depth perception of the acquired images in the control of the invasive plants, allowing treatment in layers in relation to the height of the plants.

IV. Conclusion

It can be concluded that the use of IoT sensors can aid the task of recognizing and distinguishing the presence of different invasive plants in groundnut crops. This aids in more precise use of herbicides on crops and can be adapted to crops other than groundnuts, reducing the cost and environmental impact of weed control. Considering the decision-making steps, results have proved the usefulness of the developed sensor-based system to operate with great precision and generate information for agricultural management. Besides, important factors in handling IoT sensor data and communication have been observed, leading to a specific protocol and requirements related to security breaches as much as possible, and including functionalities to decrease latency.

The invasive plants classifiers achieved accuracy close to 80%; however, sensitivity can still be improved by refining the descriptors and the image working window. Despite the promising results, the current system is limited by the hardware on-device processing. For future work, it is being considered the integration of the system into Field Programmable Gate Array (FPGA) platform in order to have configurable possibilities related to prototyping based on high performance computing and thus improving the processing cost.

Acknowledgment

This work has been supported by the Brazilian Corporation for Agricultural Research (EMBRAPA), and the Coordenation for the Improvement of Higher Education Personel (CAPES).

References

[1] H. Edquist, P. Goodridge, and J. H. and, "The internet of things and economic growth in a panel of countries," *Economics of Innovation and New Technology*, vol. 30, no. 3, pp. 262–283, 2021.

[2] R. Krishnamurthi, A. Kumar, D. Gopinathan, A. Nayyar, and B. Qureshi, "An overview of IoT sensor data processing, fusion, and analysis techniques," *Sensors*, vol. 20, no. 21, 2020, ISSN: 1424-8220.

[3] D. Sehrawat and N. S. Gill, "Smart sensors: Analysis of different types of IoT sensors," in *2019 3rd International Conference on Trends in Electronics and Informatics (ICOEI)*, 2019, pp. 523–528.

[4] N. G. Sai and D. Subramanyam, "Impact of weed management practices on weed growth, crop yield and soil microbes in groundnut," *Indian Journal of Weed Science*, vol. 55, no. 3, pp. 340–344, 2023.

[5] Z. Gonzalez *et al.*, "Herbicide selectivity in peanut cultivars," *Journal of Agricultural Science*, vol. 10, pp. 447–447, Jul. 2018.

[6] J. F. S. Gomes and F. R. Leta, "Applications of computer vision techniques in the agriculture and food industry: A review," *European Food Research and Technology*, vol. 235, no. 6, pp. 989–1000, 2012.

[7] I. Kansal, V. Khullar, J. Verma, R. Popli, and R. Kumar, *Paladyn, Journal of Behavioral Robotics*, vol. 14, no. 1, p. 20 220 105, 2023.

[8] S. Tiwari *et al.*, "IoT-enabled model for weed seedling classification: An application for smart agriculture," *AgriEngineering*, vol. 5, no. 1, pp. 257–272, 2023, ISSN: 2624-7402.

[9] F. Dankhara, K. Patel, and N. Doshi, "Analysis of robust weed detection techniques based on the internet of things IoT," *Procedia Computer Science*, vol. 160, pp. 696–701, 2019, ISSN: 1877-0509.

[10] S. Kulkarni, S. Angadi, and V. Belagavi, "IoT based weed detection using image processing and cnn," *Int. J. Eng. Appl. Sci. Technol*, vol. 4, no. 3, pp. 606–609, 2019.

[11] U. Farooq *et al.*, "Lightweight deep learning model for weed detection for IoT devices," in *2022 2nd International Conference on Emerging Frontiers in Electrical and Electronic Technologies (ICEFEET)*, 2022, pp. 1–5.

[12] B. M. Moreno and P. E. Cruvinel, "An IoT stereo image sensor system for agricultural application," *International Journal On Advances in Software*, vol. 16, no. 3 & 4, pp. 160–171, 2023, ISSN: 1942-2628.

[13] B. M. Moreno and P. E. Cruvinel, "Computer vision system for identifying on farming weed species," in *IEEE 16th International Conference on Semantic Computing (ICSC)*, 2022, pp. 287–292.

[14] S. C. Mukhopadhyay *et al.*, "Artificial intelligence-based sensors for next generation IoT applications: A review," *IEEE Sensors Journal*, vol. 21, no. 22, pp. 24 920–24 932, 2021.

[15] H. Landaluce *et al.*, "A review of IoT sensing applications and challenges using rfid and wireless sensor networks," *Sensors*, vol. 20, no. 9, 2020, ISSN: 1424-8220.

Courtesy of IARIA Board and IARIA Press. Original source: ThinkMind Digital Library https://www.thinkmind.org

[16] O. Said, "A bandwidth control scheme for reducing the negative impact of bottlenecks in IoT environments: Simulation and performance evaluation," *Internet of Things*, vol. 21, p. 100 682, 2023, ISSN: 2542-6605.

[17] C. Bisdikian, "An overview of the bluetooth wireless technology," *IEEE Communications Magazine*, vol. 39, no. 12, pp. 86–94, 2001.

[18] U. Saeed, M. Waqas, N. Mirbahar, and M. Khuhro, "Comparative analysis of different operating systems for raspberry pi in terms of scheduling, synchronization, and memory management," *Mehran University Research Journal of Engineering and Technology*, vol. 41, pp. 113–119, Jul. 2022.

[19] R. Neves and A. C. Matos, "Raspberry pi based stereo vision for small size asvs," in *2013 OCEANS - San Diego*, 2013, pp. 1–6.

[20] I. J. Godoy *et al.*, "Groundnut – arachis hypogaea l.," in *Instruções agrícolas para as principais culturas econômicas*, ser. Boletim IAC, A. T. E. Aguiar *et al.*, Eds., 7th ed., vol. 200, Campinas: Instituto Agronômico, 2014, pp. 22–27.

[21] C. S. Pereira, R. Morais, and M. J. C. S. Reis, "Recent advances in image processing techniques for automated harvesting purposes: A review," in *2017 Intelligent Systems Conference (IntelliSys)*, 2017, pp. 566–575.

[22] R. M. Haralick, K. Shanmugam, and I. Dinstein, "Textural features for image classification," *IEEE Transactions on Systems, Man, and Cybernetics*, vol. SMC-3, no. 6, pp. 610–621, 1973.

[23] R. Song, Z. Zhang, and H. Liu, "Edge connection based canny edge detection algorithm," *Pattern Recognition and Image Analysis*, vol. 27, pp. 740–747, 2017.

[24] V. N. T. Le, S. Ahderom, B. Apopei, and K. Alameh, "A novel method for detecting morphologically similar crops and weeds based on the combination of contour masks and filtered local binary pattern operators," *GigaScience*, vol. 9, no. 3, giaa017, Mar. 2020, ISSN: 2047-217X.

[25] T. U. Rehman, M. S. Mahmud, Y. K. Chang, J. Jin, and J. Shin, "Current and future applications of statistical machine learning algorithms for agricultural machine vision systems," *Computers and Electronics in Agriculture*, vol. 156, pp. 585–605, 2019, ISSN: 0168-1699.

Courtesy of IARIA Board and IARIA Press. Original source: ThinkMind Digital Library https://www.thinkmind.org

Copyright (c) IARIA, 2025. **ISBN: 978-1-68558-273-9**

Using Radar Chart Areas to Evaluate the Sensitivity of Electronic Nose Sensors in Detecting Water Stress in Soybean

Paulo S. de P. Herrmann[1] and Matheus Santos Lucas[2]

[1] Embrapa Instrumentation (CNPDIA), [2] Institute of Mathematics and Computer Sciences, University of São Paulo
São Carlos, SP, Brazil
e-mails: paulo.herrmann@embrapa.br, matsluccas@gmail.com

***Abstract*— Water stress significantly limits soybean (Glycine max L.) productivity worldwide. Early water stress detection is crucial for implementing timely irrigation strategies to mitigate its adverse effects. Electronic noses (E-Noses), equipped with sensor arrays that detect Volatile Organic Compounds (VOCs) emitted by plants, offer a non-invasive approach to monitoring plant health. This study proposes using radar chart areas as a novel method to evaluate the sensitivity of e-nose sensors in detecting water stress in soybeans. By converting multivariate sensor responses into radar charts, we quantitatively assess sensor performance and identify the most responsive sensors to water stress-induced VOC changes. The results demonstrate that radar chart areas provide a comprehensive metric for sensor sensitivity, enhancing the effectiveness of E-Noses in agricultural applications.**

Keywords- Radar charts; Electronic nose; Soybean; Water stress; Sensor sensitivity; Volatile Organic Compounds; Plant monitoring; Precision agriculture.

I. INTRODUCTION

Recent advances have introduced electronic noses (e-noses) as innovative tools for monitoring plant health. E-Noses consists of sensor arrays that can detect specific patterns of Volatile Organic Compounds (VOCs) emitted by plants under stress conditions (see Figure 1). Changes in VOC profiles can serve as early indicators of water stress, often appearing before any visual symptoms become noticeable [1].

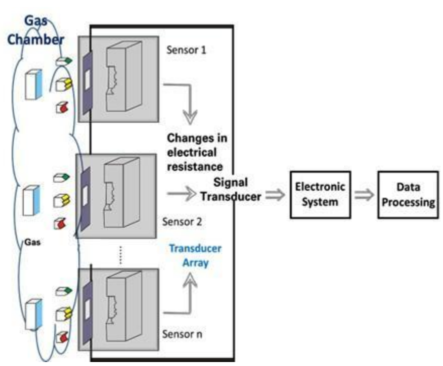

Figure 1. Block diagram of an E-nose and its components, including sensors, signal transducer, electronic system, and data processing.

Soybean (*Glycine max L.*) is a vital crop, serving as a key source of protein and oil for human consumption and animal feed. Water stress remains one of the most critical abiotic stresses affecting soybean growth and yield, leading to global economic losses. Traditional methods for detecting water stress involve physiological measurements and visual assessments, which can be labor-intensive and subjective.

The E-Nose has undergone extensive evaluation in experiments that employ statistical techniques such as Principal Component Analysis (PCA) and Linear Discriminant Analysis (LDA) to reduce the dimensionality of the collected data [2]. The dynamic mode is a distinguished method used to identify the most informative features for distinguishing between varying stress levels. A radar chart has been utilized for this purpose [1].

The radar chart, also known as a spider plot, star plot, or Kiviat figure [3], is more than just a graphical technique; it is a crucial tool in this study. It provides a straightforward way to display multivariate data on a two-dimensional plane, making it easier to visualize and compare sensor responses and ultimately evaluate the sensitivity of the sensors [1].

A radar chart presents multivariate data on axes that radiate outward from a central point. In Figure 2, each axis represents a distinct variable, with data points marked along these axes. Connecting these points forms a polygon, and calculating the area of this polygon can yield quantitative insights [4].

Figure 2. Radar Chart with an Area.

Courtesy of IARIA Board and IARIA Press. Original source: ThinkMind Digital Library https://www.thinkmind.org

Takenaka et al. [5] provided a method for evaluating the accessibility of a facility location using the area of a radar chart. The authors argue that the area of a radar chart is a more stable measure of accessibility than other measures. The main objectives of this investigation are: 1. To develop a method utilizing radar chart areas to evaluate the sensitivity of E-Nose sensors in detecting water stress in soybean plants; 2. To identify which sensors within the E-Nose array are most responsive to VOC changes associated with water stress; 3. To assess the effectiveness of radar chart areas as a quantitative metric for sensor performance in agricultural monitoring applications.

The rest of the paper is structured as follows. In Section II, we present the materials and methods. In Section III, we show the results and discuss them. Conclusion and future work directives close the article, in Section IV.

II. MATERIALS AND METHODS

Below are presented all the materials and methods used in this work, as well as the equations used to obtain the results.

A. Plant Material and Experimental Design

Soybean seeds (*Glycine max L.*) were germinated and grown in controlled greenhouse conditions at 25.0±2.0 (°C), relative humidity of 60–70 (%), and a 14-hour photoperiod. Plants were cultivated in pots containing a standardized soil mixture and watered regularly to maintain optimal moisture levels.

Measurements were taken up to the V3 phenological stage of plant development. During the experiment (21 days), the plants were divided into two groups:

- Irrigated (10 days): Continued to receive regular irrigation to maintain field capacity.

- Non-irrigated (11 days): Subjected to water deficit by withholding irrigation to reduce soil moisture content gradually.

B. Electronic Nose Setup

An electronic nose system, AlphaFox^{tm} 2000, equipped with an array of six Complementary Metal-Oxide Semiconductor (CMOS) sensors was employed. Table 1 shows each sensor in the array was selected for its sensitivity to specific VOCs known to be emitted by plants under stress:

TABLE I. THE SENSORS INSTALLED IN THE E-NOSE ARE [6].

No.	Sensor	Sensitivity property	Reference Materials
S1	T30/1	Organic compounds	Organic compounds
S2	P10/1	Combustible gas	hydrocarbon
S3	P10/2	Inflammable gas	methane
S4	P40/1	Oxidizing gas	fluorine
S5	T70/2	Aromatic compounds	Methyl benzene, xylene
S6	PA/2	Organic compounds and toxic gas	Ammonia, amines, ethyl alcohol

C. Applications in Electronic Nose

The sensitivity S (%) for each sensor was calculated using (1):

$$S(\%) = \left(\frac{R - R_0}{R_0}\right) x100 \qquad (\%) \qquad (1)$$

R_0 – Initial electrical resistance (Ω);
R – Electrical resistance varying over time (Ω)

To analyze the data obtained from the E-Nose, we utilized both radar charts and area radar charts to represent the peak sensitivity (S (%)), which was normalized using Equation 1 for each of the six sensors: S1 T30/1, S2 P10/1, S3 P10/2, S4 P40/1, S5 T70/2, and S6 PA/2, as shown in Figure 3.

An area radar chart is a specific type of radar chart that illustrates the values by displaying the area enclosed by the lines connecting the data points. Figure 4 presents the representation of both the radar chart and the area radar chart for the peak sensitivity (S (%)). Radar charts are useful for visualizing multiple variables simultaneously [7].

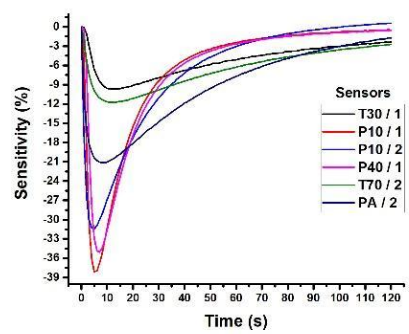

Figure 3. The variation in sensitivity, using the equation 1, of each of the six sensors in relation to time, depending on the gas sampled and measured in the E-Nose.

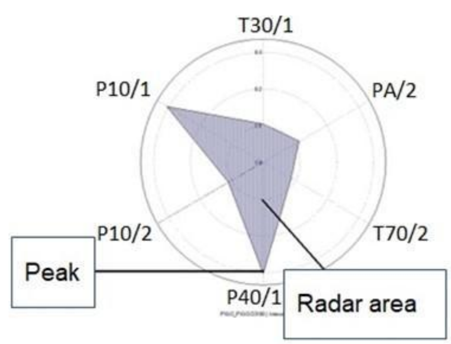

Figure 4. The radar chart and radar area from the sensitivity (%) peak to the six sensors (S1: T30/1; S2: P10/1; S3: P10/2; S4: P40/1; S5: T70/2 and S6: PA/2) from the E-Nose.

D. Calculating the Area of a Radar Chart

A radar chart is a graphical representation that effectively illustrates multidimensional data by expressing the values of each attribute in a clear and concise manner.

Courtesy of IARIA Board and IARIA Press. Original source: ThinkMind Digital Library https://www.thinkmind.org

Its 2D visualization provides a comprehensive view of the data, making it easier to analyze and understand its various dimensions [8].

The method of radar chart for Multidimensional Data: X = {X1, X2Xj, ⋯ Xn} is a multi-dimensional data set, and Xi {xi1, xi2, xi3xiN} is a N-dimensional vector. Use the radar chart when N⩾3 [8].

A method for evaluating the accessibility of a facility location using the area of a radar chart was provided by Takenaka et al [5]. The authors argue that the area of a radar chart is a more stable measure of accessibility than other measures.

The Area of the Radar (An) was calculated using (2) where Xi = Si {S1(%), S2(%), S3(%), S4(%), S5(%), S6(%)}.

To calculate the area (A_n) of the polygon formed in a radar chart:

1. Convert Polar Coordinates to Cartesian Coordinates. Each data point is defined by:

- r_i: The distance from the center to the data point along axis i (the normalized value of the variable).
- θ_i: The angle corresponding to axis i, calculated as:

$$\theta_i = \frac{2\pi(i-1)}{n} \qquad (2)$$

Where n is the total number of variables (axes). The Cartesian coordinates (x_i,y_i) are:

$$x_i = r_i \cos\theta \text{ and } {}_iy_i = r_i \sin\theta_i$$

2. Apply the Shoelace Formula: The area of the polygon can be calculated using the Shoelace Formula (3):

$$A_n = \frac{1}{2}\left|\sum_{i=1}^{n}(x_i y_{i+1} - x_{i+1} y_i)\right| \quad (\%^2) \quad (3)$$

- $x_{n+1} = x_1$ and $y_{n+1} = y_1$ to complete the loop.

The formula sums the cross-products of vertex coordinates in a specific order [1].

III. RESULTS AND DISCUSSION

The average values and standard deviations derived from radar measurements of both irrigated and non-irrigated soybean samples are illustrated in Figure 5. The data reveals a marked difference between the measurements taken in the morning and those taken in the afternoon, with the greatest standard deviation observed during the afternoon sessions. This pronounced variation may be attributed to several influencing factors, including the physiological state of the plants, which can change due to water uptake and nutrient availability.

Environmental conditions at the time of sample extraction also likely played a significant role; the fluctuating temperatures, humidity levels, and light intensity throughout the day can affect the plants responses. Furthermore, the specific growth stage of the soybeans whether they are in vegetative growth or nearing maturation—can impact how they interact with their environment. Additionally, potential errors in the syringe headspace during sampling could introduce variability in the measurements.

It is particularly noteworthy that the highest standard deviation was recorded during the afternoon. On the 22nd day of the experiment, specific weather conditions were present, characterized by overcast skies, intermittent rain, and a significant cloud cover. These factors could have influenced the plants' physiological responses, leading to the observed discrepancies in the data.

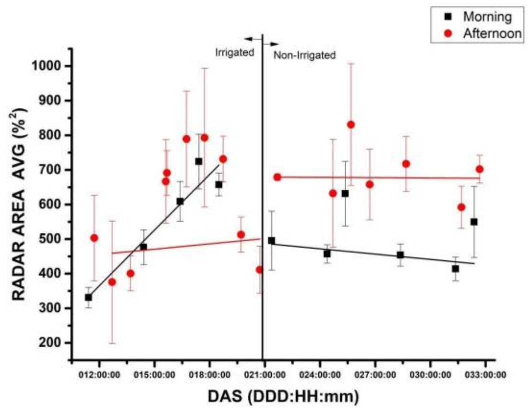

Figure 5. E-Nose measurements of gas samples taken from a chamber containing soybeans during the Days After Sowing (DAS), using the average radar area and standard deviation (n=3). The measurements are presented based on the time of day, either in the morning (9:30 a.m.) denoted by red circles or in the afternoon (3:30 p.m.) denoted by black squares. Moreover, the measurements are obtained from both irrigated and non-irrigated plants. For each DAS, gas samples are measured three times in both periods, i.e., the morning and afternoon to obtain the area radar measurement.

IV. CONCLUSIONS AND FUTURE WORK

An area radar chart is a specialized variant of a radar chart that utilizes the area enclosed by the connecting lines of data points to visually represent and compare values. Figure 4 illustrates this radar chart format, specifically highlighting the radar area at the sensitivity peak (S (%)), which indicates the maximum responsiveness of the variables in question.

Area radar charts are particularly valuable tools when analyzing and comparing the overall performance of distinct data groups, for example some experimental conditions. By presenting complex data in a clear and intuitive manner, area radar charts facilitate better decision-making and insights, allowing stakeholders to quickly grasp relationships and trends within the data. The area can be used as a valid metric to rank data.

Future work directions include integrating the method with equipment in a mobile unit to facilitate field use; integrating AI into the model; and applying the methodology to study thermal and water stress.

Courtesy of IARIA Board and IARIA Press. Original source: ThinkMind Digital Library https://www.thinkmind.org

Copyright (c) IARIA, 2025. ISBN: 978-1-68558-273-9

ACKNOWLEDGMENT

Embrapa Instrumentation supported this work and Embrapa project # 20.22.01.001.00.

REFERENCES

[1] P. S. P. Herrmann, M. Santos Luccas, E. J. Ferreira and A. Torre Neto, "Application of electronic nose and machine learning used to detect soybean gases under water stress and variability throughout the daytime," *Front. Plant Sci.* 15:1323296, 2024, doi: 10.3389/fpls.2024.1323296.

[2] S. Zorpeykar, E. Mirzaee-Ghaleh, H. Karami, Z. Ramedani and A. D. Wilson, "Electronic Nose Analysis and Statistical Methods for Investigating Volatile Organic Compounds and Yield of Mint Essential Oils Obtained by Hydrodistillation," *Chemosensors*. vol. 10, no. 11, pp. 486+, 2022, https://doi.org/10.3390/chemosensors10110486.

[3] K. W. Kolence and P. J. Kiviat, "Software unit profiles & Kiviat figures," *ACM Sigmetrics. Performance Evaluation Review*, vol. 2, no. 3, pp. 2-12, 1973, doi: 10.1145/1041613.1041614.

[4] M. J. Saary, "Radar plots: a useful way for presenting multivariate health care data," *Journal of Clinical Epidemiology*, vol. 61, no. 4, pp. 311-317, 2008, https://doi.org/10.1016/j.jclinepi.2007.04.021.

[5] T. Takenaka, K. Nakamura, T. Ukai and Y. Ohsawa, "Stability of the Area of Radar Chart to Evaluate the Accessibility of Facility Location," *Journal of the City Planning Institute of Japan*, 2018.

[6] W. Wei, J. Li and L. Huang, "Discrimination of Producing Areas of Astragalus membranaceus Using Electronic Nose and UHPLC-PDA Combined with Chemometrics," *Czech J. Food Sci.*, vol. 35, no. 1, pp. 40-47, 2017, 10.17221/126/2016-CJFS.

[7] W - Y. Liu, B.-W. Wang, Jia-Xin Yu, Fang Li, Shui-Xing Wang and Wen-Xue Hong, "Visualization classification method of multi-dimensional data based on radar chart mapping," *2008 International Conference on Machine Learning and Cybernetics*, Kunming, China, pp. 857-862, 2008, doi: 10.1109/ICMLC.2008.4620524.

[8] W. Peng, "Improved radar chart for lighting system scheme selection," *Appl. Opt.*, vol. 61, no. 19, pp. 5619-5625, 2022, doi.org/10.1364/AO.455779.

Courtesy of IARIA Board and IARIA Press. Original source: ThinkMind Digital Library https://www.thinkmind.org

Applicability Assessment of a Thermo-Formed Piezoelectret Accelerometer in Agricultural Robotics Systems

Igor Nazareno Soares*, Ruy Alberto Corrêa Altafim*, Ruy Alberto Pisani Altafim†
*Department of Electrical and Computer Engineering, Engineering School of São Carlos
University of São Paulo
São Carlos, Brazil
†Department of Computer Systems, Informatics Center
Federal University of Paraíba
João Pessoa, Brazil
e-mail: igor.soares@usp.br, altafim@usp.br, ruy@ci.ufpb.br

***Abstract*—The advancement of robotic systems in precision agriculture has increased the demand for robust, cost-effective, and customizable inertial sensors capable of operating in diverse mechanical environments. This work evaluates the applicability of a custom-developed Thermo-Formed Piezoelectret Accelerometer (TFPA) for use in agricultural robotics. The sensor, composed of a thermo-formed piezoelectret, a 30 g seismic mass, and a polyurethane foam support, was experimentally characterized over a frequency range of 50 Hz to 3.2 kHz. The sensor was calibrated using a back-to-back method with a reference accelerometer. The measured sensitivity reached a peak of 196 mV/g at 100 Hz, exhibiting a frequency response typical of a second-order underdamped system. An analytical mass–spring–damper model was developed to simulate the sensor's transfer function, and parameter tuning demonstrated strong agreement with experimental results. By comparing the TFPA's response with vibration frequency bands reported in the literature for Unmanned Aerial Vehicles (UAV), gear-driven implements, robotic arms, and harvesters, the sensor was found to be suitable for mid- to high-frequency applications, and capable of operating at even higher frequencies with signal amplification. Design parameters, such as foam thickness and Young's modulus, were shown to enable application-specific tuning of resonance and sensitivity. The TFPA's performance, mechanical robustness, and tunability highlight the potential of piezoelectret-based accelerometers for embedded vibration sensing in agricultural automation. Future work will focus on miniaturization, electronics integration, and extended calibration toward lower frequencies.**

Keywords-Piezoelectret accelerometers; vibration sensing; agricultural robotics; inertial sensors; dynamic modeling; resonance tuning; sensor calibration; frequency response analysis.

I. INTRODUCTION

The integration of robotic technologies in agriculture has significantly advanced the efficiency, precision, and sustainability of farming operations. Applications ranging from autonomous tractors and robotic arms for harvesting to Unmanned Aerial Vehicles (UAV) for monitoring and spraying have become increasingly prevalent in both research and commercial deployments [1]–[3]. These robotic systems often operate in complex, dynamic environments, subject to terrain-induced vibrations, actuator-induced oscillations, and mechanical impacts that can degrade both system performance and sensor accuracy.

Monitoring and analyzing vibration in agricultural machinery is essential for tasks, such as structural health monitoring, fault detection in powertrains, optimization of robotic motion control, and enhancement of operator safety and comfort [4]–[6]. Accelerometers are a core component in these sensing applications, typically required to operate over a wide frequency range and withstand harsh environmental conditions.

Conventional accelerometers — such as Micro-Electro-Mechanical Systems (MEMS) and piezoelectric types — are widely used but may face limitations in specific agricultural robotic applications. MEMS devices, for instance, tend to have reduced accuracy at higher frequencies or under large mechanical stress, while commercial piezoelectric sensors may be costly or require complex conditioning electronics [7].

In this context, piezoelectret-based accelerometers have emerged as a promising alternative due to their mechanical robustness, low cost, lightweight construction, and potential for customization [8]–[10]. Piezoelectrets are polymeric materials with quasi-permanent internal polarization that generate charge in response to mechanical deformation. A class of advanced materials that have garnered significant attention in scientific research and technological innovation, akin to piezoelectric polymers, they exhibit piezoelectric properties, yet are distinguished by their cellular microstructure and enhanced performance characteristics [11]. The remarkable electromechanical coupling efficiency and flexibility inherent in piezoelectrets render them particularly appealing for developing compact, lightweight, and versatile transducers and actuators [12]. When integrated with a seismic mass and elastic suspension, they can serve as effective vibration transducers [8]–[10].

This work builds upon previous research involving the development of a Thermo-Formed Piezoelectret Accelerometer (TFPA), shifting the focus toward evaluating its applicability in agricultural robotics. The sensor — composed of a thermo-formed piezoelectret element with an integrated lead seismic mass and compliant foam support — was previously characterized in terms of design and frequency response [9][10]. In this study, the TFPA is further examined through experimental calibration and analytical mass–spring–damper modeling, with emphasis on mapping its sensitivity profile to the vibration environments typical of robotic systems, such as UAVs, automated harvesters, rotary cultivators, and robotic

Courtesy of IARIA Board and IARIA Press. Original source: ThinkMind Digital Library https://www.thinkmind.org

arms. The objective is to determine the sensor's suitability for these applications by identifying the overlap between its linear response range and the dominant operational frequencies observed in the field, while also exploring mechanical tuning strategies and signal amplification techniques to broaden its functional range for practical deployment.

The remainder of this paper is organized as follows. Section II reviews related work on vibration profiles in agricultural robotics and sensor requirements. Section III details the design, construction, and calibration of the proposed TFPA sensor. Section IV presents the experimental results, theoretical modeling, and application-specific analysis. Finally, Section V concludes the study and outlines directions for future work.

II. Literature Review

Vibration analysis is a key consideration in the design, operation, and maintenance of robotic systems in agriculture. Each class of agricultural machine or robotic component presents characteristic vibration profiles, often dictated by actuation mechanisms, mechanical loads, and environmental interactions. Understanding these profiles is essential for selecting or designing compatible sensors, such as accelerometers.

A. Vibration Sources in Agricultural Robotics

Rotary Implements and Powertrains. Rotary tillers, cultivators, and gear-driven implements generate moderate to high-frequency vibrations due to blade impacts, gear meshing, and chassis resonance. Gao et al. [13] conducted a comprehensive analysis of the vibration characteristics of a tractor–rotary cultivator combination, identifying multiple frequency domains of significance. In the low-frequency range (0–100 Hz), strong energy was observed around 33 Hz in the tractor, attributed to its first-order natural frequency, and operator-sensitive cab vibrations were noted between 4.9 Hz and 6.8 Hz. In the medium-frequency range (100–500 Hz), resonance frequencies appeared around 280 Hz for the tractor cab and 350 Hz for the rotary tiller gearbox. Additionally, the rotary tiller showed less energy at low frequencies but exhibited increasing vibration activity above 250 Hz, consistent with efficient soil interaction. The gearbox demonstrated substantial high-frequency content between 750 and 1000 Hz, underscoring the mechanical complexity and resonance behavior in operational conditions.

UAVs and Aerial Systems. Drones used for crop monitoring and spraying are subject to vibrational loads arising from rotor dynamics, motor RPM fluctuations, and rapid maneuvers. Power Spectral Density (PSD) analysis has shown that UAVs exhibit distinct vibration bands depending on operational conditions. Vibrations in the 10–70 Hz range are typically linked to shaft and blade rotation at moderate throttle levels, while more intense vibrational energy occurs between 70 and 230 Hz due to high-speed rotor excitations during fast maneuvers. These frequency domains are particularly important for sensor stability and data quality in precision agriculture applications [14].

Harvesters and Cutting Mechanisms. Combine harvesters and robotic harvesters experience complex, multi-modal vibrations. Meng et al. [15] analyzed the modal response of sugar beet combine harvesters and identified significant vibration modes at 12.7 Hz due to the power input shaft and around 35 Hz related to engine excitation. In robotic harvesting systems, vibratory tools are often tuned to specific frequencies to optimize fruit detachment efficiency. Zheng et al. [16] reported optimal frequency ranges between 10 and 20 Hz for winter jujube trees, using harmonic response and transient analysis based on high-resolution 3D reconstruction. Similarly, Sola-Guirado et al. [17] assessed vibration parameters for lateral canopy shakers used in olive harvesting, highlighting the need for precise frequency targeting to maximize fruit removal while minimizing energy input.

Robotic Arms and Manipulators. Robotic arms used in fruit picking or soil sampling are subject to structure-borne resonance and actuation-induced oscillations. Badkoobehhezaveh et al. [3] conducted finite element and experimental modal analysis on a 5-Degrees-Of-Freedom (5-DOF) long-reach robotic arm designed for agricultural applications. Their study identified natural frequencies ranging from 4.4 Hz to 41.6 Hz, depending on the arm's configuration and payload, with lower modes associated with structural bending and torsional responses.

Sprayers and Operator Cabins. In large boom sprayers, low-frequency oscillations can arise from terrain coupling and the flexible dynamics of long boom arms, often requiring vibration damping systems to ensure uniform spraying. Qiu et al. [18] analyzed a spray boom-air suspension system designed to mitigate these vibrations but did not specify particular frequency ranges. Regarding operator cabins, Cutini et al. [19] reported that Whole-Body Vibration (WBV) in agricultural tractors typically occurs in the frequency range of 0.5 Hz to 80 Hz, which can pose health risks to operators if sustained for prolonged periods. These findings underscore the importance of vibration management in agricultural vehicle design.

B. Sensor Compatibility Considerations

The wide spectrum of vibration frequencies in agricultural robotics — ranging from sub-Hertz to several hundred Hertz — poses a challenge for accelerometer design. Sensors must not only detect vibrations across this range but also maintain signal linearity and adequate sensitivity. Commercial MEMS accelerometers may offer sufficient resolution at low frequencies, but often lack robustness and bandwidth for higher-frequency diagnostics. Piezoelectric sensors offer excellent high-frequency response but are typically more costly and less suited to large-scale deployment or customization [7].

The TFPA aims to fill this niche by offering a scalable, mechanically tunable alternative with sensitivity and bandwidth characteristics that can be matched to specific robotic applications.

Courtesy of IARIA Board and IARIA Press. Original source: ThinkMind Digital Library https://www.thinkmind.org

III. Materials and Methods

This section describes the experimental and analytical procedures used to evaluate the TFPA. It is divided into three subsections: the first details the design and physical construction of the sensor; the second presents the calibration method used to determine its frequency response; and the third outlines the analytical modeling approach based on a mass–spring–damper system to simulate the sensor's behavior under dynamic excitation.

A. Design and Construction of the TFPA

The developed TFPA, shown in Figure 1a, is based on a custom-fabricated piezoelectret film formed by thermal lamination of fluorinated ethylene propylene (FEP) layers, as can be seen in Figure 1c. The lamination process creates four open tubular voids, which become polarized and acquire electromechanical sensitivity after a high-voltage corona charging process. The internal microstructure behaves as a ferroelectret, producing an electric signal in response to mechanical deformation perpendicular to the film plane [20].

The piezoelectret film is coated with vacuum-deposited aluminum electrodes and coupled mechanically to a seismic mass of 30 g, composed of lead and shaped as a 10 mm-high cylinder with 18 mm diameter. This mass is housed inside a low-friction polytetrafluoroethylene (PTFE) sheath that ensures mechanical alignment and isolates lateral forces. An elastic element made of polyurethane foam, with density of 12 kg/m³, provides vertical restoring force and allows free oscillation of the mass along the sensing axis, as can be seen in Figure 1b. This configuration constitutes a single-axis, inertia-based accelerometer.

The sensing structure is enclosed within an aluminum casing measuring 74 mm in height and 51 mm in diameter. A coaxial Bayonet Neill-Concelman (BNC) connector is integrated for electrical output, with shielding ensured by the metallic housing. The final assembly offers mechanical robustness, electrical shielding, and modularity suitable for embedded applications in robotic platforms.

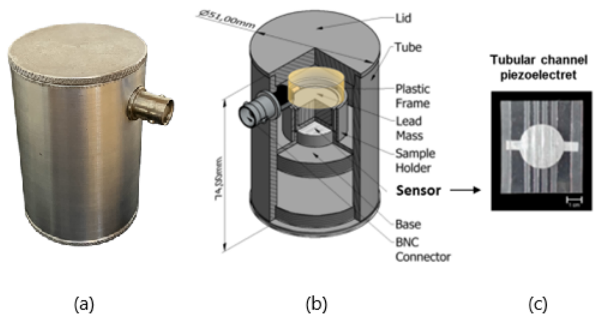

Figure 1. (a) Constructed TFPA prototype (b) TFPA internal structure (c) Piezoelectret sensor with open tubular channels

B. Calibration Procedure

The TFPA's frequency response, spanning from 50 Hz to 3.2 kHz, was characterized using the experimental setup illustrated in Figure 2 [10]. A function generator (HP model 33120A) was used to produce sinusoidal excitation signals, which were fed into a Brüel & Kjær (B&K) model 2707 power amplifier. This amplifier drove a B&K 4812 electrodynamic shaker to induce controlled vertical vibrations.

The TFPA and a reference piezoelectric accelerometer (B&K model 8305) were co-mounted atop the shaker platform to ensure identical excitation. The reference signal passed through a B&K Type 2635 conditioning amplifier, while the TFPA output was recorded directly, without additional amplification. Both signals were captured simultaneously by an Agilent Technologies DSO-X 3024A digital oscilloscope, allowing synchronized time-domain acquisition and accurate amplitude comparisons.

The system was calibrated to generate a constant sinusoidal acceleration amplitude of 9.81 m/s^2 (1 g). Sensitivity in mV/g was computed for each frequency point. This experimental data were used to identify resonance behavior, verify model predictions, and determine the operational frequency range where the sensor exhibits linear sensitivity.

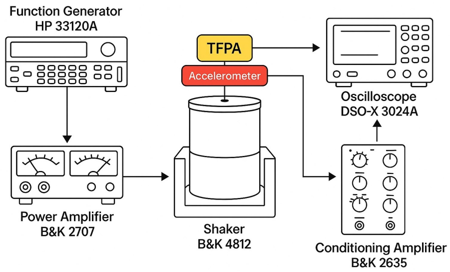

Figure 2. Experimental calibration setup showing signal generator, amplifier, shaker, TFPA and reference accelerometer

C. Analytical Modeling and Simulation

To interpret and predict the sensor behavior under dynamic excitation, the TFPA was modeled as a Single-Degree-Of-Freedom (SDOF) mass–spring–damper system [21]. The governing differential equation is:

$$m\ddot{x}(t) + c\dot{x}(t) + kx(t) = F(t) \qquad (1)$$

Here, m is the seismic mass, k is the effective stiffness of the foam, and c represents the damping coefficient. Under sinusoidal base excitation, the response was simulated in the frequency domain by evaluating the transfer function between the base acceleration and the acceleration of the seismic mass.

The elastic modulus of the foam (E) was estimated from manufacturer datasheets and literature for low-density polyurethane foams, typically ranging from 50–200 kPa [22]. The stiffness was calculated as $k = EA/L$, where A is the contact area between the foam and the mass, and L is the foam thickness.

Parametric studies were performed by varying m, E, and L to assess tuning capabilities and validate the match between experimental and theoretical frequency responses.

Courtesy of IARIA Board and IARIA Press. Original source: ThinkMind Digital Library https://www.thinkmind.org

Copyright (c) IARIA, 2025. ISBN: 978-1-68558-273-9

IV. Results and Discussions

This section presents and analyzes the results obtained from the TFPA's experimental characterization and theoretical modeling. The first subsection discusses the measured frequency response of the sensor and its resonant behavior. The second compares these experimental results with theoretical simulations. The third examines the sensor's compatibility with typical vibration profiles in agricultural robotics, and the final subsection addresses limitations of the current prototype and opportunities for future miniaturization.

A. Experimental Frequency Response

The TFPA's measured frequency response, shown in Figure 3 [10], displays a clear resonant peak centered at 100 Hz, where the sensor achieves a maximum sensitivity of approximately 196 mV/g. The sensitivity rises sharply toward this peak and falls off symmetrically beyond it, exhibiting the characteristic bell-shaped behavior of a second-order underdamped system.

Notably, the sensor does not present a flat linear region before resonance; instead, the sensitivity increases markedly between 50 Hz and 100 Hz. This non-flat rise suggests the influence of the resonance even slightly below the peak frequency. Beyond 100 Hz, the sensitivity decreases steeply and monotonically, with values dropping below 10 mV/g by 3.2 kHz. This confirms a narrow high-sensitivity band centered around the resonance and a progressively diminishing response at higher frequencies.

The experimental data confirms that the sensor operates as a classic mass–spring–damper resonant system and provides a well-defined dynamic signature suitable for matching with analytical models and mapping to real-world vibration profiles in agricultural robotics.

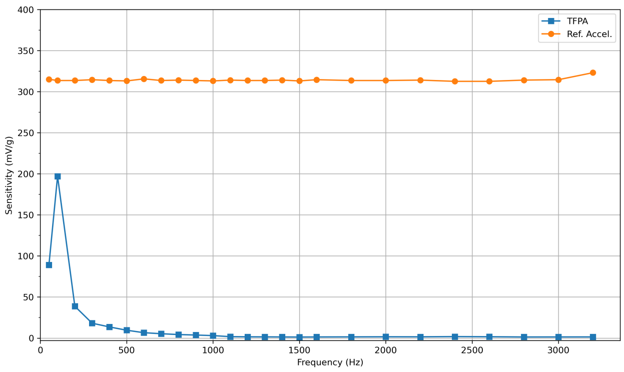

Figure 3. Frequency response of the TFPA, with a resonance frequency at 100 Hz

B. Comparison with Theoretical Models

To assess the fidelity of the TFPA's dynamic behavior, the experimentally obtained frequency response was compared to simulated models derived from a single-degree-of-freedom (SDOF) mass–spring–damper system. The transfer function used represents the mechanical gain between base excitation and seismic mass acceleration, following the classical SDOF vibration theory for underdamped systems [21][23]. These challenges are common in mechanical systems and have been extensively addressed in vibration engineering practice [24].

$$H(j\omega) = \left|\frac{X''(j\omega)}{Y''(j\omega)}\right| = \frac{1}{\sqrt{(1-(\omega/\omega_n)^2)^2+(2\zeta\cdot\omega/\omega_n)^2}} \quad (2)$$

where $\omega_n = \sqrt{k/m}$ is the undamped natural frequency, ζ is the damping ratio, and $k = EA/L$ is the effective stiffness of the foam element, with E representing Young's modulus, A the contact area, and L the foam thickness.

To illustrate the effect of key physical parameters on the sensor's dynamic behavior, preliminary simulations were conducted using three distinct configurations (A, B, and C), varying the seismic mass m, foam modulus E, and thickness L. These configurations produced resonance frequencies from approximately 30 Hz to 178 Hz, demonstrating the tunability of the system, as can be seen in Figure 4. Although none of these aligned precisely with the experimental response, they highlight the potential for application-specific optimization through mechanical design.

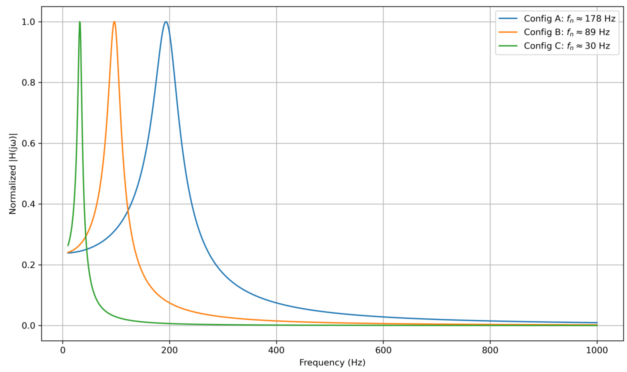

Figure 4. Simulated frequency responses for configurations A, B, and C, illustrating resonance tunability via changes in mass, stiffness, and foam thickness

A matched simulation was then performed using the known mass (30 g) and foam thickness (L = 20 mm). To align the model with the experimentally observed resonance, the required foam modulus was calculated and a damping ratio selected to reproduce the experimentally observed peak width and roll-off gradient.

Figure 5 shows the comparison between the experimental and simulated sensitivity curves. The matched model accurately reproduces the resonance peak and the roll-off profile beyond 100 Hz. This agreement validates the modeling approach and confirms the TFPA's characterization as a second-order inertial sensor. The mechanical parameters used in the simulation directly reflect physical sensor properties, demonstrating the model's predictive power for application-oriented tuning.

This result validates the mass–spring–damper model and confirms the TFPA's behavior as a second-order inertial trans-

Courtesy of IARIA Board and IARIA Press. Original source: ThinkMind Digital Library https://www.thinkmind.org

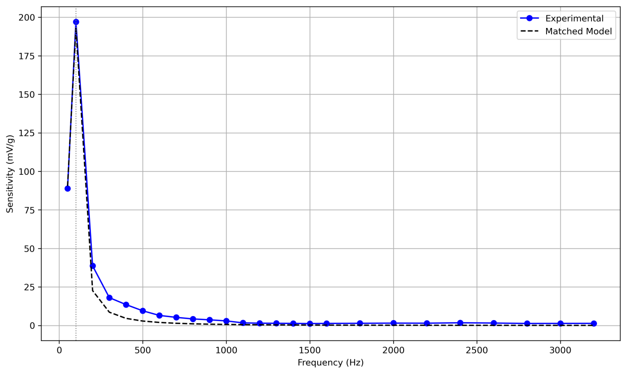

Figure 5. TFPA response comparison: experimental sensitivity data and matched simulation in physical units

ducer, whose performance can be predicted and tuned for agricultural applications.

C. Application Compatibility and Tuning Discussion

The validated dynamic model and measured frequency response of the TFPA enable a direct evaluation of its applicability across key classes of agricultural robotic systems, with respect to their dominant vibration frequency bands.

Based on the literature survey presented in Section II, the following typical operating frequencies were identified:

- **UAVs and electric motors** (70–230Hz): The TFPA's resonance at 100 Hz and its high sensitivity within the -3 dB bandwidth from 76 to 114 Hz make it well-suited for vibration monitoring in UAV propulsion systems and electric actuators, especially where higher-frequency diagnostics are required. Although the response drops off above resonance, it remains smooth and predictable, allowing for signal reconstruction with amplification techniques.
- **Gearboxes and rotary tillers** (250–1000 Hz): Although these frequencies lie above the TFPA's resonance, the sensor still provides measurable output in this range. Despite the lower gain, its linearity allows for reliable vibration detection, particularly when paired with signal conditioning or amplification techniques.
- **Robotic arms** (4–40 Hz): These structures operate below the TFPA's natural resonance. However, by modifying mechanical parameters — such as increasing the seismic mass or employing a more compliant foam — the resonance can be shifted downward, improving sensitivity in this domain.
- **Harvesting tools and vibratory shakers** (10–35 Hz): These tools often rely on carefully tuned excitation frequencies for fruit detachment. With proper tuning, the TFPA could be adapted for monitoring or feedback in such systems.
- **Sprayers and operator cabins** (0.5–80 Hz): While this range is outside the current operating band, a redesign with softer materials or mechanical amplification could enable compatibility. Additionally, whole-body vibration monitoring may benefit from a broader-band solution incorporating the TFPA in multi-sensor systems.

These observations highlight the mechanical flexibility of the TFPA architecture. Because its resonance and bandwidth are governed by design-adjustable parameters — specifically the seismic mass m and the foam stiffness $k = EA/L$ — the sensor can be customized to target specific vibrational environments. Increasing stiffness or reducing mass shifts the response toward higher frequencies, while the opposite configuration favors low-frequency applications.

Overall, the current configuration positions the TFPA as a strong candidate for medium-frequency diagnostics, with a -3 dB bandwidth of 76–114 Hz, where the sensor exhibits high sensitivity and linearity. This aligns well with the dominant frequencies encountered in UAV propulsion systems and electric drivetrain components. Beyond this range, the sensor maintains a smooth and monotonic roll-off, with a measurable response verified experimentally up to 3.2 kHz, supporting its use in higher-frequency applications, such as gearboxes and rotary tillers.

While the sensor's sensitivity peaks near its 100 Hz resonance, the measured data confirm that its post-resonance behavior remains linear and predictable. This makes the TFPA viable for both resonance-tuned use cases and broadband diagnostic tasks — especially when paired with analog amplification, impedance matching, or digital signal processing. These characteristics reinforce the TFPA's potential as a compact, tunable, and cost-effective solution for vibration monitoring in embedded agricultural robotic systems.

D. Limitations and Opportunities for Miniaturization

While the TFPA demonstrates favorable sensitivity and mechanical tunability, its current prototype form factor — measuring 74 mm in height with a 30 g seismic mass — may constrain its deployment in compact robotic platforms. The use of a relatively large lead mass and thick polyurethane foam is primarily dictated by the target resonance frequency and mechanical alignment constraints in this version.

However, piezoelectret materials themselves are inherently thin, lightweight, and flexible, offering significant potential for miniaturization. Reducing the mass and housing dimensions would naturally raise the resonant frequency, allowing adaptation to higher-frequency vibration environments. To offset the resulting loss in sensitivity, amplification strategies — either through analog front-end electronics or high-impedance buffer stages — can be introduced without compromising signal fidelity.

Additionally, engineered elastomer materials with customized stiffness and damping characteristics could enable finer control over the sensor's dynamic range and resonance tuning. This modularity supports the development of application-specific TFPA variants optimized for distinct vibration profiles across agricultural robotic systems.

Overall, future design iterations should aim to balance mass reduction, material optimization, and electronic conditioning

Courtesy of IARIA Board and IARIA Press. Original source: ThinkMind Digital Library https://www.thinkmind.org

to extend the TFPA's usability to both embedded and distributed sensing architectures in precision agriculture.

Importantly, the strong agreement between experimental data and the SDOF-based matched model further supports this pathway. It demonstrates the feasibility of predictive tuning in future designs, enabling model-driven optimization of foam stiffness, damping, and mass configurations for compact versions tailored to specific vibrational environments.

V. Conclusion and Future Work

This work presented the design, calibration, and dynamic modeling of a TFPA aimed at agricultural robotic applications. The sensor, composed of a thermo-formed FEP piezoelectret, a 30 g seismic mass, and a polyurethane foam support, was experimentally characterized across a wide frequency range (50 Hz to 3.2 kHz) using sinusoidal base excitation.

The measured sensitivity peaked at approximately 196 mV/g near 100 Hz, exhibiting a frequency response consistent with an underdamped second-order system. A single-degree-of-freedom mass–spring–damper model was developed, and the simulated response showed excellent agreement with the experimental data when foam stiffness and damping were tuned to match the observed dynamics.

Comparison with vibration frequency bands reported in the literature confirmed that the TFPA is well-suited for mid-frequency components, with a -3 dB sensitivity range between 76 and 114 Hz, including UAVs and electric actuators, while remaining functional at higher frequencies up to 3.2 kHz. Although sensitivity decreases beyond resonance, the sensor maintains linear and predictable behavior, making it viable for broadband diagnostics when supported by amplification or signal conditioning.

The TFPA's response characteristics can be tailored through geometric and material parameters, such as seismic mass, foam thickness, and Young's modulus. This enables application-specific tuning of the resonance and bandwidth. While the current prototype size may limit its use in compact platforms, the thin and lightweight nature of piezoelectret films supports future miniaturization.

These results position the TFPA as a robust, low-cost, and mechanically tunable solution for embedded vibration sensing in precision agriculture, with strong potential for future integration into adaptive and distributed robotic systems.

Building upon these findings, subsequent efforts will address the miniaturization of the TFPA, facilitating its integration into compact robotic platforms. Experimental validation in real agricultural environments is planned to evaluate long-term performance and environmental resilience. Further work will extend the calibration procedure below 50 Hz to enhance low-frequency application capabilities.

Acknowledgment

The authors thank the Brazilian funding agencies CAPES and CNPq, the University of São Paulo (Electrical and Computer Department at Engineering School of São Carlos), the Federal University of Paraíba, and the Institute of Technological Research of São Paulo (Energy Infrastructure Laboratory).

References

[1] R. P. Sishodia, R. L. Ray, and S. K. Singh, "Applications of remote sensing in precision agriculture: A review," *Remote Sensing 2020, Vol. 12, Page 3136*, vol. 12, p. 3136, 2020.

[2] T. Duckett, S. Pearson, S. Blackmore, and B. Grieve, "Agricultural robotics: The future of robotic agriculture," *UK-RAS White Papers*, 2018.

[3] H. Badkoobehhezaveh, R. Fotouhi, Q. Zhang, and D. Bitner, "Vibration analysis of a 5-dof long-reach robotic arm," *Vibration 2022, Vol. 5, Pages 585-602*, vol. 5, pp. 585–602, 2022.

[4] M. Hosseinpour-Zarnaq, M. Omid, and E. Biabani-Aghdam, "Fault diagnosis of tractor auxiliary gearbox using vibration analysis and random forest classifier," *Information Processing in Agriculture*, vol. 9, pp. 60–67, 2022.

[5] J. Xu, T. Jing, M. Fang, P. Li, and Z. Tang, "Failure state identification and fault diagnosis method of vibrating screen bolt under multiple excitation of combine harvester," *Agriculture 2025, Vol. 15, Page 455*, vol. 15, p. 455, 2025.

[6] J. H. Kim, J. T. Dennerlein, and P. W. Johnson, "The effect of a multi-axis suspension on whole body vibration exposures and physical stress in the neck and low back in agricultural tractor applications," *Applied Ergonomics*, vol. 68, pp. 80–89, 2018.

[7] T. Wu *et al.*, "Research status and development trend of piezoelectric accelerometer," *Crystals 2023, Vol. 13, Page 1363*, vol. 13, p. 1363, 2023.

[8] J. F. Alves *et al.*, "An accelerometer based on thermoformed piezoelectrets with open-tubular channels," *Annual Report - Conference on Electrical Insulation and Dielectric Phenomena, CEIDP*, vol. 2020-October, pp. 524–526, 2020.

[9] I. N. Soares *et al.*, "New design for a thermo-formed piezoelectret-based accelerometer," in *ALLSENSORS 2023, The Eighth International Conference on Advances in Sensors, Actuators, Metering and Sensing*, IARIA, 2023, pp. 21–24.

[10] I. N. Soares, R. A. C. Altafim, R. A. P. Altafim, and M. M. Tokoro, "Investigation of thermo-formed piezoelectret accelerometer under different electrodynamic vibration conditions," in *ALLSENSORS 2024, The Ninth International Conference on Advances in Sensors, Actuators, Metering and Sensing*, IARIA, 2024, pp. 32–37.

[11] M. M. Moreira *et al.*, "Piezoelectrets: A brief introduction," *IEEE Sensors Journal*, vol. 21, pp. 22 317–22 328, 2021.

[12] X. Qiu *et al.*, "Ferroelectrets: Recent developments," *IET Nanodielectrics*, vol. 5, pp. 113–124, 2022.

[13] Y. Gao *et al.*, "Analysis of vibration characteristics of tractor–rotary cultivator combination based on time domain and frequency domain," *Agriculture 2024, Vol. 14, Page 1139*, vol. 14, p. 1139, 2024.

[14] C. Ge, K. Dunno, M. A. Singh, L. Yuan, and L. X. Lu, "Development of a drone's vibration, shock, and atmospheric profiles," *Applied Sciences 2021, Vol. 11, Page 5176*, vol. 11, p. 5176, 2021.

[15] J. Meng, Z. Li, W. Xian, F. Li, and Y. Li, "Modal response and vibration characteristics of sugar beet combine harvester frame," *Engenharia Agrícola*, vol. 44, e20240054, 2024.

[16] Z. Zheng *et al.*, "Characterising vibration patterns of winter jujube trees to optimise automated fruit harvesting," *Biosystems Engineering*, vol. 248, pp. 255–268, 2024.

[17] R. R. Sola-Guirado *et al.*, "Vibration parameters assessment to develop a continuous lateral canopy shaker for mechanical harvesting of traditional olive trees," *Spanish Journal of Agricultural Research*, vol. 14, e0204–e0204, 2016.

[18] W. Qiu *et al.*, "Analysis of factors influencing vibration suppression of spray boom-air suspension for medium and small-scale high-clearance sprayers," *Sensors 2021, Vol. 21, Page 6753*, vol. 21, p. 6753, 2021.

Courtesy of IARIA Board and IARIA Press. Original source: ThinkMind Digital Library https://www.thinkmind.org

[19] M. Cutini, M. Brambilla, and C. Bisaglia, “Whole-body vibration in farming: Background document for creating a simplified procedure to determine agricultural tractor vibration comfort,” *Agriculture 2017, Vol. 7, Page 84*, vol. 7, p. 84, 2017.

[20] R. A. P. Altafim *et al.*, “Template-based fluoroethylenepropylene piezoelectrets with tubular channels for transducer applications,” *Journal of Applied Physics*, vol. 106, p. 014 106, 2009.

[21] D. J. Inman, *Engineering Vibration*, 4th ed. Pearson Education, 2013.

[22] D. Zenkert, *An Introduction to Sandwich Construction*. EMAS Publishing, 1995.

[23] S. S. Rao, *Mechanical Vibrations*, 6th ed. Pearson, 2017.

[24] C. M. Harris and A. G. Piersol, *Harris’ Shock and Vibration Handbook*, 5th ed. McGraw-Hill, 2002.

Courtesy of IARIA Board and IARIA Press. Original source: ThinkMind Digital Library https://www.thinkmind.org

A Prototype of a Monitoring Sensor System for Stored Grains in a Real-world Setting

Jose Dalton Cruz Pessoa[1], Sérgio da Silva Soares[2], Victor Bertucci Neto[1]

[1]Embrapa Instrumentação, São Carlos, SP, Brasil
[2]CRIAR Space Systems, Ribeirão Preto, SP, Brasil
e-mail: jose.pessoa@embrapa.br, sergio@grupocriar.com.br, victor.bertucci@embrapa.br

***Abstract*— This paper presents a further step in the sequence of studies and developments of instrumentation for monitoring grains in Silo bags. The final deliverable of this project will be a monitoring system that includes sensor capsules for detecting the ecosystem conditions within a Silo bag: the electronics, communication protocols, a low Earth orbit satellite, and a central data storage and analysis unit. This document presents partial results from the relevant environment application of a sensor-capsule model. In a bag of approximately 1 cubic meter containing maize, three capsules were installed in positions that were expected to detect different environmental conditions within the bag. Probe 63 was installed near the upper surface of the bag, more exposed to solar radiation. Probe 64 was installed near the center of the bag; and Probe 65 was installed near the base of the bag, where it received less solar radiation but was more exposed to heat transfer by conduction. The experiment served as a proof of concept for the terrestrial component of the monitoring system, and with it, the requirements for its classification at Technology Readiness Level (TRL) 7 were finalized. The experiment also allowed for the identification of the effect of sensor position within the Silo and the correlation between the variables (temperature, humidity, and CO2 concentration).**

Keywords – Silo; Silo-bolsa; grain; soy; corn.

I. INTRODUCTION

The National Supply Company (Companhia Nacional de Abastecimento - Conab) [1] estimates that the 2024/2025 harvest will yield 322.3 million tons of grains, comprising 166.33 million tons of soybeans and 119.6 million tons of maize. In the first half of 2024, the storage capacity in Brazil reached 222.3 million tons, equivalent to 69% of the harvest.

The deficit in storage capacity impacts the country's ability to stockpile food, compels producers to sell their product at market price during the harvest period, and tends to reduce grain quality, and consequently its value, when harvesting is not performed under ideal moisture conditions.

Grain storage, for regulatory stock or waiting for more favorable pricing, can be carried out in some types of storage units: Conventional warehouse, Bulk Storage Warehouse, Silo, and Silo bag. The primary difference between these storage facilities lies in the form in which the products are stored (bulk or packaged) and the warehouse structure.

The Conventional Warehouse is intended for the storage of packaged goods (bags, boxes, bales, etc.). It features a flat floor and a single compartment. The Bulk Storage Warehouse is an adaptation of a conventional warehouse for storing grains in bulk. It has a flat floor, which can complicate grain unloading, but it is a more economical alternative for bulk handling.

The Silo is a structure specifically designed for the preservation of large volumes of grains. They are typically constructed in a vertical cylindrical shape. Modern Silos often include temperature monitoring and ventilation systems to prevent grain overheating. These Silos may also feature conveyor systems, screw conveyors, and elevators to facilitate grain loading and unloading.

Silo bags are large, flexible plastic bags made of high-resistance polyethylene, occasionally doped with a substance that reduces the deleterious effects of UV radiation on the plastic. The Silo bag should be installed in an area with low slope (up to 5%, for example) and good drainage. Compared to the previous options, it presents a significantly lower cost. For filling the Silo bag, the use of an implement called a grain bagger is advisable, and for grain extraction, an implement called a Silo bag unloader is used. The load capacity of the Silo bag depends on its length, which is generally 30m to 90m, where it is possible to store hundreds of tons of grains.

Storage units are designed or adapted to provide temperature and humidity conditions suitable for grain preservation. However, controlling these variables within such a large volume is very challenging. Furthermore, storage units exhibit varying levels of airtightness, consequently allowing for gas exchange and potentially the entry of insects and rodents. Additionally, it is not always possible to choose the initial storage conditions, notably the grain moisture content.

Silo bags exhibit good airtightness due to being made of a flexible yet resistant plastic (Low-Density Polyethylene; LDPE). This type of polyethylene allows for the fabrication of bags that conform to the volume of the stored grains. It also possesses good tensile strength and impact resistance, essential characteristics for withstanding the weight of the grains and climatic conditions. Additives, such as UV stabilizers, protect the material from degradation caused by solar exposure. Other additives can be incorporated to enhance tear and puncture resistance, as well as to reduce gas permeability. The polyethylene forming the body of the Silo bag can also be multi-layered to improve its mechanical and permeability properties.

The Silo bag remains stationed in the field, subject to climatic conditions and the surrounding ecosystem. The

Courtesy of IARIA Board and IARIA Press. Original source: ThinkMind Digital Library https://www.thinkmind.org

primary challenges are the initial conditions and attacks by animals that can rupture the Silo. Generally, rodents cause small breaches. In Brazil, legislation has complicated the hunting of feral pigs (crossbreed of wild boar and domestic pig), which, being of medium to big size, can cause significant damage to crops and the Silo. All of these variables can deteriorate the cargo, or a portion thereof, if countermeasures are not implemented to prevent or mitigate the damage.

Controlling the internal ecosystem of the Silo bag is not feasible. However, automated monitoring of the Silo bag is also challenging, as it relies on a power source, a robust and reliable data transmission system, and the encapsulation of electronics with adequate Ingress Protection (IP) rating. In the agricultural environment, encapsulations with IP65, IP67, and IP69K ratings are more common [2].

Subsequently, following a brief review in Section II, we will describe the prototype utilized in this work in Section III and the experimental setup in Section IV. In Section V, we will present a graphical analysis, and in Section VI, a correlation analysis of the data, prior to the conclusions in Section VII.

II. A Short Review

The state of the art for maintaining the quality of grains stored in Silo bags includes an updated review of topics such as storage techniques [3], modified atmosphere effects, pest control methods [4], and microorganism control methods, property security, sensors and monitoring methods [5], data analysis and mining methods [6], and specific experimental results. As a comprehensive topic, it can be summarized that the objective of this technical-economic area is to reduce post-harvest grain losses. The approach has been to identify relevant variables and their respective sensors, data transmission methods, and data analysis and mining.

Temperature and humidity sensors enable the continuous monitoring of internal conditions within the Silo bag. Carbon dioxide (CO2) sensors are beginning to be used, but their cost impacts adoption by farmers. The equivalent to these measurements would be oxygen (O2) concentration measurement. Both monitor the modified atmosphere inside the Silo bag, indicating the effectiveness of the sealing and biological activity (respiration of grains, insects, and fungi).

Vibration and movement sensors can detect damage to the Silo bag structure or unauthorized movements, aiding in property security and pest control. However, the adoption of this type of sensor requires the development of signal conditioners to filter out common interference in the field.

Other aspects of monitoring for loss reduction during storage, such as the complex system of data transmission in the field and anomaly warning algorithms, are usually handled within companies.

Despite advances, field-scale monitoring still demands answers to questions: How does sensor position affect the time series, and; How does position affect the correlation between variables. This work explores these two questions.

III. The Prototype

Temperature, humidity, and CO2 sensors were utilized in each measurement unit: Probe 63, Probe 64, and Probe 65. The probes have a cylindrical format divided into two parts: the lance and the capsule. The lance is inserted into the Silo, and the capsule remains outside the Silo.

Figure 1 illustrates a probe that encapsulates three sensor elements with their respective electronics, one electronic circuit for signal pre-processing, and another responsible for the sensor's communication with a receiving base.

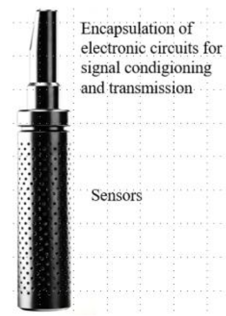

Figure 1. Probe prototype. The probe is composed of sensors, conditioning electronics, and antenna.

Commercial sensor elements were utilized, but all signal conditioning electronics were developed in the CRIAR laboratories. The CO2 sensor is based on the two-beam Non-Dispersive Infrared (NDIR) technology and detects within a range of 0 - 40%, with a resolution of 0.01% Vol. The operating temperature range is between -25ºC and 55ºC.

The relative humidity of the air inside the Silo bag was measured with a resolution of 0.05 to 0.4 %RH and a typical accuracy of +/-3.0 %RH.

In this work, a version of the telemetry system for Silo bags (e-SILOBAG) [7] was utilized, which included sensors, data transmission protocol, data reception and storage infrastructure, and analysis, as shown in Figure 2.

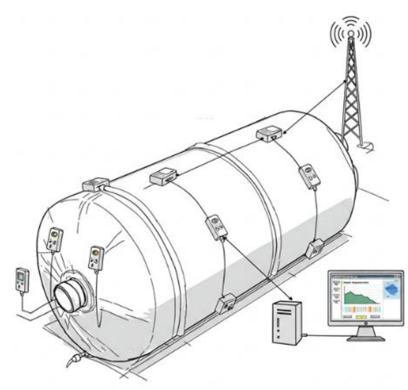

Figure 2. Ground communication network is formed by probes installed in the Silo, a hub (data concentrator) coupled to a ground station that transmits the signal to a database in the processing unit.

Courtesy of IARIA Board and IARIA Press. Original source: ThinkMind Digital Library https://www.thinkmind.org

During the proof of concept of this system version, limitations in power supply were detected, which were quickly resolved, allowing for the continuation of the experiment.

IV. EXPERIMENTAL SETUP

A small storage Silo, constructed from the plastic used in Silo bags and with an approximate volume of 1m³, was positioned on a concrete surface, adjacent to a masonry wall. The Silo was filled with maize grains.

Probes 63, 64, and 65 were installed (these labels were arbitrarily assigned), as depicted in Figure 3. Probes 63 and 65 were positioned 20cm from the Silo surface, and probe 64 was positioned 40cm from the surface, near the center of the Silo.

The probes were installed in non-equivalent positions. Probe 63 received more direct solar radiation, as did probe 64. Probe 65 received less direct solar radiation but was closer to the lower surface of the Silo, which received more heat via conduction.

All three probes are equipped with 2 sensor sets: one internal to the Silo and the other external to the Silo. The internal set measures internal Temperature, internal Humidity, and CO2. The external set measures external Temperature and external Humidity.

Measurements were taken every 60 minutes, and the data were transmitted to a concentrator and from there to a database. The measurements were conducted over a period of 133 days.

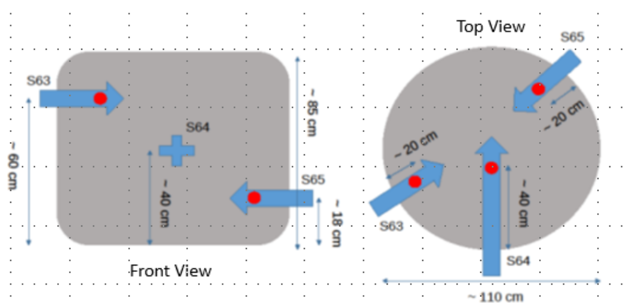

Figure 3. Position of probes and sensors within the Silo bag. Probes 63 and 65 measured at 20 cm from the surface, and probe 64 at 40 cm. Probe 63 received more direct solar radiation.

V. GRAPHICAL ANALYSIS

Figure 4 presents the behavior of CO2 concentration (%) measured by the three probes. The data were normalized (Z-score normalization), and 12-period moving averages were calculated.

Throughout the experiment, the CO2 (Figure 4) concentration was practically the same across the three probes, indicating that this variable tends to be independent of the position within the Silo.

The graphs suggest that the behavior of the concentration went through at least three phases: up to day 27, when the first increase in concentration occurs; between days 45 and 95, when the second increase occurs; and after day 105, when the concentration stabilizes and tends to decrease.

Upon opening the bag, we identified the presence of a small population of maize weevils (*Sitophilus zeamais*). The first phase of the CO2 curves may be associated with the increased respiration of the grains, the second phase with the development of the weevil population, and the third phase with the equilibrium state and degradation of the ecosystem.

Figure 5 presents the time series of the internal temperatures measured by the three probes. It is observed that the three probes exhibit the same general behavior; that is, the trend of increase or decrease is followed by all three probes.

Probe 63 shows greater temperature variations; that is, over some days, the amplitude of the diurnal variations is larger than that of probe 65, which indicates the relative position of the probes with respect to the sun.

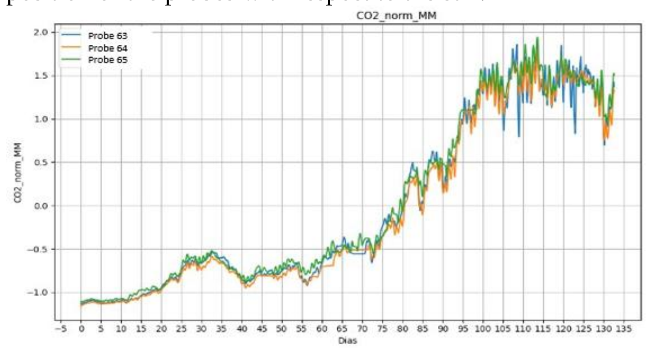

Figure 4. Behavior of CO2 concentration, measured by the three probes.

Probe 65, located in a more shaded area, measures the effects of the surface on which the Silo rests, which is made of concrete. Concrete has high thermal diffusivity, rapidly transmitting heat absorbed from solar radiation.

Until approximately day 55 of the experiment, the internal temperature of probe 63 tends to follow the troughs of the internal temperature of probe 65. Afterward, it tends to follow the peaks. The explanation for this behavior is not yet clear.

The temperature variations, with greater amplitude, near the Silo surface (probes 63 and 65) indicate an environment more conducive to the development of fungi and bacteria. Probe 64, whose measurements were taken near the center of the Silo, also exhibits significant oscillations, but with lower frequency.

The comparative analysis of these graphs shows that the internal temperature of the Silo is not uniform, and that it depends on the probe's position relative to direct (e.g., Sun) and indirect (e.g., soil) heat sources, and the sensor's depth within the Silo. The explanation for the temperature behavior at the center of the Silo can be attributed to the thermal conductivity, thermal diffusivity, and specific heat of the grain. These properties, however, depend on the grain's moisture content.

For maize grains, according to Andrade et al. [8], the Specific Heat varies by 25%, linearly (r^2=0.9583), for moisture contents (% wb) between 9% and 17%. Within the same grain moisture range, the Thermal Conductivity varies, linearly (r^2=0.9525), by 25%. The authors conducted these measurements in a volume of 0.05 m³.

Courtesy of IARIA Board and IARIA Press. Original source: ThinkMind Digital Library https://www.thinkmind.org

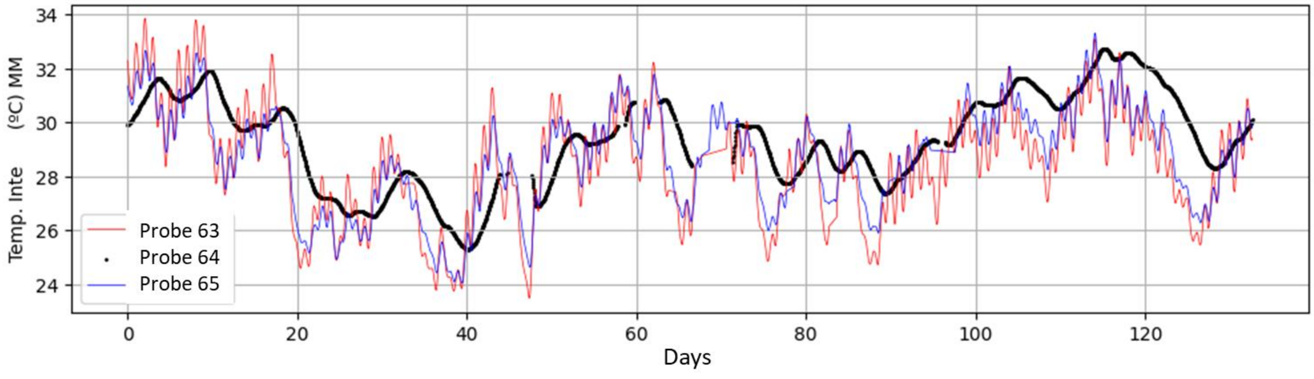

Figure 5. Internal temperature of the Silo, measured by three probes. Two of them (63 and 65) positioned near the surface. Probe 63 received more direct solar radiation.

TABLE 1. CORRELATION MATRIX BETWWEN THE VARIABLES MEASURED BY PROBE 63.

PROBE 63	Temp. Ext (ºC)	Umid Ext (%)	Temp. Int (ºC)	Umid Int (%)	CO2 Int (%)
Temp. Ext (ºC)	1,00	-0,90	0,32	-0,81	0,01
Umid Ext (%)	-0,90	1,00	-0,54	0,82	0,10
Temp. Int (ºC)	0,32	-0,54	1,00	-0,23	0,05
Umid Int (%)	-0,81	0,82	-0,23	1,00	0,19
CO2 Int (%)	0,01	0,10	0,05	0,19	1,00

TABLE 2. CORRELATION MATRIX BETWWEN THE VARIABLES MEASURED BY PROBE 65

PROBE 65	Temp. Ext (ºC)	Umid Ext (%)	Temp. Int (ºC)	Umid Int (%)	CO2 Int (%)
Temp. Ext (ºC)	1,00	-0,67	0,34	-0,49	-0,01
Umid Ext (%)	-0,67	1,00	-0,72	0,28	0,29
Temp. Int (ºC)	0,34	-0,72	1,00	0,30	0,24
Umid Int (%)	-0,49	0,28	0,30	1,00	0,51
CO2 Int (%)	-0,01	0,29	0,24	0,51	1,00

VI. CORRELATION ANALYSIS

Tables 1 and 2 show the correlation between the variables measured in the experiment, for which the Silo model had a volume of 1m³.

A. Temperatura

The measurements from Probe 63, which was more exposed to direct radiation, show that the External Temperature exhibits a strong negative correlation with the Internal Humidity (-0.81) and a weak positive correlation with the Internal Temperature (0.32). The Internal Temperature exhibits a very weak negative correlation with the Internal Humidity (-0.23).

These values may indicate that the independent variable of the system, according to Probe 63, is the External Temperature, with an indirect effect on the other variables. The Internal Temperature, for example, depends on the thermal behavior of the grains and their moisture content. The Silo is a complex system whose behavior depends on multivariate relationships and, in at least some cases, on unidentified variables (such as the unidentified presence of microorganisms).

The measurements from Probe 65 show that the External Temperature exhibits a weak (almost moderate) negative correlation with the Internal Humidity (-0.49) and a weak positive correlation with the Internal Temperature (0.32). The Internal Temperature exhibits a weak (almost very weak) positive correlation with the Internal Humidity (0.30).

This set of values presents the same pattern of behavior as Probe 63, but with the effect of Probe 65's position near the ground. In other words, to better understand the relationship between the External Temperature and the Internal Humidity through a mathematical model, it would be convenient to consider the effect of heat transfer from the ground to the Silo.

Courtesy of IARIA Board and IARIA Press. Original source: ThinkMind Digital Library https://www.thinkmind.org

B. CO2

The correlations of CO2 concentration with the other variables, according to the measurements from Probe 63, were very weak or negligible.

At the position of Probe 65, which was less exposed to direct solar radiation, the strongest correlation was moderate (0.51), with the Internal Temperature. The CO2 concentration depends on the respiration rate of biotic agents. For maize grains, and constant moisture content, the respiration rate increases with temperature [9], as it does for the maize weevil (*Sitophilus zeamais*) [10]. The effect of temperature on the development of fungi, yeasts, and bacteria requires an analysis of the microbiota, as each species performs its metabolic functions most efficiently within different temperature ranges.

Upon opening the Silo, a significant population of bacteria, fungi, yeasts, and insects was not detected (qualitative observation), suggesting that the correlation between CO2 concentration and Internal Temperature was mainly due to the volume of stored grains. The stronger correlation at the lower position (Probe 65) may indicate a slightly greater presence of microorganisms at the base than at the upper surface of the Silo.

When analyzing the correlations in phase 1 (Figure 4; 0 to 27 days) and phase 2 (Figure 4; 45 to 95 days), the values are different. Regarding Internal Temperature, in phase 1, the correlation was strongly negative for probes 63 (-0.71) and 65 (-0.78), and very strongly negative for probe 64 (-0.93). That is, the increase in temperature reduced the CO2 concentration on the scale of diurnal variations. The negative correlation appears to contradict the expected behavior of respiration in relation to temperature, but the measurements refer to the air temperature inside the Silo, which is not the same as the grain temperature.

Regarding Internal Humidity, the highest value was a moderate negative correlation (-0.66) at probe 65. In this case as well, a positive correlation was expected, but in the same way as for temperature, the sensor measures the air humidity and not the grain moisture content.

VII. CONCLUSIONS AND FUTURE WORK

In a Silo bag model of approximately 1 m³, three probes were installed. Each probe measured temperature, humidity, and internal concentration within the Silo, as well as external temperature and humidity. One probe (63) was installed on the upper lateral side, another on the lower lateral side (65), and both measured near the surface. The third probe (64) was installed on the front side and measured near the Silo's center.

The measurements were enabled and facilitated by the monitoring system developed by CRIAR, where the probes transmit their data to a concentrator, and the concentrator transmits it to a server.

During the 133 days of the experiment, deficiencies in the electronic design were detected that affected power consumption. The problem was resolved, and the new version will feature a solar panel to ensure automatic battery recharging.

The temperature, relative humidity, and CO2 concentration remained within the operational specifications of the sensors (-25ºC to 55ºC; 0 to 95% RH; 0 to 40%). The experiment contributed to understanding the effect of probe position within the Silo and to the development of algorithms for data analysis. Soon, it will be possible to mine information of interest, especially regarding the quality of the stored grains and any damage to the Silo bag structure. The version used is not the latest available but contains the main elements of the system, such as the communication protocols and signal conditioning electronics, which allowed for the proof of concept to be carried out and to indicate some desirable improvements.

The study validated the proof of concept of the measurement and data transmission system in a relevant environment and paved the way for field-scale testing.

REFERENCES

[1] Conab, https://www.conab.gov.br/ultimas-noticias/5895-producao-de-graos-2024-25-e-estimada-em-322-3-milhoes-de-toneladas-com-clima-favoravel-para-as-culturas-de-1-safra, [retrieved: May, 2025].

[2] IEC, International electrotechnical Commission. <https://www.iec.ch/ip-ratings>, [retrieved: apr, 2025].

[3] B. J. Olorunfemi and S. E. Kayode, “Post-Harvest Loss and Grain Storage Technology - A Review,” Turkish Journal of Agriculture - Food Science and Technology, v. 9, n.1, pp. 75-83, 2021.

[4] A. F. Rozado, L. R. A. Faroni, W. M. I. Urruchi, R. N. C. Guedes, and J. L. Paes, “Aplicação de ozônio contra Sitophilus zeamais e Tribolium castaneum em milho armazenado (Ozone application against Sitophilus zeamais and Tribolium castaneum in stored corn),” Revista Brasileira de Engenharia Agrícola e Ambiental (Brazilian Journal of Agricultural and Environmental Engineering), v.12, n.3, pp.282–285, 2008.

[5] L. Labrot–Rhodes, E. Campo, and P. Poujaud, “Review of monitoring systems for stored grains in amodified atmosphere,” Heliyon v.11, 2025.

[6] H. Yu, B. Li, D. Shen, J. Cao, and B. Mao, “Study on prediction model of grain post-harvest loss,” Procedia Computer Science 122, pp. 122–129, 2017.

[7] e-SILOBAG. <https://e-Silobag.com.br/>, [retrieved: May, 2025].

[8] E. T. de Andrade, S. M. Couto, D. M. De Queiroz, and A. B. Peixoto, “Determinação de propriedades térmica de grãos de milho,” Ciênc. Agrotc. Lavras, v.28, n.3, pp. 488-498, 2004

[9] F. J. M. Valle, A. Gaston, R. M. Abalone, D. A. de la Torre, C. C. Castellari, and R. E. Bartosik. “Study and modelling the respiration of corn seeds (Zea mays L.) during hermetic storage,” Boisystems Engineering, 208, pp. 45-57, 2021.

[10] M. A. G. Pimentel, L. R. D’A. Faroni, M. D. Batista, and F. H. da Silva, “Resistance of stored-product insects to phosphine,” Pesq. Agropec Bras. vol. 43, pp. 1671-1676, 2008.

Courtesy of IARIA Board and IARIA Press. Original source: ThinkMind Digital Library https://www.thinkmind.org

Copyright (c) IARIA, 2025. ISBN: 978-1-68558-273-9

Sensor-Based Platform for Evaluation of Atmospheric Carbon Sequestration's Potential by Maize Crops

Paulo E. Cruvinel[1,2], Luiz A. Colnago[1]
[1]Embrapa Instrumentation, São Carlos, SP, Brazil
[2]Post-Graduation Program in Computer Science - Federal University of São Carlos, SP, Brazil
Email: paulo.cruvinel@embrapa.br, luiz.colnago@embrapa.br

***Abstract*—The development of sensor-based techniques has been allowing advanced studies for agriculture's decision support systems. This paper discusses an innovative sensor-based method for the evaluation of CO_2 sequestration potential from the atmosphere by agricultural crop environments. This study has led to new insights into the management of crop fields for food and biomass production for energy. It also brings together information related to the carbon sequestration potential, which can allow opportunities not only for the use of sensors and related techniques in soil science but also for value aggregation for the agricultural process and environmental care. For validation, an experimental maize crop area has been used. Besides, studies about atmospheric carbon sequestration potential were evaluated. Such analyses have become possible by using vegetation indexes related to the normalized difference vegetation and the modified chlorophyll absorption in reflective, both calculated with data acquired using a multispectral sensor. In addition, three other sensors have been used for solar light intensity, soil water content, and air temperature measurements. Results have shown the spatial variability of the carbon sequestration potential, as well as its temporal variability when considering different phenomenological phases of the maize culture. Furthermore, a positive correlation with plant management and the carbon sequestration potential has been found, i.e., leading to an adequate new sensor-based descriptor for atmospheric carbon sequestration by plants evaluation.**

Keywords-light-band sensors, carbon sequestration, agricultural sensor, intelligent instrumentation.

I. INTRODUCTION

Atmospheric carbon sequestration is the process of capturing and storing carbon dioxide (CO2) from the air. It is a way to reduce the amount of CO_2 in the atmosphere and slow climate change occurrences. CO_2 sequestration by living organisms can be stored in plants, animals, soil, oceans, and other bodies of water, like lakes, rivers, and watersheds. In fact, this can be done based on reforestation, agricultural crops, and wetland restoration, i.e., considering sustainable management and good environmental practices [1]. In addition, it is important to observe that still there are other methods related to the use of technologies that extract CO_2 directly from the atmosphere.

Beyond considering the use of agricultural crops for food, fiber, and biomass energy production, atmospheric carbon sequestration can also be considered. To get a better understanding of this process, one may think of the concepts related to photosynthesis [2]. Photosynthesis is a photochemical reaction. It uses light energy to convert carbon dioxide and water into oxygen and glucose. Photosynthesis is also observed in other organisms besides green plants. These include several prokaryotes, such as cyanobacteria, purple bacteria, and green sulfur bacteria. These organisms exhibit a photosynthesis system just like green plants. The glucose produced during photosynthesis is then used as a carbon source and fuel for various cellular activities and growth. The by-product of this physiochemical process is oxygen [3].

The leaves of plants contain microscopic cellular organelles known as chloroplasts. Each chloroplast contains a green-colored pigment called chlorophyll. In fact, chlorophyll molecules absorb light energy, whereas carbon dioxide enters the leaves through the tiny pores of stomata located in the epidermis [4].

The glucose produced in photosynthesis is then sent to the roots, stems, leaves, fruits, flowers, and seeds. In other words, the plants use this sugar as an energy and carbon source, which helps them to grow. Glucose molecules, water, and other nutrients are used in several biochemical processes, producing a larger number of small organic compounds as well as more complex carbohydrates like cellulose and starch.

The following factors can affect the photosynthesis process, which means light intensity, concentration of CO_2, temperature, water availability, and air pollution, since pollutants and other particulates may settle on the leaf surface, blocking the pores of stomata [5].

Increasing either the light intensity or the CO_2 concentration in the air results in raising the photosynthesis rate. On the other hand, low light intensity or low CO_2 concentration results in a lower photosynthesis rate, respectively. For efficient photosynthesis processes, it is important to have a temperature range between 25°C and 35°C.

Likewise, since water is an important factor in photosynthesis, its deficiency can lead to problems in the intake of CO2. This occurs due to the fact that low water availability from soil leads to the refusal of stomatal opening to retain the amount of water they have stored inside.

However, despite these factors being critical, the chlorophyll content in the leaves must be evaluated to estimate the potential of crops for carbon sequestration from the atmosphere.

Chlorophyll is a green pigment found in the chloroplasts of the plant cell and in the mesosomes of cyanobacteria. In fact, they are used by plants and bacteria to absorb energy from sunlight. Most land plants have two forms of chlorophyll, designated as A and B. In such a context,

Copyright (c) IARIA, 2025. ISBN: 978-1-68558-273-9

differences permit the absorption of different wavelengths of light. Figure 1 shows a typical chlorophyll chemical structure found in plants [6].

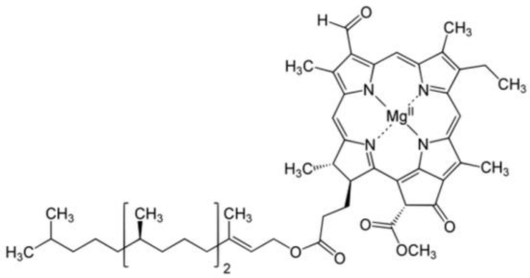

Figure 1. The typical structure of Chlorophyll A in plants [6].

The adequate estimation of leaf chlorophyll content is also important in monitoring the growth status of plants in agriculture, such as, for instance, in maize production based on precision farming management. Therefore, for the evaluation of chlorophyll content in plants, one may use different vegetation indexes, which can be obtained based on the use of multispectral data collected with adequate sensors.

This paper presents a sensor-based method for atmospheric CO_2 sequestration potential evaluation in agricultural crop management.

After this introduction in Section I, this paper is structured as follows. Section II presents the materials and methods, including not only the used materials and the agricultural experiments' descriptions for the method's validation but also the adopted sensor-based architecture and the computational model for the CO_2 sequestration potential index evaluation by crops. Section III presents the results and discussions based on the evaluation of atmospheric carbon potential sequestration into a productive rainfed maize crop and its relationship with the agricultural management practices. The final conclusions are presented in Section IV.

II. Material and Methods

Figure 2 shows the block diagram for the sensor-based architecture used for atmospheric carbon sequestration potential evaluation from crops. In the block diagram, one may observe the use of the Normalized Difference Vegetation Index (NDVI) and the Modified Chlorophyll Absorption in Reflective Index (MCARI), both calculated based on data acquired with a multispectral camera, as well as taking into account three other sensors for solar light intensity, soil water content, and air temperature measurements.

The NDVI was proposed in 1974 [7] and was validated five years later [8]. In fact, in 1979, the linear combinations of the bands of the Red wavelength (called RED) (668 nm ± 10 nm) and the Near Infra-Red wavelength (called NIR) (840 nm ± 40 nm) light bands became a monitor of biomass density. NDVI values from -1.0 to 1.0 can be found in literature. However, since soil has an NDVI value close to zero and for plant evaluation the values can be in the range from 0.1 to 1.0, the interval of [0.0-1.0] has come to be used in agricultural applications. The higher the value, the greater the plant density. Despite some limitations, it has a good linear correlation with crop growth [9]. Equation (1) shows the NDVI calculation formula, i.e., to allow in this work information regarding the biomass amount evaluation in the regions related to plant growth only.

On the other hand, the MCARI was published in the year 2000 [10], and it is recognized as an evolution of the Chlorophyll Absorption Ratio Index (CARI), whose development occurred in 1994 [11]. The CARI has been primarily used to estimate not only chlorophyll content in leaves but also frost content damage and the monitoring of the yield and physiological response of crops. Such a vegetation index improvement brought not only a better index focus but also a much stronger relationship with plant leaves' chlorophyll content. For the MCARI calculation, (2) is used considering the RED, Green wavelength (called GREEN) (560 nm ± 20 nm), and NIR light bands, i.e., in this work to estimate the amount of chlorophyll crop's leaves.

For solar light intensity measurements, a luxmeter based on a silicon photodiode with a spectral filter has been used, which can allow measurements up to 4 × 105 Lux and an accuracy of ±5%.

For soil moisture measurements, a capacitive sensor has been used, which can allow measures from 0.0 to 75.0 cm^3/cm^3 and accuracy of ±4%. Characteristics in relation to less invasive measurements have been considered in relation to such a selection. Soil moisture analyses have been carried out from horizon A (root zone) at specific sites on the sampling grid.

For air temperature measurements, the use of a platinum resistance sensor (PT100) calibrated for operation in the range of 0.0 to 80.0°C has been considered, which achieves an accuracy of up to ±0.4 °C, with a resolution of 0.1 °C. The electronics have been configured to have all the calculated indexes and the sensors' measurements provided to a computer model.

$$NDVI = \left(\frac{NIR-RED}{NIR+RED}\right) \quad (1)$$

$$MCARI = \left((NIR - RED) - 0.2(NIR - GREEN)\right)\left(\frac{NIR}{RED}\right) \quad (2)$$

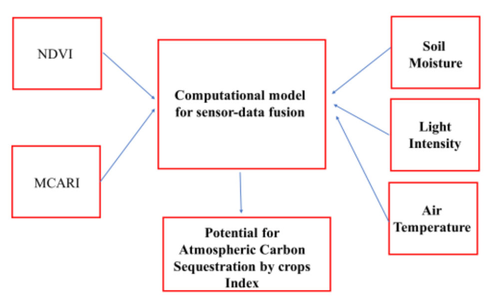

Figure 2. The sensor-based arrangement for the potential of atmospheric carbon sequestration by crops.

In fact, to have the vegetation indexes estimation, eight flight missions were conducted, i.e., based on the use of a

Courtesy of IARIA Board and IARIA Press. Original source: ThinkMind Digital Library https://www.thinkmind.org

Copyright (c) IARIA, 2025. ISBN: 978-1-68558-273-9

multirotor Unmanned Aircraft System (UAS), DJI Matrice 100 (Figure 3).

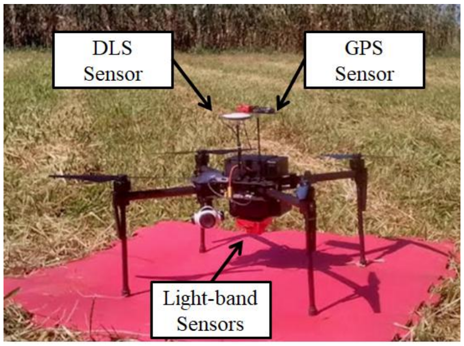

Figure 3. The UAS and hardware setup for the RGB, RED, GREEN, and NIR images acquisition.

For imaging, each flight has been considered to attend to each phenomenological state of the maize culture [12]. Then, in such a context, a MicaSense RedEdge-M multispectral camera has been considered and embedded onboard. The specifications of the multispectral sensors from the Micasense camera are detailed in Table I [13].

TABLE I. SPECIFICATIONS FOR THE MICASENSE CAMERA

Parameters	Specifications
Weigth	170 g (Including DLS)
Dimensions	9.4 cm × 6.3 cm × 4.6 cm (3.7" × 2.5" × 1.8")
External Power	4.2V−15.8V, 4W nominal, 8W peak
Spectral Bands	Narrowband: Blue, Green, Red, Near-IR
Capture Rate	1 capture per second (per band), 12−bit RAW
Ground Sample Distance (GSD)	5.95 cm/pixel (per band)
Wavelength	Blue (475 nm center ± 20 nm) Green (560 nm ± 20 nm) Red (668 nm center ± 10 nm) Near-IR (840 nm ± 40 nm)

In addition, for the light bands data acquisition protocol, the use of the Ground Control Points (GCP), a high-precision GPS in conjunction with a Real-Time Kinematic (RTK) receiver (i.e., allowing accuracy of ± 1 cm, and a Downwelling Light Sensor (DLS) to allow images' contrast correction due to possible superimposition of clouds in the sky has been considered. Furthermore, in accordance with the UAS settings and the onboard light-band sensors, for all the flights, the morning periods have been considered to be a time from 11 A.M. to 12 A.M.

For validation of the method, an experimental agricultural area has been used, i.e., following the study standards of Embrapa Instrumentation. The crop area is located 860 m from the geographic coordinates 21°57'3.9" S and 47°51'10.9" W at the National Reference Laboratory for Precision Agriculture (LANAPRE) in São Carlos, SP, Brazil.

Such an experimental crop area has been cultivated with maize (Zea mays L.), having 4,000 m² and a sampling grid equal to 10 m × 10 m. Figure 4 shows such an arrangement for specific management with the UAS navigation's flight route, i.e., divided into 40 blocks (from B1 to B40). The crop area has been divided into four plots of 1,000 m² (20 m × 50 m) aiming to manage Nitrogen (N) with surface and broadcast fertilization, associated with soil fertilization for the process of corn seeding.

Soil fertilization by N has been considered with scaled applications equal to 0, 18, 36, and 72 kg/ha, representing 0%, 50%, 100%, and 200%, respectively, in relation to the agronomic recommended dose [14]. All the other nutrients have been applied in recommended doses.

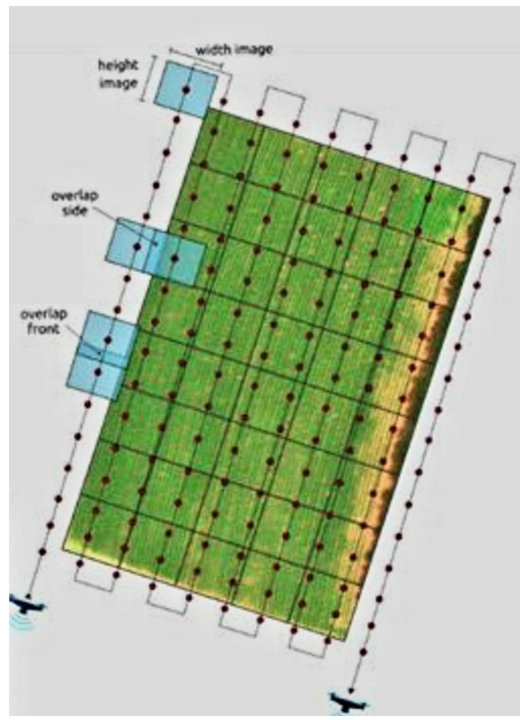

Figure 4. Experimental arrangement for sensors-based potential evaluation of atmospheric carbon sequestration with `specific site management, including the UAS navigation`s flight route.

Besides, to perform the analysis regarding atmospheric carbon sequestration's potential in the crop having maize plants, an extraction of information from each site-specific block has also been considered. Therefore, sensor data have been collected from each block, referred to as Region Of Interest (ROI), not only from the multispectral light bands but also from the sensors related to solar light intensity, soil moisture in the A-horizon, and air temperature.

Furthermore, to improve Signal to Noise Ratio (SNR), all the collected images have been filtered with a Gaussian filter using (3), and each ROI has been rotated, i.e., taking into consideration the angle calculation by (4) as follows.

$$G_\sigma(x,y) = \frac{1}{2\pi\sigma^2} e^{-\frac{x^2+y^2}{2\sigma^2}} \qquad (3)$$

Courtesy of IARIA Board and IARIA Press. Original source: ThinkMind Digital Library https://www.thinkmind.org

Copyright (c) IARIA, 2025. ISBN: 978-1-68558-273-9

$$Rotation = \begin{bmatrix} 1 & 0 & t_x \\ 0 & 1 & t_y \\ 0 & 0 & 1 \end{bmatrix} \begin{bmatrix} \cos\theta & -\sin\theta & 0 \\ \sin\theta & \cos\theta & 0 \\ 0 & 0 & 1 \end{bmatrix} \begin{bmatrix} 1 & 0 & -t_x \\ 0 & 1 & -t_y \\ 0 & 0 & 1 \end{bmatrix} \quad (4)$$

where the Gaussian function G_σ (x,y) is controlled by the variance σ^2, since the mean value is equal to zero, and the parameters $-t_x$, and $-t_y$ correspond to the translation of the ROI to the origin, whereas t_x, and t_y can allow shifting it back to its original position.

For data analysis, a Potential Atmospheric Carbon Sequestration Index (PACSI) has been defined, which allows assessing such potential by agricultural crops, i.e., considering (5) for each specific site from the experimental agricultural field, as well as the integration of the measurements and calculated variables.

$$PACSI \triangleq g\begin{pmatrix} Light\ Intensity, Air\ Temperature, \\ Soil\ Moisture, NDVI, MCARI \end{pmatrix} \quad (5)$$

To perform this operation, the fusion of variables is considered based on the use of the figure of merit's concept [15]. This fusion technique considers the set of normalized variables in the interval [0.0–1.0] and the respective plots of their values on a circle with unit radius, equally equidistant from each other (Fig. 5). From the marking of the resulting points on the equidistant radii, they are treated as vertices, and their connections represent edges (Eai) and (Ebi) of triangles, which, when united, generate a figure of merit whose area represents the result of the fusion or index resulting from the set of measurements or metrics used.

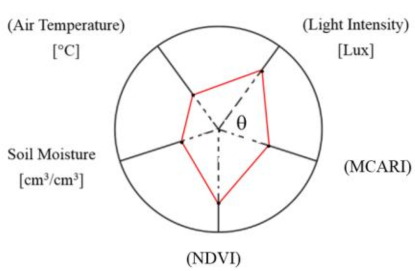

Figure 5. Sensor data fusion based on plotting normalized variables and equally equidistant from each other (θ=72°) on a circle with unit radius.

In this work, the referred index results from the sum of five areas of triangles formed within the circle with unit radius. Once the angles and edge measurements of each triangle are known, the total area can be calculated, as expressed in (6) as follows.

$$PACSI = \sum_{I=1}^{5} \frac{Ea_i Eb_i \sin\theta_i}{2} \quad (6)$$

Additionally, to complete the method's validation, after the determination of the PACSIs values, one for each specific site, the relationship with the nitrogen management was evaluated.

III. RESULTS AND DISCUSSIONS

For multispectral image acquisition, it was necessary to perform radiometric calibration to convert the metadata of the digital image to a physical scale. On the other hand, the geometry of the aerial image was established by the size of the sensor, the focal length, and the height of the UAS flights, which together determine its Ground Sample Distance (GSD) (Table II). The GSD provides the corresponding measure for the pixels of the surface of the experimental area or the area covered by the image. The percentages established for both the lateral and frontal overlapping of the aerial images were equal to 80% respectively.

The total number of registered images was equal to 300 for each spectral band, i.e., leading to a total amount of 9600 images, i.e., leading to a required storage capacity equal to 29.52 GB (gigabytes), because the surface width and height were equal to 27 m × 20 m, respectively, and the distances between each front and side capture were 4 m and 5 m, respectively.

TABLE II. PARAMETERS USED FOR DATA ACQUISITION

Description	Values	Units
Flying altitude	138	m
Mission flying time	12	min
Max. speed of flying	11	m/s
Front and side overlap	80	%
Ground sample distance	5.95	cm/pixel

Figure 6 shows examples of results obtained from the eighth flight, i.e., considering the rotation of the images and Regions Of Interest (ROI) for analysis of block 25, in terms of the RGB, NIR, RED, and GREEN light-bands.

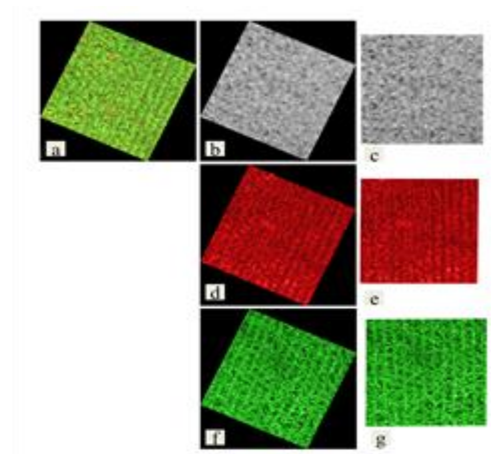

Figure 6. Sample of analysis for the block 25: from the eight flight - (a) RGB, (b) NIR, and (c) ROI NIR; (d) RED and (e)ROI RED; (f) GREEN, and (g) ROI GREEN.

Copyright (c) IARIA, 2025. ISBN: 978-1-68558-273-9

Data analyses for collected data were carried out for the eight flights, that is, considering not only the reflectance measurements and the calculations based on the use of (1) and (2), but also the additional sensors and their measurements for each site-specific area in the culture area. An example of the obtained results can be observed in Table III for all the blocks from the experimental field.

Besides, based on such a calculation of the vegetation indexes and the sensor-based data measurements, as well as using the (6), it was possible to figure out the PACSI values (in units of area) for each ROI presented in the experimental maize agricultural field (Table IV). In fact, before calculating the area of the figure of merit, all the values were normalized to be included in the circle having the unit radius, i.e., to make it possible to infer the potential of each block to sequester the atmospheric carbon by maize crop.

TABLE III. BLOCKS RESULTS FOR FLIGHT EIGHT

Specific Site (Block #)	X - UTM [m]	Y - UTM [m]	MCARI	NDVI	Light Intensity [Lux]	Air Temperature [°C]	Soil Moisture [cm³/cm³]
1	205,320.60	7,569,399.92	0.0295	0.6627	84,500	31.3	0.61
2	205,324.77	7,569,409.01	0.0283	0.6884	84,432	31.2	0.60
3	205,311.51	7,569,404.09	0.0309	0.5991	84,495	31.5	0.60
4	205,315.68	7,569,413.18	0.0289	0.6583	84,502	31.4	0.62
5	205,302.42	7,569,408.26	0.0295	0.6338	84,505	31.6	0.61
6	205,306.59	7,569,417.35	0.0291	0.6360	84,504	31.4	0.62
7	205,293.33	7,569,412.43	0.0295	0.6760	84,506	31.3	0.40
8	205,297.50	7,569,421.52	0.0292	0.6307	84,504	31.7	0.42
9	205,284.24	7,569,416.60	0.0326	0.7398	84,508	31.8	0.35
10	205,288.41	7,569,425.69	0.0292	0.6889	84,506	32.0	0.33
11	205,292.58	7,569,434.78	0.0261	0.7166	84,508	32.1	0.40
12	205,296.75	7,569,443.87	0.0256	0.7459	84,507	31.9	0.34
13	205,301.67	7,569,430.61	0.0270	0.7135	84,508	32.0	0.44
14	205,305.84	7,569,439.70	0.0260	0.7508	84,505	31.7	0.43
15	205,310.76	7,569,426.44	0.0262	0.7340	84,504	31.8	0.64
16	205,314.93	7,569,435.53	0.0268	0.7349	84,506	31.5	0.63
17	205,319.85	7,569,422.27	0.0267	0.7450	84,500	31.9	0.62
18	205,324.02	7,569,431.36	0.0253	0.7756	84,501	31.7	0.63
19	205,328.94	7,569,418.10	0.0254	0.7704	84,504	32.0	0.63
20	205,333.11	7,569,427.19	0.0253	0.7803	84,506	31.8	0.62
21	205,337.28	7,569,436.28	0.0223	0.8155	84,508	32.0	0.61
22	205,341.45	7,569,445.37	0.0220	0.8205	84,504	32.1	0.62
23	205,328.19	7,569,440.45	0.0228	0.8067	84,507	31.9	0.62
24	205,332.36	7,569,449.54	0.0223	0.8161	84,502	32.0	0.61
25	205,319.10	7,569,444.62	0.0242	0.7875	84,506	31.4	0.63
26	205,323.27	7,569,453.71	0.0224	0.8093	84,504	31.3	0.62
27	205,310.01	7,569,448.79	0.0238	0.7894	84,501	31.7	0.44
28	205,314.18	7,569,457.88	0.0224	0.8068	84,508	31.8	0.45
29	205,300.92	7,569,452.96	0.0248	0.7489	84,504	32.1	0.34
30	205,305.09	7,569,462.05	0.0257	0.7443	84,509	32.2	0.33
31	205,309.26	7,569,471.14	0.0235	0.7491	84,497	31.9	0.30
32	205,313.43	7,569,480.22	0.0244	0.7628	84,500	31.8	0.35
33	205,318.35	7,569,466.97	0.0219	0.8101	84,506	31.8	0.45
34	205,322.52	7,569,476.05	0.0231	0.7959	84,504	31.9	0.46
35	205,327.44	7,569,462.79	0.0213	0.8189	84,506	31.6	0.60
36	205,331.61	7,569,471.88	0.0229	0.7937	84,508	31.8	0.61
37	205,336.53	7,569,458.62	0.0209	0.8293	84,500	31.7	0.60
38	205,340.70	7,569,467.71	0.0214	0.8224	84,510	31.4	0.62
39	205,345.62	7,569,454.45	0.0211	0.8290	84,513	31.6	0.62
40	205,349.79	7,569,463.54	0.0220	0.8310	84,614	31.9	0.61

Figure 7 shows the relationship observed between the applied N dose and the PACSI calculated values for all the blocks from the experimental agricultural maize crop field.

For the example of results presented here with data from the eighth flight, the values found for PACSI were between 0.151 and 0.655, both values in units of area, with higher values indicating greater potential for sequestering carbon from the atmosphere by the corn crop.

TABLE IV. NORMALIZED RESULTS AND THE PACSI VALUE

Specific Site (Block #)	Normalized value for MCARI	Normalized value for NDVI	Normalized value for Light Intensity	Normalized value for Air Temperature	Normalized value for Soil Moisture	PACSI
1	0.735	0.274	0.895	0.273	0.600	0.294
2	0.633	0.385	0.000	0.182	0.733	0.191
3	0.857	0.000	0.000	0.182	0.733	0.173
4	0.679	0.255	0.000	0.182	0.733	0.183
5	0.732	0.158	0.000	0.182	0.733	0.178
6	0.701	0.159	0.000	0.182	0.733	0.172
7	0.730	0.331	0.000	0.182	0.733	0.207
8	0.710	0.136	0.947	0.182	0.300	0.151
9	1.000	0.606	0.882	0.091	0.067	0.294
10	0.706	0.387	0.974	0.091	0.000	0.168
11	0.443	0.507	0.947	0.000	0.300	0.190
12	0.403	0.633	0.987	0.182	0.033	0.245
13	0.518	0.493	0.934	0.091	0.367	0.233
14	0.435	0.654	0.961	0.182	0.333	0.293
15	0.452	0.581	0.895	0.000	0.567	0.236
16	0.500	0.586	0.000	0.182	0.600	0.159
17	0.490	0.629	0.829	0.091	0.600	0.285
18	0.373	0.761	0.829	0.091	0.533	0,281
19	0.386	0.739	0.961	0.000	0.567	0.275
20	0.369	0.781	0.947	0.364	0.933	0.467
21	0.120	0.933	0.974	0.273	0.233	0.313
22	0.090	0.955	0.947	0.636	0.300	0.411
23	0.160	0.895	1.000	0.727	0.067	0.414
24	0.120	0.935	0.974	0.909	0.000	0.433
25	0.280	0.812	0.974	0.364	1.000	0.458
26	0.125	0.906	0.947	0.273	0.967	0.367
27	0.246	0.820	0.908	0.636	0.367	0.420
28	0.122	0.895	1.000	0.727	0.400	0.470
29	0.332	0.646	0.947	1.000	0.233	0.473
30	0.407	0.626	0.934	0.909	0.300	0.473
31	0.220	0.647	0.961	0.636	0.267	0.364
32	0.298	0.706	0.947	0.727	0.300	0.426
33	0.081	0.910	0.974	0.455	0.400	0.367
34	0.187	0.849	0.895	0.818	0.433	0.473
35	0.030	0.948	0.908	0.636	0.900	0.469
36	0.166	0.839	0.947	0.909	0.933	0.635
37	0.000	0.992	0.974	0.727	0.900	0.529
38	0.042	0.963	0.934	0.909	0.967	0.615
39	0.016	0.991	0.947	1.000	0.967	0.655
40	0.094	1.000	0.987	0.818	0.933	0.622

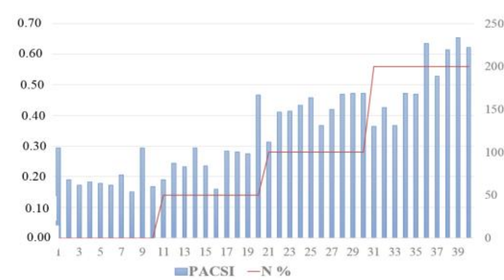

Figure 7. Histogram of the calculated PACSI values for the specific sites of the experimental maize crop field, considering the flight eighth and the N doses applied (in percentages).

Courtesy of IARIA Board and IARIA Press. Original source: ThinkMind Digital Library https://www.thinkmind.org

However, since chlorophyll content is related to photosynthesis and nitrogen fertilization, the application of N at different doses was also considered for validation in the field experiment. The existing relationship can be explained by considering that chlorophyll is dependent on nitrogen and is involved in photosynthesis, which in turn is also related to the potential for carbon sequestration from the atmosphere. Nitrogen is a nutrient that is present in the chloroplasts of leaves, where it participates in the synthesis of chlorophyll. Without nitrogen, there is no chlorophyll, which makes photosynthesis unfeasible and prevents plant development. It is important to note that in the example results, although there is a region of blocks where no additional nitrogen fertilization occurred (0%), there are indications of PACSI values, blocks from 1 to 10. This occurrence was observed due to the preliminary fertilization that was carried out in the soil for planting corn seeds, that is, the fertilization of the entire crop area that occurred at the beginning of the agricultural process. For the other blocks, that is, from 11 to 40, the impact of the additional percentage of N applied and its relationship with the increasing PACSI values was imperative. Evidently, the efficiency of the results depends on the values of light intensity, air temperature, and soil moisture.

Furthermore, one may observe that such a new PACSI index has the potential to also be used to indicate the need for nitrogen fertilization in the observed crop, thus helping the rural producer to save inputs and maximize contributions to the sequestration of atmospheric CO_2, which helps air quality and minimizes the effects of climate change.

The total cost to figure out this development of the sensor-based platform's prototype for the potential evaluation of atmospheric carbon sequestration by agricultural crops was about USD 75,000. Nevertheless, the developed solution based on such a sensor platform can be useful not only for large crop areas but also for small farms. In fact, alternatives to decrease costs in relation to its application can be reached by different pathways, i.e., using it as a service to be offered by others or even taking into consideration its cooperative use by a group of smallholder farmers.

IV. CONCLUSION AND FUTURE WORK

This work presented a new sensor-based index for evaluation of agricultural crop potential for carbon sequestration (PACSI). It is based on information related to the biomass amount per area, chlorophyll absorption by the plants, solar light intensity, air temperature, and the agricultural soil moisture in the root zone. In fact, it has been proved to be useful not only to help in managing impacts due to climate change but also to be used as an indicator for needs in nitrogen fertilization by the farmers, i.e., allowing not only loss minimization but also gain in sustainability. Future research works will consider the development of an integrated and customized agricultural smart sensor platform coupled to a Convolutional Neural Network (CNN) for real-time evaluation of the potential for atmospheric carbon sequestration by crops.

ACKNOWLEDGMENT

This research was partially supported by both the São Paulo Research Foundation, Brazil (FAPESP, Process No. 17/19350-2), and the Brazilian Corporation for Agricultural Research (Embrapa).

REFERENCES

[1] S. Dawid *et al.*, “Towards carbon neutrality: enhancing CO_2 sequestration by plants to reduce carbon footprint,” *Science of The Total Environment*, vol. 966, pp. 178763-178784, 2025.

[2] J. P. Dekker and R. Van Grondelle, “Primary charge separation in photosystem II,” *Photosynthesis Research*, vol. 63, pp. 195–208, 2000.

[3] N. Nelson and C. F. Yocum, “Structure and function of photosystems I and II,” *Annual Review of Plant Biology*, vol. 57, pp. 521–565, 2006.

[4] K. Ferreira *et al.*, “Architecture of the photosynthetic oxygen-evolving center,” *Science*, vol. 303, pp. 1831–1838, 2004.

[5] H. Ago *et al.*, “Novel features of eukaryotic photosystem II revealed by its crystal structure analysis from a red alga,” *Journal of Biological Chemistry*, vol. 291, pp. 5676–5687, 2016.

[6] R. Tanaka and A. Tanaka, “Chlorophyll cycle regulates the construction and destruction of the light-harvesting complexes,” *Biochimica et Biophysica Acta (BBA) – Bioenergetics*, vol. 1807, no. 8, pp. 968-976, 2011.

[7] J. W. Rouse *et al.*, “Monitoring vegetation systems in the great plains with ERTS,” in *Proceedings of the Third Earth Resources Technology Satellite-1 Symposium*, National Aeronautics and Space Administration (NASA), SP-351, Washington DC, USA, pp. 309-317, 1974.

[8] C. J. Tucker, “Red and photographic infrared linear combinations for monitoring vegetation,” *Remote Sensing of Environment*, vol. 8, pp. 127-150, 1979.

[9] P. E. Cruvinel and W. N. C. Veramendi, “Using light-band sensors for stress evaluation in rainfed maize agricultural crop,” in *IARIA, Proceedings of the Ninth International Conference on Advances in Sensors, Actuators, Metering and Sensing (ALLSENSORS 2024)*, pp. 1-7, 2024.

[10] C. S. T. Daughtry *et al.*, “Estimating corn leaf chlorophyll concentration from leaf and canopy reflectance,” *Remote sensing of Environment*, vol. 74, pp. 229–239, 2000.

[11] M. S. Kim *et al.*, “The use of high spectral resolution bands for estimating absorbed photosynthetically active radiation (A par),” in *CNES, Proceedings of 6th International Symposium on Physical Measurements and Signatures in Remote Sensing*, National Aeronautics and Space Administration (NASA), Report Number: GSFC-E-DAA-TN72921, February, pp. 299-306, 1994.

[12] M. W. L. Carvalho *et al.*, “Productive performance of maize crop irrigated with and without water deficit in different plant arrangements,” *Brazilian Journal of Maize and Sorghum*, vol. 19, pp. 1196-11208, 2020.

[13] MicaSense RedEdge-M™, Multispectral Camera, *User Manual*, vol. 1, pp. 1-47, 2017.

[14] A. P. Duarte, H. Cantarella, and J. A. Quaggio, "3.5. Maize (Zea mays)," in *Fertilization and liming recommendations for the state of São Paulo - Bulletin 100* (Organizers: H. Cantarella, J.A. Quaggio, Jr. D. Mattos R. M. Boaretto, B. van Raij), 3rd edition, Instituto Agronomic de Campinas, vol. 1, pp. 199-200, 2022.

[15] P. E. Cruvinel *et al.*, “Evaluation of models for establishing a risk figure for the occurrence of Black Sigatoka in banana plantations,” *Embrapa - Document Series*, ISSN: 1518-7179, n. 55, pp. 1-28, 2011.

Courtesy of IARIA Board and IARIA Press. Original source: ThinkMind Digital Library https://www.thinkmind.org

Development of Magnetic Microwires with High Magneto-Impedance Effect

Alvaro Gonzalez, Paula Corte-Leon, Valentina Zhukova
Department of Polymers and Advance Materials, Univ. Basque Country, UPV/EHU, 20018 San Sebastian, Spain
e-mail: alvaro.gonzalezv@ehu.eus; paula.corte@ehu.eus; valentina.zhukova@ehu.es,

Jesus Olivera
Instituto de Física, Facultad de Ciencias, Universidad Autónoma de Santo Domingo, Dominican Republic
e-mail: jolivera33@uasd.edu.do

Juan Maria Blanco
Dept. Appl. Phys. I, EIG, Univ. Basque Country, UPV/EHU, 20018, San Sebastian, Spain
e-mail: juanmaria.blanco@ehu.eus

Arcady Zhukov
Dept Polymers and Advance Materials Physics, Univ. Basque Country, UPV/EHU, 20018 San Sebastian and Ikerbasque, Bilbao Spain
e-mail: arkadi.joukov@ehu.es

***Abstract*— Giant Magneto-Impedance (GMI) effect is ideal for developing high-performance magnetic sensors due to its high sensitivity to magnetic fields and the ease of manufacturing magnetic sensors. We provide our attempts to improve the GMI effect and magnetic softness of Co-rich glass-coated magnetic microwires. We studied the GMI effect and magnetic properties of Co-rich glass-coated magnetic microwires with two different diameters. Substantially different frequency dependence of GMI effect is observed in studied microwires. A high GMI ratio of about 625% is observed in thinner Co-rich microwire at about 300 MHz.**

Keywords- magnetic microwires; magnetic softness; GMI effect; magnetic anisotropy.

I. INTRODUCTION

The main interest in amorphous wires is related to the GMI effect suitable for development of magnetic sensors [1]-[6]. Commonly, the GMI effect is attributed to high circumferential magnetic permeability, μ_ϕ, of amorphous wires and substantial μ_ϕ dependence on the applied magnetic field.

The most common way to represent the GMI effect is the GMI ratio, $\Delta Z/Z$, given as [1]-[6]:

$$\Delta Z/Z=[Z(H)-Z(H_{max})]/Z(H_{max})\cdot 100 \qquad (1)$$

where Z is the sample impedance, H is the applied magnetic field and H_{max} is the maximum applied Direct Current (DC) magnetic field (usually below a few kA/m).

Typically, $\Delta Z/Z$ –values of about 200-300% are reported in Co-rich magnetic wires with vanishing magnetostriction coefficients, λ_s [4]-[6]. In several publications, $\Delta Z/Z$ –values above 600% have been achieved in carefully processed Co-rich glass-coated microwires [4][7]. Such glass-coated microwires can be prepared using the so-called modified Taylor-Ulitovsky (also known as quenching-and-drawing method), actually known since the 60s and intensively studied since the 90s [7]-[9].

The performance of sensors and devices based on use of the GMI effect is substantially affected by the $\Delta Z/Z$ - value. Therefore, great attention was paid to studies of the magnetic wires with improved magnetic softness and optimization of the GMI effect by thermal treatment [4][7].

Consequently, in this paper we provide our latest attempt on optimization of the magnetic softness and GMI effect in Co-rich glass-coated magnetic microwires.

In Section 2, we present the description of the experimental methods and samples, while in Section 3, we describe the results on effect of annealing on hysteresis loops and GMI effect of Co-rich microwires. We conclude our work in Section 4.

II. EXPERIMENTAL DETAILS

We studied magnetic properties and GMI effect in amorphous $Co_{72}Fe_4B_{13}Si_{11}$ glass-coated microwires with metallic nucleus diameters, d, of about 40 μm and a total diameter, D, of about 45 μm (sample 1) and $d \approx 25.8$ μm $D \approx 29.2$ μm (sample2) manufactured by the aforementioned Taylor-Ulitovsky method. Briefly, the Taylor-Ulitovsky technique involves melting a metallic alloy inside a Duran-type glass tube using a high-frequency inductor, forming the glass capillary, drawing of such capillary filled with the molten metallic alloy surrounded by a softened glass, and winding of the solidified glass-coated microwires onto a rotating bobbin [8]-[10]. In fact, this fabrication technique is known since the 60s [11][12], however it was considerably modified during the last years [8]-[10]. The chemical composition was selected considering nearly-zero magnetostriction coefficient, λ_s ($\lambda_s \approx 10^{-7}$) of Co-rich Co-Fe based amorphous alloys [13][14].

Axial hysteresis loops were measured using the fluxmetric method, developed for studies of soft magnetic

Courtesy of IARIA Board and IARIA Press. Original source: ThinkMind Digital Library https://www.thinkmind.org

microwires with reduced diameters [15]. In this method, the electromotive force, ε, is induced in the pick-up coil with number of turns, N, due to a change in the magnetic flux, ϕ, when the magnetization reversal of a sample with magnetization M occurs [15]. Such ε is given as:

$$\varepsilon = -N\frac{d\phi}{dt} \quad (2)$$

The magnetic flux, ϕ, is produced by both the applied field, H, and by the sample magnetization, M, [15]:

$$\phi == \mu_0[A_c H + A_s M] \quad (3)$$

where A_c and A_s are the coil and sample cross-section areas. The use of compensation coil allows to remove the applied field contribution [15]. Finally, the magnetization, M, can be obtained by integrating the ε, as follows:

$$M = \frac{1}{N\mu_0 A_s}\int \varepsilon\, dt \quad (4)$$

The hysteresis loops represented as the normalized magnetization M/M_o versus applied magnetic field, H (being M_o -the magnetic moment of the samples at maximum amplitude H_o of magnetic field) allows better comparison of magnetic properties of studied microwires with different chemical compositions and diameters.

The GMI ratio, $\Delta Z/Z$, was defined using (1) from the $Z(H)$ dependence. Z-values were evaluated using a vector network analyzer from the reflection coefficient S_{11}, as described elsewhere [16].

The amorphous state studied sample has been confirmed by a broad halo in the X-ray spectra obtained using X-ray diffraction.

The magnetostriction coefficient, λ_s, of both studied samples was evaluated using the so-called Small Angle Magnetization Rotation (SAMR) method. In both samples, low and negative λ_s-values of about -0.9×10^{-6} are obtained.

We studied as-prepared microwires and microwires annealed in conventional furnace at 300 ºC.

III. EXPERIMENTAL RESULTS AND DISCUSSION

As can be seen from the hysteresis loop (see Figure 1), both as-prepared microwires present rather soft magnetic properties with coercivities, H_c, about 20 A/m and magnetic anisotropy fields, H_k, below 200 A/m.

This behavior is typical for amorphous microwire with low negative λ_s –values. The $\Delta Z/Z(H)$ dependencies of both studied samples measured at various frequencies, f, are provided in Figures 2 (a) and (b). Double-peak $\Delta Z/Z(H)$ dependencies, typical for magnetic wires with circumferential magnetic anisotropy [17], are observed at all measured frequencies in both samples (see Figure 2). Such features of the GMI effect correlate with the hysteresis loop, particularly with low H_c and H_k -values.

In both studied samples, a rather high GMI effect, i.e. high maximum $\Delta Z/Z$ ratio, $\Delta Z/Z_{max}$, (≈600 %) is observed (see

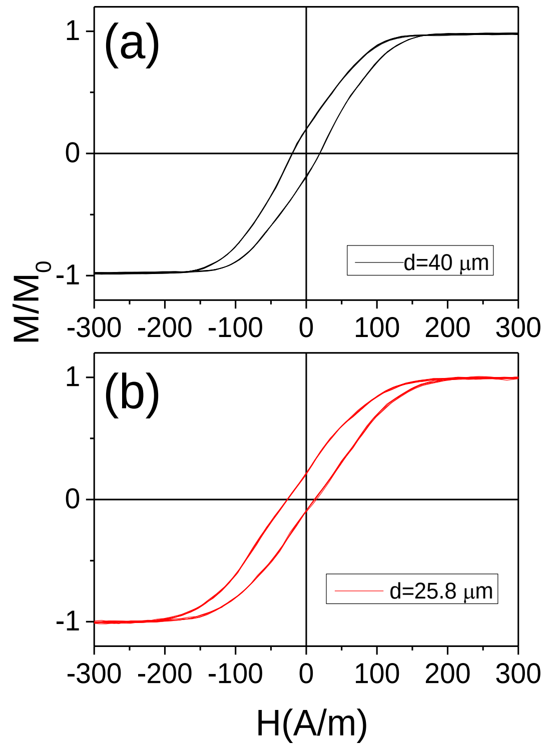

Figure 1. Hysteresis loops of the sample 1 (a) and 2 (b).

Figure 2). The achieved high $\Delta Z/Z_{max}$ –values are relevant for obtaining of high magnetic field sensitivity, η, given as [1] [3] [18]:

$$\eta = \frac{\partial\left(\frac{\Delta Z}{Z}\right)}{\partial H} \quad (5)$$

Obviously, the η-value given by (5) is one of the important parameters for the GMI materials performance. From the relationship between η and $\partial\left(\frac{\Delta Z}{Z}\right)$, given by (5), it follows that the higher $\Delta Z/Z_{max}$ –values, the higher the η-values. Therefore, a comparison of the $\Delta Z/Z_{max}$ –values and their frequency dependencies is meaningful for assessing the effectiveness of the GMI effect in studied samples.

As follows from Figure 2, $\Delta Z/Z_{max}$ –values are observed at each frequency, f. As previously already discussed, $\Delta Z/Z_{max}$ ratio in magnetic wires usually exhibits maximum value at some optimum frequency, f_o [3][16]. As observed from Figure 2, $\Delta Z/Z_{max}$ –values are affected by f, being higher at $100\leq f\leq400$ MHz (see Figure 2).

The $\Delta Z/Z_{max}$ (f) dependencies obtained from $\Delta Z/Z(H)$ dependencies measured in the frequency range up to 800 MHz are shown in Figure 3. As can be seen from Figure 3, slightly higher $\Delta Z/Z_{max}$– values are obtained for sample 1 at f < 100 MHz. However, at f ≥100 MHz higher $\Delta Z/Z_m$– values are observed for sample 2.

Courtesy of IARIA Board and IARIA Press. Original source: ThinkMind Digital Library https://www.thinkmind.org

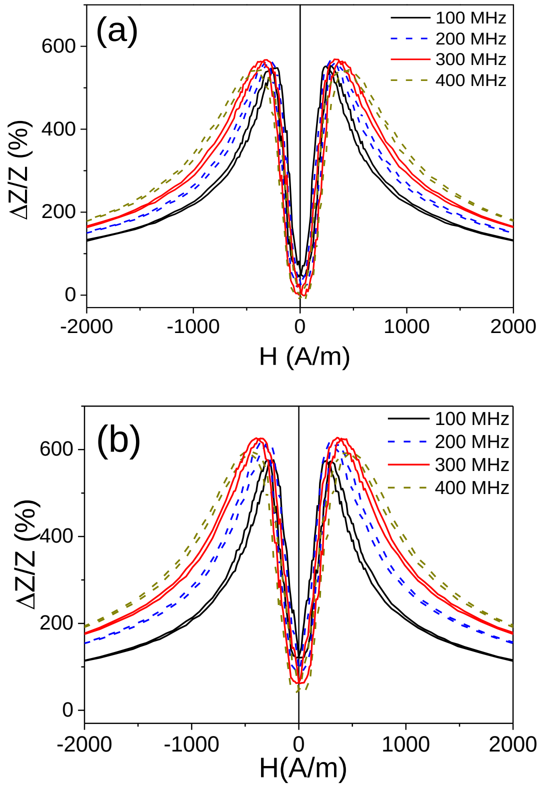

Figure 2. *ΔZ/Z(H)* dependencies measured at different frequencies in sample 1 (a) and 2 (b).

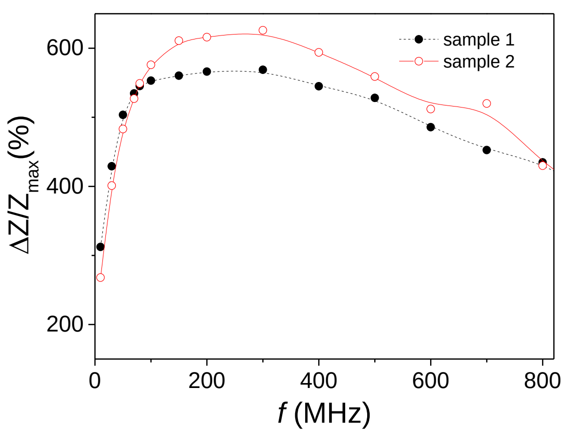

Figure 3. $\Delta Z/Z_m(f)$ dependencies evaluated from *ΔZ/Z(H)* dependencies for both studied samples.

The $\Delta Z/Z_{max}$ -value and the frequency, f_o, at which $\Delta Z/Z_{max}$ is observed are related to the wire diameter and to the magnetoelastic anisotropy [3][19]. Thus, a decrease in magnetic wire diameter is associated with an increase in the f_o –value [19]. The $\Delta Z/Z_{max}$ –values obtained for the sample 2 ($\Delta Z/Z_{max}$ ≈625%) observed at f_o ≈300 MHz are among the highest reported for as-prepared glass-coated microwires [4][[7]. Considering that appropriate annealing usually allows further $\Delta Z/Z_{max}$ –value improvement, future research on effect of annealing on GMI effect will be carried out.

IV. CONCLUSIONS AND FUTURE WORK

We studied magnetic properties and GMI effect in two $Co_{72}Fe_4B_{13}Si_{11}$ glass-coated amorphous microwires with different metallic nucleus diameters. The studied samples of the same chemical composition but different diameters exhibit different frequency dependences of the maximum GMI ratio. Quite high maximum GMI ratio (up to 625%) is observed in thinner Co-rich microwires at 300 MHz. Future studies of the appropriate annealing on $\Delta Z/Z_{max}$ –value might be helpful for further improvement of the GMI effect.

ACKNOWLEDGMENT

This work was supported by EU under “INFINITE” (HORIZON-CL5-2021-D5-01-06) and “Harmony” (HORIZON-CL4-2023-RESILIENCE-01) projects, by the Spanish MICIN, under PID2022-141373NB-I00 project, by the Government of the Basque Country under PUE_2021_1_0009, Elkartek (MOSINCO and ATLANTIS) projects and under the scheme of “Ayuda a Grupos Consolidados” (ref. IT1670-22). The authors thank the technical and human support provided by SGIker of UPV/EHU (Medidas Magneticas Gipuzkoa) and European funding (ERDF and ESF). J.O. thanks the Ministry of Higher Education, Science and Technology (MESCYT) of the Dominican Republic.

REFERENCES

[1] M. Knobel, M. Vazquez, and L. Kraus, “Giant magnetoimpedance“, Handbook Magn. Mater., vol. 15, pp. 497- 563, 2003.

[2] R. Beach and A. Berkowitz, “Giant magnetic field dependent impedance of amorphous FeCoSiB wire”, Appl. Phys. Lett. vol. 64, pp. 3652-3654, 1994.

[3] A. Zhukov et al., “Giant magnetoimpedance in rapidly quenched materials,” J. Alloy Compd., vol. 814, p. 152225, 2020.

[4] K. R. Pirota, L. Kraus, H. Chiriac, and M. Knobel, “Magnetic properties and GMI in a CoFeSiB glass-covered microwire”, J. Magn. Magn. Mater., vol. 21, pp. L243-L247, 2000.

[5] K. Mohri, T. Uchiyama, L.P. Shen, C. M. Cai, and L.V. Panina, “Amorphous wire and CMOS IC-based sensitive micro-magnetic sensors (MI sensor and SI sensor) for intelligent measurements and controls”, J. Magn. Magn. Mater. vol. 249, pp. 351-356, 2002.

[6] M. H. Phan and H. X. Peng, “Giant magnetoimpedance materials: Fundamentals and applications”, Progr. Mater. Sci. vol. 53 (2008) pp. 323-420.

[7] P. Corte-León et al., “Engineering of magnetic properties of Co-rich microwires by joule heating”, Intermetallics, vol. 105, pp. 92-98, 2019.

[8] H. Chiriac et al., “Ultrathin Nanocrystalline Magnetic Wires”, Crystals, vol. 7, p. 48, 2017.

[9] S. A. Baranov, V.S. Larin, and A.V. Torcunov, “Technology, Preparation and Properties of the CastGlass-Coated Magnetic Microwires” Crystals, vol. 7, p. 136, 2017.

Courtesy of IARIA Board and IARIA Press. Original source: ThinkMind Digital Library https://www.thinkmind.org

[10] A. Zhukov et al., “Advanced functional magnetic microwires for technological applications”, J. Phys. D: Appl. Phys., vol. 55, p. 253003, 2022.
[11] A. V. Ulitovsky, I. M. Maianski, and A. I. Avramenco, “Method of continuous casting of glass coated microwire“, USSR Patent, No. 128427, 1960, Bulletin No. 10, p. 14.
[12] L. Kraus, J. Schneider, and H. Wiesner, “Ferromagnetic resonance in amorphous alloys prepared by rapid quenching from the melt”, Czech. J. Phys. B, vol. 26, pp.601–602, 1976.
[13] Y. Konno and K. Mohri, “Magnetostriction measurements for amorphous wires”, IEEE Trans Magn., vol. 25, pp. 3623-3625, 1989.
[14] M. Churyukanova et al., “Magnetostriction investigation of soft magnetic microwires”, Phys. Stat. Sol. A, vol. 213(2), pp. 363–367, 2016.
[15] L. Gonzalez-Legarreta et al., “Optimization of magnetic properties and GMI effect of Thin Co-rich Microwires for GMI Microsensors”, Sensors, vol. 20, p. 1558, 2020.
[16] A. Zhukov et al., “Routes for Optimization of Giant Magnetoimpedance Effect in Magnetic Microwires“, IEEE Instrum. Meas. Mag., vol. 23(1), pp. 56-63, 2020.
[17] N. A. Usov, A. S. Antonov, and A. N. Lagar`kov, “Theory of giant magneto-impedance effect in amorphous wires with different types of magnetic anisotropy”, J. Magn. Magn. Mater., vol. 185, pp. 159-173, 1998.
[18] P. Corte -León, A. Gonzalez, V. Zhukova, M. Ipatov, J. M. Blanco, and A. Zhukov, “Optimization of giant magnetoimpedance effect in Co-rich glass-coated microwires by annealing”, J. Alloys Compound, vol. 999, p. 175023, 2024 doi: 10.1016/j.jallcom.2024.175023
[19] D. Ménard, M. Britel, P. Ciureanu, and A. Yelon, “Giant magnetoimpedance in a cylindrical magnetic conductor”, J. Appl. Phys., vol 84 (5), pp. 2805–2814, 1998.

Courtesy of IARIA Board and IARIA Press. Original source: ThinkMind Digital Library https://www.thinkmind.org

Free Space Microwave Stresses Sensing in Composites with Ferromagnetic Microwire Inclusions

Valentina Zhukova, Alvaro Gonzalez, Alfonso García-Gómez
Dept. Polym. Advanced Materials, Dept. Applied Physics and EHU Quantum Center, Univ. Basque Country, UPV/EHU, 20018 San Sebastian, Spain
e-mails: valentina.zhukova@ehu.es; alvaro.gonzalezv@ehu.eus; alfonso.garciag@ehu.eus

Johan Malm, Christer Johansson
RISE Research Institutes of Sweden, Digital Systems, Göteborg, Sweden
emails: johan.malm@ri.se; christer.johansson@ri.se

Rafael Garcia-Etxabe, Maitane Mendinueta
GAIKER Technology Centre, Basque Research and Technology Alliance (BRTA) and Department of Electricity and Electronics, University of Basque Country, UPV/EHU, 48940 Leioa, Spain
e-mail: etxabe@gaiker.es

Arcady Zhukov
Dept. Polym. Advanced Materials, Dept. Appl. Physics and EHU Quantum Center, Univ. Basque Country, UPV/EHU, 20018 San Sebastian and Ikerbasque, Bilbao, Spain
e-mail: arkadi.joukov@ehu.es

***Abstract*—In this work, we provide recent experimental results on free space microwave measurements of composites with ferromagnetic microwires inclusions. We observed that both hysteresis loops and the S_{12} parameter in the frequency range 2-4 GHz are affected by applied stress. Such stress sensitivity of studied composites is potentially suitable for contactless stress monitoring in civil engineering or in aircraft industry.**

Keywords-magnetic microwires; magnetic softness; carbon fiber composite; magnetoimpedance effect; applied stress.

I. INTRODUCTION

Amorphous soft magnetic wires, prepared by rapid melt quenching, are useful for numerous industrial applications, such as magnetic and magnetoelastic sensors [1]-[6]. Recently, great attention has been paid to the development of amorphous materials at micro-nano scale involving melt quenching with improved biocompatibility, corrosion and mechanical properties [7][8]. Glass-coated amorphous microwires prepared by the Taylor-Ulitovsky technique present a unique combination of physical properties: such magnetic microwires have extended diameters range (between 0.2 and 100 µm), covered with thin, insulating, biocompatible and flexible glass-coating and can present excellent mechanical and magnetic properties [7]-[10].

Recently, the stress and temperature dependence of hysteresis loops and Giant Magnetoimpedance (GMI) effect are proposed for the mechanical stresses monitoring in Fiber Reinforced Composites (FRC) with microwires inclusions and magnetoelastic sensors [11]- [14]. In particular, it was previously shown that the microwave response of a wire medium is affected by modifying the magnetic properties with external stimuli (magnetic field, stress, temperature). The aforementioned physical mechanism is based on a combination of the dispersion properties of the wire medium and the GMI effect [15]. The main advantage of this method is that it allows for contactless monitoring of external stimuli, like stress or temperature.

In this paper, we present our latest results on studies of magnetic properties of glass-coated Co-rich microwires and on wireless health monitoring of composites containing both carbon fibers and ferromagnetic glass-coated microwires.

This paper is organized as follows. In Section 2, the experimental methods are described. Section 3 deals with experimental results on free space microwave measurements of composites containing ferromagnetic glass-coated microwires. Finally, we conclude the paper in Section 4.

II. EXPERIMENTAL SYSTEM DETAILS

For the magnetic wire inclusions, we selected amorphous $Co_{64.6}Fe_5B_{16}Si_{11}Cr_{3.4}$ glass-coated microwires with metallic nucleus diameters, *d*, of about 38 µm and a total diameter, *D*, of about 45 µm manufactured by the aforementioned Taylor-Ulitovsky method. Recently, a high GMI effect with a GMI ratio above 700% has been reported in similar Co-rich microwires [16]. The morphology of studied microwires has been evaluated using Carl Zeiss -Axio Scope A1 microscope. As can be observed from Figure 1a, the studied microwire presents perfectly cylindrical geometry of the metallic nucleus and rather uniform glass-coating. The amorphous structure of the studied sample has been confirmed by a broad halo in the X-ray spectra obtained using X-ray diffraction (see Figure 1b). Typically, the crystallization of amorphous microwires was observed at Tann ≥ 500 °C [10].

Magnetic hysteresis loops of studied microwires have been measured using the fluxmetric method, previously described in detail elsewhere [17]. The hysteresis loops were represented as the dependence of normalized magnetization, M/M_0 (where M is the magnetic moment at a given magnetic field and M_0 is the magnetic moment of the sample at the maximum magnetic field amplitude almost at magnetic

Courtesy of IARIA Board and IARIA Press. Original source: ThinkMind Digital Library https://www.thinkmind.org

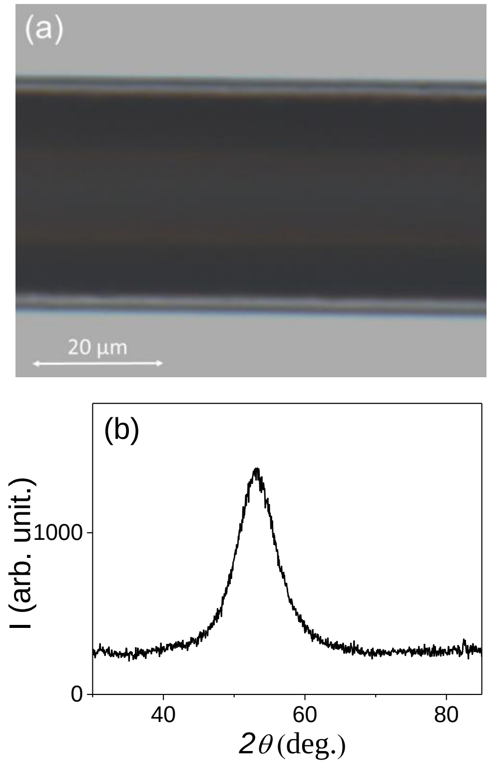

Figure 1. Image obtained using optical microscope (a) and XRD pattern (b) of studied sample.

saturation) versus the magnetic field, H. Such format of hysteresis loops allows better comparison of microwires with different chemical composition and diameters. The homogeneous axial magnetic field was produced by a long solenoid (about 1 cm in diameter and 12 cm in length). All the measurements were performed at low magnetic field frequencies (100 Hz).

The composites containing ferromagnetic glass-coated microwires embedded in polymeric matrix were manufactured at Gaiker facilities. The detailed description on fabrication of composites is provided elsewhere [18]. An epoxy system was used to manufacture the polymeric matrix: SICOMIN SR Infugreen 810 resin catalyzed with SICOMIN SD 8822.

The sample impedance, Z, in extended frequency range has been evaluated using the micro-strip sample holder from the reflection coefficient, S_{11}, obtained using Vector Network Analyzer (VNA), as previously described [19]. Such micro-strip holder with samples has been placed inside a long solenoid generating a homogeneous magnetic field, H. The experimental facility allows to measure the GMI effect up to GHz frequencies, f. The GMI ratio, $\Delta Z/Z$, is obtained from $Z(H)$ dependence as:

$$\Delta Z/Z = [Z(H) - Z(H_{max})]/Z(H_{max}), \qquad (1)$$

where H and H_{max} are given and maximum applied fields, respectively.

For wireless measurements, we used the free space measurement setup (see Figure 2) consisting of two broadband horn antennas ($1 \leq f \leq 17$ GHz) fixed to the anechoic chamber and a vector network analyzer, previously employed for the characterization of the composites with magnetic wire inclusions [11][15]. Such setup allows to characterize the composite of 20 x 20 cm^2. As recently

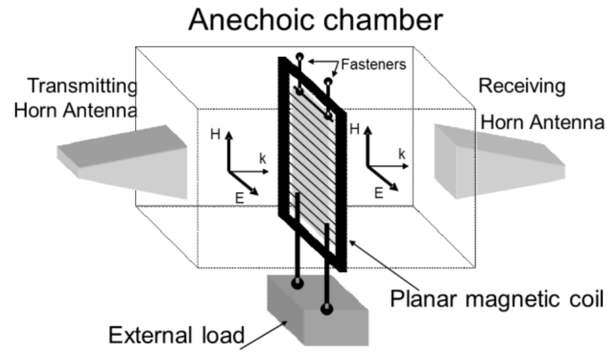

Figure 2. Sketch of the free-space setup.

described, applied magnetic modulation field during the microwave scattering measurements allows to separate the signal from magnetic microwires inclusions from the signal originated by the conductive matrix [20]. The magnetic field is produced by the planar magnetic coil. The mechanical load attached to the composite produced the tensile mechanical stress. We used an universal tension machine (SERVOSIS) allowing to apply tensile stress, augmenting the applied load by increments of 1 kN and simultaneously measuring S parameters [18]. As previously described [18], tensile stress is applied in a vertical way, both microwires and polarization direction of the antennas were oriented in that way.

III. EXPERIMENTAL RESULTS AND DISCUSSION

The hysteresis loop of studied microwires is provided in Figure 3. As observed from Figure 3, the studied microwire shows good magnetic softness: a coercivity, H_c, of about 20 A/m and a magnetic anisotropy field, H_k, of about 150 A/ m.

Figure 4 shows the results on GMI effect of the studied

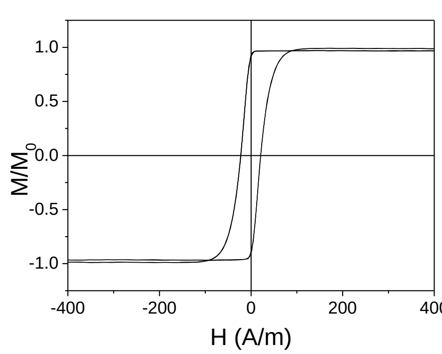

Figure 3. Hysteresis loop of studied sample

Courtesy of IARIA Board and IARIA Press. Original source: ThinkMind Digital Library https://www.thinkmind.org

Copyright (c) IARIA, 2025. ISBN: 978-1-68558-273-9

microwire. As evidenced from Figure 4, the studied microwire presents a high GMI effect with maximum $\Delta Z/Z$, $\Delta Z/Z_m$, of slightly above 200 % at frequencies of about 100-150 MHz. Such H_c, H_k, and $\Delta Z/Z_m$ -values are typical for Co-rich microwires with vanishing magnetostriction coefficients [7] [10] [17].

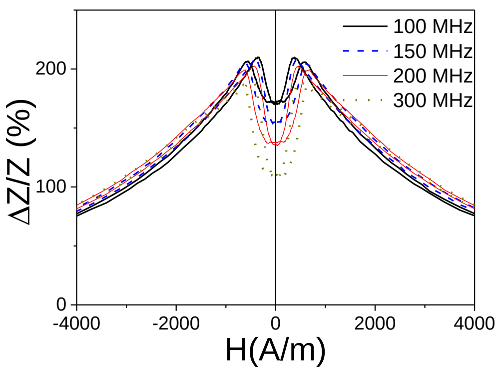

Figure 4. $\Delta Z/Z$ (H) dependencies of studied sample measured at different f.

As reported elsewhere [14] [21], magnetic properties and GMI effect of amorphous Co-rich microwires are substantially affected by applied stress and by heating. Therefore, we expect that utilizing magnetic microwires inclusions in carbon fiber composites can be suitable for stress and/or temperature monitoring.

As can be observed from Figure 5, the composites with these microwires in glass composites revealed that the S_{12} parameter is sensitive to applied force, F_a: there is a clear difference in the S_{12} parameter in the frequency range 2-4 GHz measured at F_a = 1 kN and F_a = 5 kN, due to the stress dependence of the impedance of the magnetic microwire.

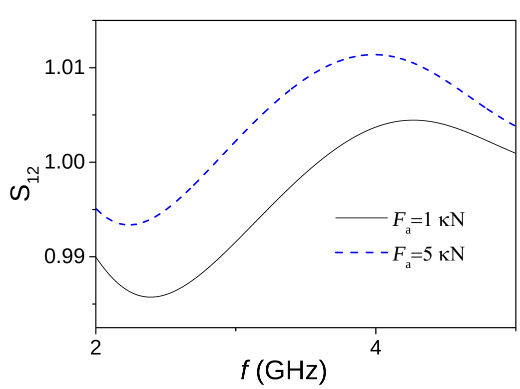

Figure 5. Effect of applied force on S_{12} (transmission) measured in the frequency range from 2 to 5 GHz.

The aforementioned experimental results provide the routes for development of tunable composites with magnetically soft amorphous glass-coated microwires inclusions sensitive to applied stresses.

It must be noted that, in the case of the composites with the carbon fibers and magnetically soft amorphous glass-coated microwires inclusions, the use of a low frequency modulating magnetic field is required to distinguish the microwave signals originated by ferromagnetic microwires inclusions from that generated by the carbon fibers [18]. The use of magnetic microwires inclusions in composite materials is potentially suitable for contactless stress monitoring in civil engineering or in aircraft industry.

IV. CONCLUSIONS AND FUTURE WORK

We have explored the feasibility of developing composites with glass-coated magnetic microwires inclusions using the free space microwave spectroscopy for stresses monitoring. For the preparation of such composites, we selected Co-rich microwires with good magnetic softness and high GMI effect. We experimentally observed that the S_{12} parameter is sensitive to applied force in the frequency range 2-4 GHz. The observed sensitivity of such composites with microwire inclusions is potentially suitable for contactless stress monitoring in civil engineering or in aircraft industry. Future studies of the temperature on S_{12} parameter might be helpful for potential applications. Developing a portable reader is one of the next steps towards real applications.

ACKNOWLEDGMENT

This work was supported by EU under "INFINITE" (HORIZON-CL5-2021-D5-01-06) and "Harmony" (HORIZON-CL4-2023-RESILIENCE-01) projects, by the Spanish MICIN under PID2022-141373NB-I00, by the Government of the Basque Country under Elkartek (ATLANTIS and MOSINCO) projects and under the scheme of "Ayuda a Grupos Consolidados" (ref. IT1670-22). The authors thank for the technical and human support provided by SGIker (Medidas Magnéticas Gipuzkoa) (UPV/EHU, ERDF, EU).

REFERENCES

[1] V. Zhukova et al., "Electronic Surveillance and Security Applications of Magnetic Microwires", Chemosensors, vol. 9, p.100, 2021.

[2] K. Mohri, T. Uchiyama, L. P. Shen, C. M. Cai, and L. V. Panina, "Amorphous wire and CMOS IC-based sensitive micro-magnetic sensors (MI sensor and SI sensor) for intelligent measurements and controls", J. Magn. Magn. Mater., vol. 249, pp. 351-356, 2001.

[3] T. Uchiyama, K. Mohri, and Sh. Nakayama, "Measurement of Spontaneous Oscillatory Magnetic Field of Guinea-Pig Smooth Muscle Preparation Using Pico-Tesla Resolution Amorphous Wire Magneto-Impedance Sensor", IEEE Trans. Magn., vol. 47, pp. 3070-3073, 2011.

[4] Y. Honkura, "Development of amorphous wire type MI sensors for automobile use", J. Magn. Magn. Mater., vol. 249, pp. 375-381, 2002.

[5] A. Zhukov et al., "Magnetoelastic sensor of level of the liquid based on magnetoelastic properties of Co-rich microwires", Sens. Actuat. A Phys., vol. 81, no. 1-3, pp.129-133, 2000.

Courtesy of IARIA Board and IARIA Press. Original source: ThinkMind Digital Library https://www.thinkmind.org

[6] L. Ding et al., “Development of a high sensitivity Giant Magneto-Impedance magnetometer: comparison with a commercial Flux-Gate”, IEEE Sensors, vol. 9, no.2, pp. 159-168, 2009.

[7] V. Zhukova et al., “Development of Magnetically Soft Amorphous Microwires for Technological Applications”, Chemosensors, vol. 10, p. 26, 2022

[8] D. Kozejova et.al., “Biomedical applications of glass-coated microwires”, J. Magn. Magn. Mater., vol. 470, pp. 2-5, 2019.

[9] T. Goto, M. Nagano, and N. Wehara, “Mechanical properties of amorphous $Fe_{80}P_{16}C_3B_1$ filament produced by glass-coated melt spinning”, Trans. JIM, vol. 18, pp. 759–764, 1977.

[10] A. Zhukov et al., “Advanced functional magnetic microwires for technological applications”, J. Phys. D: Appl. Phys., vol. 55, p. 253003, 2022.

[11] D. Makhnovskiy, A. Zhukov, V. Zhukova, and J. Gonzalez, “Tunable and self-sensing microwave composite materials incorporating ferromagnetic microwires”, Advances in Science and Technology, vol. 54, pp 201-210, 2008.

[12] F. Qin and H. X. Peng, “Ferromagnetic microwires enabled multifunctional composite materials”, Prog. Mater. Sci., vol. 58, no. 2, pp.183-259, 2013.

[13] A. Allue et al., “Smart composites with embedded magnetic microwire inclusions allowing non-contact stresses and temperature monitoring”, Compos. Part A Appl., vol. 120, pp. 12-20, 2019, DOI: 10.1016/j.compositesa.2019.02.014

[14] P. Corte -Leon et al., ”Effect of temperature on magnetic properties and magnetoimpedance effect in Fe -rich microwires”, J. Alloys Compound. vol. 946, p.169419, 2023, doi: https://doi.org/10.1016/j.jallcom.2023.169419

[15] L. Panina, M. Ipatov, V. Zhukova, J. Gonzalez, and A. Zhukov, “Tuneable composites containing magnetic microwires”, ch. 22, pp.431-460, doi: 10.5772/21423 in Book: Metal, ceramic and polymeric composites for various uses, Edited by John Cuppoletti, 2011, DOI: 10.5772/1428 ISBN: 978-953-307-353-8 (ISBN 978-953-307-1098-3) InTech - Open Access Publisher (www.intechweb.org), Janeza Trdine, 9, 51000 Rijeka, Croatia.

[16] P. Corte-León et al., “Optimization of giant magnetoimpedance effect in Co-rich glass-coated microwires by annealing”, J. Alloys Compound, vol. 999, p.175023, 2024.

[17] L. Gonzalez-Legarreta et al., “Optimization of magnetic properties and GMI effect of Thin Co-rich Microwires for GMI Microsensors”. Sensors, vol. 20, p.1558, 2020.

[18] R. Garcia-Etxabe et al., “Influence of Tensile Stress on Microwave Scattering Parameters of Continuous Ferromagnetic Microwire Embedded Into Glass Reinforced Composites”, IEEE Trans. Magn., doi: 10.1109/TMAG.2024.3488079

[19] A. Zhukov et al., “Routes for Optimization of Giant Magnetoimpedance Effect in Magnetic Microwires”, IEEE Instrumentation & Measurement Magazine, vol. 23, no. 1, pp. 56-63, 2020, doi: 10.1109/MIM.2020.8979525

[20] V. Zhukova et al., “Free Space Microwave Sensing of Carbon Fiber Composites With Ferromagnetic Microwire Inclusions”, IEEE Sens. Lett., vol. 8, No. 1, p. 2500104, 2024.

[21] P. Corte-Leon et al., “Stress dependence of the magnetic properties of glass-coated amorphous microwires” J. Alloys Compound, vol. 789, pp. 201-208, 2019, doi: 10.1016/j.jallcom.2019.03.044

Courtesy of IARIA Board and IARIA Press. Original source: ThinkMind Digital Library https://www.thinkmind.org

Copyright (c) IARIA, 2025. ISBN: 978-1-68558-273-9

Performance Improvement of Loop Closure Detection Using Semantic Segmentation in LiDAR SLAM

Shuya Muramatsu
Graduate School of Science and Engineering
Doshisha University
Kyotanabe, Kyoto, Japan
e-mail: ctwk0138@mail4.doshisha.ac.jp

Masafumi Hashimoto, Kazuhiko Takahashi
Faculty of Science and Engineering
Doshisha University
Kyotanabe, Kyoto, Japan
e-mail: {mhashimo, katakaha}@mail.doshisha.ac.jp

***Abstract*—This paper proposes a method to improve loop closure detection performance in Normal Distributions Transform (NDT) Graph Simultaneous Localization And Mapping (SLAM) using Light Detection And Ranging (LiDAR). Candidates of revisit places (loops) are detected from semantic information, such as buildings, fences, vegetation, trunks, poles, and traffic signs, based on semantic segmentation of LiDAR point cloud data. Loops are determined from loop candidates using semantic information-based point feature histograms in conjunction with conventional geometric information-based point feature histograms. Then, vehicle poses relative to loops are calculated based on the matching of point features and are applied to correct errors accumulated by NDT SLAM in the graph optimization framework. The projected-based semantic segmentation RangeNet++ is used to obtain semantic information about the surrounding environment. The experimental results obtained using the Semantic KITTI dataset demonstrate the performance of the proposed method.**

Keywords—LiDAR SLAM; NDT-Graph SLAM; loop closure detection; semantic segmentation.

I. Introduction

Recently, in the fields of Intelligent Transportation Systems (ITS) and mobile robotics, many studies on Autonomous Driving Systems (AVS) and Advanced Driver Assistant Systems (ADAS) have been reported [1][2]. Simultaneous Localization And Mapping (SLAM) and object recognition using onboard sensors, such as cameras and Light Detection And Ranging sensors (LiDARs), are important technologies for AVS and ADAS [3][4]. In this study, we focus on LiDAR SLAM.

Scan-matching SLAM using Normal Distributions Transform (NDT) and iterative closest point techniques is typically used in LiDAR SLAM [5]. However, the scan-matching SLAM causes accumulation errors as the travel distance of the vehicle increases. To reduce accumulation errors, Graph SLAM is employed in conjunction with scan-matching SLAM. In Graph SLAM, the detection of revisit places (referred to as loops) is a crucial issue, and many loop detection methods have been proposed [6].

A conventional loop detection method is based on geometric surface shape features of surrounding objects, such as poles and plains [7][8]. Loops are extracted based on the shape of the distribution of LiDAR point cloud data for objects, and loops are detected by checking the similarity of the surface shape features between two places. Another conventional geometric loop detection method is based on point features, such as Fast Point Feature Histograms (FPFH) [9] and normal-aligned radial features [10]. However, geometric surface and point features cannot distinguish objects with similar shapes, such as utility poles and trees; thus, false loop detection typically occurs.

In our previous works [11][12], to reduce false and miss detections of loops using geometric features, a two-stage loop detection method was proposed. First, loop candidates were detected based on the surface shape features. Next, loops were detected from loop candidates based on point features using FPFH and the three-Points Congruent Sets (3PCS) method. However, improvements are required to reduce miss and false loop detection.

Recently, in the ITS and mobile robotics domains, deep learning-based SLAM and object recognition methods have been actively discussed [13]. In SLAM, semantic segmentation improves the representation of surface and point features and the accuracy and robustness of loop detection. Many semantic segmentation-based loop detection methods have then been proposed [14]–[16]. However, applying semantic information to loop detection remains a challenge.

From this viewpoint, this paper improves the performance of our previous geometric loop detection method [12] by introducing semantic information from the RangeNet++ semantic segmentation method [17]. RangeNet++ is a projection-based semantic segmentation method with lower computation overhead and memory requirements than point- and voxel-based methods [18]. For this reason, RangeNet++ is used in this study.

The remainder of this paper is organized as follows. Section II describes LiDAR SLAM. Section III explains loop detection method. Section IV presents the experimental results obtained from the KITII dataset [19] to demonstrate the performance of the proposed method, followed by the conclusions in Section V.

II. Overview of LiDAR SLAM

LiDAR SLAM is based on NDT-Graph SLAM. First, the point cloud data captured from a vehicle-mounted LiDAR are mapped onto a three-dimensional (3D) grid map (voxel map) represented in the LiDAR coordinate system attached to the LiDAR. Then, a voxel grid filter is applied to downsize the LiDAR point cloud data. The block used for the voxel grid filter is a cube with a side length of 0.2 m.

In the world coordinate system, a voxel map with a voxel size of 1 m is used for NDT scan matching. For the i-th ($i = 1, 2, \dots n$) measurement in the LiDAR point cloud data, the position vector in the LiDAR coordinate system is denoted as $\boldsymbol{p}_{bi}$ and

Courtesy of IARIA Board and IARIA Press. Original source: ThinkMind Digital Library https://www.thinkmind.org

that in the world coordinate system is denoted as $\boldsymbol{p}_i$. The following relation is obtained:

$$\begin{pmatrix} \boldsymbol{p}_i \\ 1 \end{pmatrix} = \boldsymbol{T}(\boldsymbol{x}) \begin{pmatrix} \boldsymbol{p}_{bi} \\ 1 \end{pmatrix} \quad (1)$$

where $\boldsymbol{x} = (x, y, z, \phi, \theta, \psi)^T$ denotes the pose of the vehicle. (x, y, z) and (ϕ, θ, ψ) denote the 3D position and attitude angle (roll, pitch, and yaw angles) of the vehicle, respectively, in the world coordinate system. $\boldsymbol{T}(\boldsymbol{x})$ denotes the homogeneous transformation matrix.

The LiDAR point cloud data obtained at the current time step are referred to as the current point cloud data, and the point cloud data obtained up to the previous time step are referred to as the reference map. The vehicle pose $\boldsymbol{x}$ at the current time step is determined by matching the current point cloud data with the reference map. The vehicle pose is used for coordinate transform using (1). Then, the current point cloud can be mapped to the world coordinate system, and the reference map is updated.

The LiDAR obtains point cloud data by scanning laser beams. Thus, when a vehicle moves, the entire point cloud data in the LiDAR sampling period cannot be acquired at a single point in time. Therefore, if the entire point cloud data at the current time step are mapped onto the world coordinate system using vehicle-pose information at a single point in time, motion artifact (distortion) arises in the LiDAR point cloud data and degrades SLAM accuracy. The motion artifact is corrected using an unscented Kalman filter-based algorithm [20].

The point cloud data captured by the LiDAR is processed into semantic segmentation using RageNet++, and semantic information is obtained for each LiDAR measurement. In this study, 12 semantic classes are considered: cars, two-wheelers, other vehicles, people, roads, lawns, buildings, fences, vegetation, trunks, poles, and traffic signs. As shown in Figure 1, LiDAR point cloud data with semantic information are mapped onto a voxel map with a voxel size of 1 m. Then, in each voxel, majority voting of the semantic class of the LiDAR point cloud data is selected, and the voxel semantic class is determined. Figure 2 presents an example of voxel semantic classification.

In SLAM, the use of LiDAR point cloud data related to moving objects (referred to as moving point cloud data), such as cars, two-wheelers, and pedestrians, degrades accuracy. Thus, these data are removed using an occupancy grid method, and those related to stationary objects (stationary point cloud data) are used in NDT SLAM. Semantic segmentation can detect moving objects. However, this paper focuses on loop detection using semantic information; thus, moving point cloud data are removed using the occupancy grid method.

The accuracy of NDT SLAM deteriorates over time due to accumulation errors. To reduce the error, Graph SLAM is employed [21]. Figure 3 shows a pose graph for Graph SLAM. Here, the relative poses of the vehicle, which are calculated by NDT SLAM for every LiDAR sampling period, are set to a pose graph as graph edges (the black arrows depicted in Figure 3). When loops previously visited by the vehicle are detected using the method described in Section III, the current pose of the vehicle relative to its pose at the revisit node is set to the pose

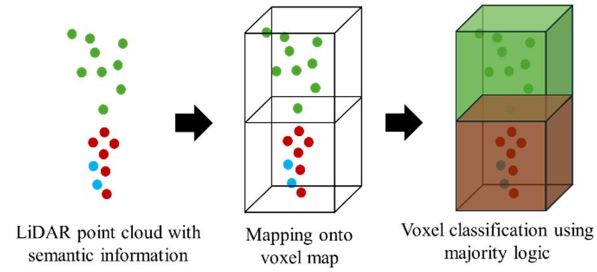

Figure 1. Flow of voxel classification using semantic information.

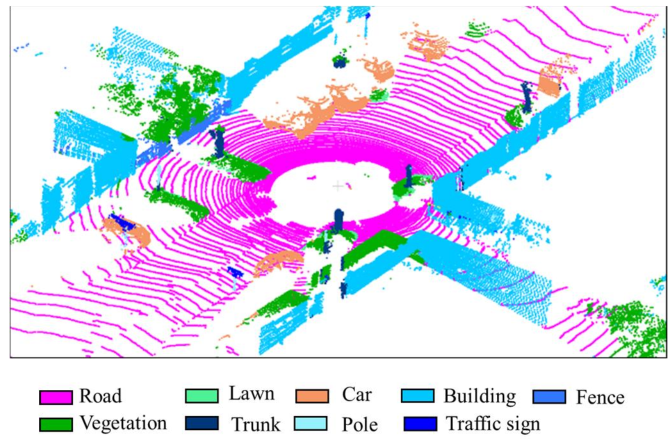

Figure 2. Example of voxel semantic classification using RangeNet++.

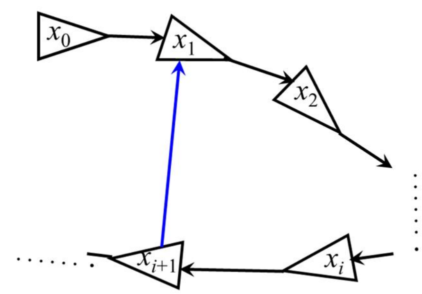

Figure 3. Pose graph. The black triangle indicates the graph node (vehicle pose), and the black and blue arrows indicate graph edges (relative poses between two neighboring nodes and loop constraint, respectively).

graph as a loop constraint (the blue arrow in Figure 3). Using the least squares method, Eq. (2) is then minimized to improve the accuracy of NDT SLAM as follows:

$$J(\boldsymbol{\chi}) = \sum_i \{(\boldsymbol{x}_{i+1} - \boldsymbol{x}_i) - \boldsymbol{\delta}_{i+1,i}\}^T \boldsymbol{\Omega}^{pose} \{(\boldsymbol{x}_{i+1} - \boldsymbol{x}_i) - \boldsymbol{\delta}_{i+1,i}\}$$
$$+ \sum_{x_A, x_B \in \mathrm{loop}} \{(\boldsymbol{x}_B - \boldsymbol{x}_A) - \boldsymbol{\delta}_{A,B}\}^T \boldsymbol{\Omega}^{loop} \{(\boldsymbol{x}_B - \boldsymbol{x}_A) - \boldsymbol{\delta}_{A,B}\} \quad (2)$$

where the first and second terms on the right side indicate the constraints on NDT SLAM and loops, respectively; $\boldsymbol{\chi} = (\boldsymbol{x}_1^T, \boldsymbol{x}_2^T, \cdots, \boldsymbol{x}_i^T, \cdots)^T$; $\boldsymbol{x}_i$ denotes the vehicle pose at the i-th time step; $\boldsymbol{\delta}_{i+1,i}$ denotes the relative pose of the vehicle between the i-th and (i+1)th time steps, which is calculated from NDT SLAM; $\boldsymbol{x}_A$ and $\boldsymbol{x}_B$ denote the vehicle poses at the loop and current nodes, respectively; $\boldsymbol{\delta}_{A,B}$ denotes the relative pose of

Courtesy of IARIA Board and IARIA Press. Original source: ThinkMind Digital Library https://www.thinkmind.org

the vehicle at the two nodes, which is calculated from the LiDAR point cloud using NDT scan matching; $\boldsymbol{\Omega}^{pose}$ and $\boldsymbol{\Omega}^{loop}$ denote the weighting matrices.

III. Loop Detection Method

A. Detection of Loop Candidates

A key component of Graph SLAM is loop detection. To this end, loop candidates are first obtained using vehicle self-location information via NDT SLAM. If the distance between an old node and the current node is less than 15 m, the old node is recognized as a loop candidate.

In our previous work [11][12], geometric surface shape features of surrounding objects were used to identify loop candidates (see Appendix A). In this paper, semantic information is used to improve the performance of selecting loop candidates. The similarity indicator (referred to as Semantic Similarity Indicator, SSI) is calculated to select loop candidates. For the SSI, six voxel semantic classes are considered: buildings, fences, vegetation, trunks, poles, and traffic signs.

Based on these classes of voxels, two feature descriptors, $Fs = (f_1, f_2, \ldots, f_6)$ and $Gs = (g_1, g_2, \ldots, g_6)$, are defined, where Fs denotes the feature descriptor, which is calculated from LiDAR point cloud data captured at loop candidates, and Gs denotes the feature descriptor, which is calculated from LiDAR point cloud data captured at the current place; f_i and g_i, $i = 1, 2, \ldots, 6$, denotes the number of the i-th semantic class. The SSI is then defined using the feature descriptors as follows:

$$SSI = \frac{\sum_{i=1}^{6}\{\max(f_i, g_i) - |f_i - g_i|\}}{\sum_{i=1}^{6}\max(f_i, g_i)} \times 100 \tag{3}$$

A higher degree of similarity between the LiDAR point cloud data at loop candidates and current places leads to a larger SSI. Thus, if the SSI is 60% or higher, the loop candidates are accepted.

B. Loop Detection and Relative Pose Calculation

Loops are determined from the loop candidates using a Point cloud Overlap Indicator (POI). From two LiDAR point cloud data captured at the current place and each loop candidate, the relative pose of the vehicle is calculated using NDT scan matching. The POI is then given by:

$$POI = \frac{1}{n}\sum_{i=1}^{n}\text{overlap}(d_i) \times 100 \tag{4}$$

where n represents the number of measurements in the LiDAR point cloud data captured at the current place of the vehicle; d_i denotes the nearest neighbor distance between the measurements in the LiDAR point cloud data captured at the current place and each loop candidate. The function overlap (d_i) is defined by

$$\text{overlap}(d_i) = \begin{cases} 1 & \text{for } d_i \le \text{threshold} \\ 0 & \text{otherwise} \end{cases} \tag{5}$$

A higher similarity between the LiDAR point cloud data captured at the current place and loop candidate leads to a smaller POI value. Thus, if the POI value is 80% or higher, the loop can be detected from the loop candidates.

In NDT scan matching, if the initial relative pose is incorrect, both the relative pose estimate and POI become inaccurate due to local minima issues. In our previous work [12], to accurately set the initial relative pose, geometric point feature histograms, FPFH, were used. In this paper, geometric and semantic point feature histograms (referred to as Semantic Point Feature Histograms, SPFH) are presented to improve the performance of setting the initial relative pose.

First, LiDAR point cloud data captured at the current place are mapped onto a voxel map (grid size of 0.2 m) in the LiDAR coordinate system and downsampled using a voxel grid filter. The centroid of the point cloud data in the i-th voxel ($i = 1, 2, \ldots$) on the voxel map is then obtained. The centroid is referred to as the feature point A_i in this paper. The geometric three-angle feature in the feature point is calculated, and geometric point feature histograms (33 dimensions in this study) are then calculated based on FPFH (see Appendix B).

In addition, a semantic feature histogram is calculated using the semantic information of the six semantic classes: buildings, fences, vegetation, trunks, poles, and traffic signs (see Section III-A).

Let A_i be the feature point in the i-th voxel and A_j be the feature point in the j-th voxel ($j = 1, 2, ..., n$) located around the i-th voxel. Here, semantic information is assigned to each feature point, which is classified as a voxel semantic class using the voxel classification method shown in Figure 1.

By obtaining the semantic class of the feature point A_i and the semantic classes of the n feature points ($A_1, A_2, \cdots, A_n$) around A_i, a six-dimensional semantic feature histogram, which is the ratio of each semantic class of A_i to the n feature points, is calculated. Here, n represents the number of voxels within a radius of 2 m from the i-th voxel. The semantic feature histogram of A_i is referred to as Simplified Semantic Histograms (SSH) of A_i, $\boldsymbol{SSH}(A_i)$. Similarly, $\boldsymbol{SSH}(A_j)$ is calculated for the feature point A_j ($j = 1, 2, ..., n$) around A_i.

The six-dimensional Semantic Histogram (SH) related to A_i is then given by

$$\boldsymbol{SH}(A_i) = \boldsymbol{SSH}(A_i) + \frac{1}{n}\sum_{j=1}^{n} w_j \boldsymbol{SSH}(A_j) \tag{6}$$

where the weight w_i is given as the inverse number of the distance between A_i and A_j.

The six-dimensional semantic feature histogram is combined with the 33-dimensional geometric feature histogram using FPFH. The 39-dimensional point feature histogram (referred to as Semantic Fast Point Feature Histogram, SFPFH) is then used to accurately set the initial relative pose.

From the LiDAR point cloud data captured at each loop candidate, the feature point B_i and the related SFPFH are obtained in the same way. Their feature points A_i and B_i are matched using the 3PCS method [12] as follows:

Step 1: Three feature points A_i ($i = 1, 2, 3$) are randomly extracted from the set of feature points obtained at the current location, and a triangle $\tilde{A}$ is composed of the three feature points A_1, A_2, and A_3. Then, 100 feature points B_j ($j = 1, 2, \ldots,$

Courtesy of IARIA Board and IARIA Press. Original source: ThinkMind Digital Library https://www.thinkmind.org

100) with similar SFPFH as those of A_i (i = 1, 2, 3) are extracted from the set of feature points obtained at each loop candidate using the k-nearest neighbor method. A triangle $\tilde{B}$ is composed of any three feature points from 100 feature points B_j. The three feature points B_1, B_2, and B_3 are selected such that the two triangles $\tilde{A}$ and $\tilde{B}$ are congruent.

Step 2: The pose of the loop candidate relative to the current place is denoted by $\delta \boldsymbol{x} = (\delta x, \delta y, \delta z, \delta\phi, \delta\theta, \delta\psi)^T$, where $(\delta x, \delta y, \delta z)$ and $(\delta\phi, \delta\theta, \delta\psi)$ denote the relative position and attitude angle, respectively.

In the matched triangles $\tilde{A}$ and $\tilde{B}$, the centroid positions of the three-feature point sets (A_1, A_2, A_3) and (B_1, B_2, B_3) are denoted by $\bar{\boldsymbol{a}}$ and $\bar{\boldsymbol{b}}$, respectively. The positions of the feature points A_i and B_i, where i = 1, 2, 3, are denoted by $\boldsymbol{a}_i^*$ and $\boldsymbol{b}_i^*$, respectively. The feature point matrices are then given by $\delta\boldsymbol{a} = (\delta\boldsymbol{a}_1, \delta\boldsymbol{a}_2, \delta\boldsymbol{a}_3)^T$ and $\delta\boldsymbol{b} = (\delta\boldsymbol{b}_1, \delta\boldsymbol{b}_2, \delta\boldsymbol{b}_3)^T$, where $\delta\boldsymbol{a}_i \triangleq \boldsymbol{a}_i^* - \bar{\boldsymbol{a}}$ and $\delta\boldsymbol{b}_i \triangleq \boldsymbol{b}_i^* - \bar{\boldsymbol{b}}$. Based on the matrices $\boldsymbol{W}_1$ and $\boldsymbol{W}_2$, which are defined by the singular value decomposition ($\boldsymbol{H} = \boldsymbol{W}_1 \boldsymbol{\Sigma} \boldsymbol{W}_2^T$) of the matrix $\boldsymbol{H} = \delta\boldsymbol{b} \cdot \delta\boldsymbol{a}^T$, the homogeneous matrix related to the relative pose $\delta\boldsymbol{x}$ is given by

$$\boldsymbol{T}(\delta\boldsymbol{x}) = \begin{pmatrix} \boldsymbol{W}_2 \boldsymbol{W}_1^T & \bar{\boldsymbol{a}} - \boldsymbol{R}\bar{\boldsymbol{b}} \\ 0 & 1 \end{pmatrix} \tag{7}$$

where $\boldsymbol{R}$ represents the rotational matrix related to $(\delta\phi, \delta\theta, \delta\psi)$.

The position of the i-th feature point A_i (i = 1, ..., n_A) in the feature point set A is denoted by $\boldsymbol{a}_i$, and that of the j-th feature point B_j (j = 1, ..., n_B) in the feature point set B is denoted by $\boldsymbol{b}_j$. The distance r_j between $\boldsymbol{b}_j$ and its nearest neighbor feature point $\boldsymbol{a}_i$ is then calculated by

$$r_j = \left\{ \begin{pmatrix} \boldsymbol{a}_i \\ 1 \end{pmatrix} - \boldsymbol{T}(\delta\boldsymbol{x}) \begin{pmatrix} \boldsymbol{b}_j \\ 1 \end{pmatrix} \right\}^T \left\{ \begin{pmatrix} \boldsymbol{a}_i \\ 1 \end{pmatrix} - \boldsymbol{T}(\delta\boldsymbol{x}) \begin{pmatrix} \boldsymbol{b}_j \\ 1 \end{pmatrix} \right\} \tag{8}$$

Step 3: Steps 1 and 2 are repeated 100 times to find the relative pose $\delta\boldsymbol{x}$ with the largest value in the following cost function:

$$J = \frac{1}{n_B} \sum_{j=1}^{n_B} \text{overlap}(r_j) \tag{9}$$

where overlap (r_i) denotes the overlap function defined in (5).

The relative pose $\delta\boldsymbol{x}$ is then obtained. In NDT scan matching, the relative pose $\delta\boldsymbol{x}$ is used as the initial value, and an iterative calculation is performed. Therefore, the accurate relative pose is calculated, and the POI in (4) can be obtained accurately.

IV. Fundamental Experiments

A. Dataset

The Semantic KITTI dataset [19] is used to evaluate the performance of the proposed method. In the KITTI dataset, a mechanical 64-layer LiDAR (Velodyne HDL-64E) is mounted on a vehicle. The horizontal field of view of the LiDAR is 360° with an angular resolution of 0.08°, and the vertical field of view is 26.8° with an angular resolution of 0.42°. The LiDAR sampling period is 0.1 s, where the laser beam makes one rotation in the horizontal direction. The LiDAR obtains approximately 120,000 point cloud data points during the sampling period. Each observation point has information about its 3D position and reflection intensity.

In the KITTI dataset, 11 sequences (sequences 00–10) containing true semantic information, are used in this study. Four sequences (sequences 00, 02, 05, and 08), which have many loops, are used to evaluate the proposed method. Therefore, cross-validation is performed for the four sequences; thus, when sequence 00 is used for evaluation data, sequences 01–10 are used as training data, when sequence 02 is used for evaluation data, sequences 00, 01, and 03–10 are used as training data, and so on. The distances traveled by the vehicle in sequences 00, 02, 05, and 08 are 3.7, 5.0, 2.2, and 3.2 km, respectively.

B. Performance of Object Recognition by RangeNet++

The recognition performance of RangeNet++ is evaluated. Table I shows the accuracy (Intersection over Union (IoU), precision, and recall) for 12 semantic classes. As shown in the table, accuracy tends to be high for large objects, such as cars, roads, buildings, and vegetation, whereas it decreases for small objects, such as people and traffic signs.

For the six sematic voxel classes used in the loop detection method, including buildings, fences, vegetation, trunks, poles, and traffic signs, the average IoU, precision, and recall aree 58.6%, 73.7%, and 72.1%, respectively.

C. Performance of Loop Detection

The performance of SSI and SFPFH in loop detection is evaluated. First, a dataset of pairs of loops and current places with a relative distance of α m is generated from the KITTI dataset; these pairs should be detected accurately as true loops. The relative distance is set at $0 \le \alpha \le 5$ m and $5 < \alpha \le 10$ m. In addition, a dataset of pairs of loops and current places with a relative distance $\alpha \ge 300$ m is generated; these pairs should be detected as false loops.

The performance of loop detection is then evaluated using the true and false loop datasets. If a true loop is determined to be a loop, it is considered a correct loop detection; if a true loop is determined not to be a loop, it is considered a miss loop detection; if a false loop is considered a loop, it is considered a false loop detection.

First, the performance of loop candidate detection is evaluated in terms of the SSI. The precision and recall results of loop candidate detection are shown in Table II. For comparison, the results of loop candidate detection using the conventional geometric method (Geometric Similarity Indicator, GSI) [12]

TABLE I. PERFORMACE OF OBJECT CLASSIFICATION USING RANGENET++

Class	IoU [%]	Precision [%]	Recall [%]
Car	89.5	91.4	97.7
Two-wheeler	43.6	63.1	58.6
Other vehicles	40.8	69.1	49.9
Person	22.8	52.8	28.7
Road	94.2	97.9	96.1
Lawn	65.4	81.0	77.4
Building	84.5	90.9	92.5
Fence	56.1	73.2	70.6
Vegetation	80.5	88.1	90.3
Trunk	53.1	68.5	70.2
Pole	40.1	51.5	64.5
Traffic sign	37.4	69.9	44.5

Courtesy of IARIA Board and IARIA Press. Original source: ThinkMind Digital Library https://www.thinkmind.org

TABLE II. PERFORMANCE OF LOOP CANDIDATE DETECTION IN TERMS OF SSI AND GSI

Sequence	Recall		Precision
	$0 \le \alpha \le 5$ m	$5 < \alpha \le 10$ m	
00	99.7 (82.6)	98.8 (75.6)	64.0 (54.1)
02	99.9 (67.9)	99.4 (62.8)	62.5 (52.9)
05	98.2 (80.7)	98.9 (79.7)	53.5 (49.9)
08	100 (78.3)	99.4 (72.9)	61.3 (52.0)

The performance evaluation in terms of conventional GSI is shown in brackets.

TABLE III. PERFORMANCE OF LOOP DETECTION IN TERMS OF SFPFH AND FPFH

Sequence	$0 \le \alpha \le 5$ m	$5 < \alpha \le 10$ m
00	96.2 (94.3)	71.0 (65.7)
02	89.9 (85.3)	59.8 (58.0)
05	92.5 (92.7)	67.0 (65.2)
08	89.2 (77.8)	74.8 (57.1)

The performance evaluation in terms of conventional FPFH is shown in brackets.

(Appendix A) are also shown in the table. The higher the precision value, the fewer the incorrectly detected loop candidates, and the higher the recall value, the fewer the falsely extracted loop candidates. As shown in the table, the proposed SSI provides higher loop candidate extraction performance than the conventional GSI.

Next, the performance of loop detection is evaluated in terms of using SFPFH. The Matching Success Score (MSS) is defined as follows:

$$MSS = \frac{1}{n}\sum_{i=1}^{n} f(POI_i) \times 100 \qquad (10)$$

where n represents the number of true loop pair; POI_i denotes the POI of the i-th pair. The function $f(POI_i)$ is defined by

$$f(POI_i) = \begin{cases} 1 & \text{for } POI_i \le \text{threshold} \\ 0 & \text{otherwise} \end{cases} \qquad (11)$$

Higher loop detection accuracy from loop candidates leads to a larger *MSS*. The result is shown in Table III. For comparison, the results obtained using the conventional geometric method (FPFH) are also shown in the table. The results show that the proposed method (SFPFH) provides higher loop detection performance than the conventional method (FPFH).

D. SLAM Performance

Figures 4 and 5 show environment maps of sequence 00 constructed by SLAM using the proposed and conventional geometric methods, respectively. Figure 6 shows the vehicle movement path estimated by SLAM. As an enlarged map shown in Figure 5, the conventional method distorts the environment map because of miss detections of loops, whereas the proposed method does not cause distortion, as shown in Figure 4. In addition, in the area surrounded by the pink frame in Figure 6, the conventional method has a large error in vehicle self-pose estimation, whereas the proposed method achieves accurate estimation of vehicle self-pose.

Figure 7 shows an image of a location where distortion in the environment map occurs using the conventional method. The image contains many parked cars and the surface features of the cars are all similar; thus, incorrect loops are detected using only the conventional FPFH. This is why distortion occurs when using the conventional method. However, in such an environment, the proposed SFPFH can accurately detect loops.

Next, the following three evaluation values are used to evaluate SLAM performance in sequences 00, 02, 05, and 08:

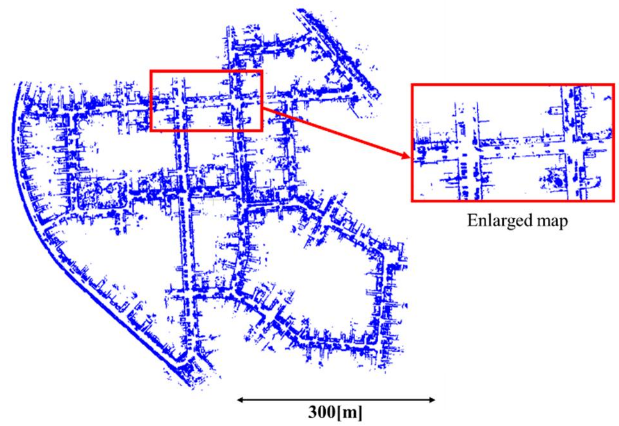

Figure 4. Environment map built using proposed method.

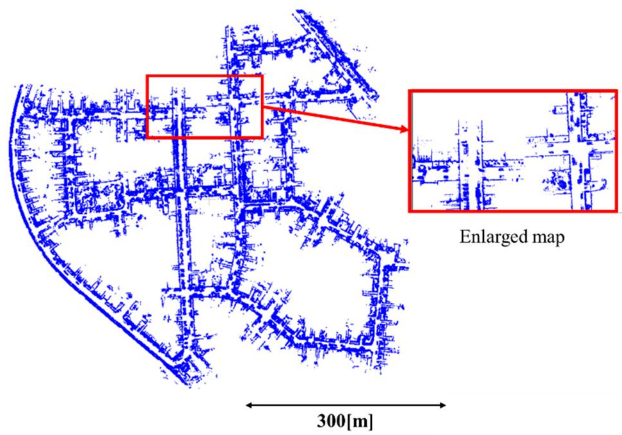

Figure 5. Environment map built using conventional method.

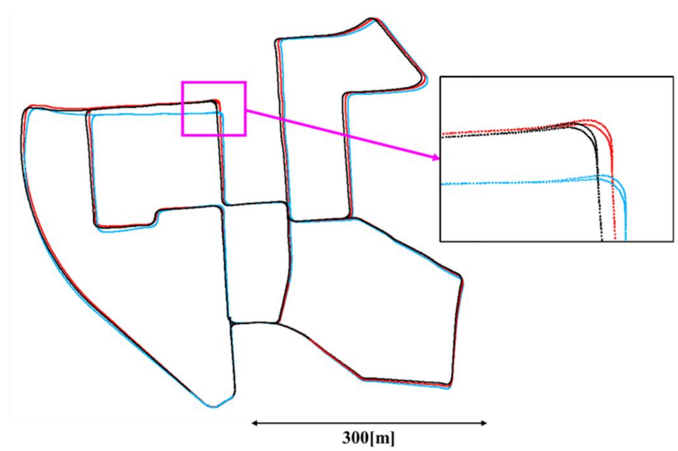

Figure 6. Vehicle movement path estimated using SLAM. The black line indicates the ground truth. The red and light blue lines indicate the results obtained using proposed and conventional methods, respectively.

Courtesy of IARIA Board and IARIA Press. Original source: ThinkMind Digital Library https://www.thinkmind.org

Figure 7. Photo of area surrounded by the red frame in Figures 4 and 5.

TABLE IV. SLAM PERFORMANCE

Sequence	ATE [m]	NLD	MELC [%]
00	3.19 (6.92)	1030 (889)	9.6 (18.0)
02	38.62 (94.14)	334 (213)	51.6 (68.0)
05	3.75 (4.55)	594 (575)	23.5 (24.3)
08	11.05 (11.63)	458 (424)	12.1 (17.5)

The performance evaluation using the conventional geometric method is shown in brackets.

- Absolute Trajectory Error (ATE): Root-Mean-Square (RMS) error of estimate of vehicle self-position
- Number of Loop Detection (NLD)
- Miss Extraction rate of Loop Candidates (MELC)

The results are shown in Table IV. The proposed method achieves a smaller ATE, larger NLD, and smaller MELC than the conventional method, which demonstrates its superior SLAM performance improvement.

V. CONCLUSION AND FUTURE WORK

This paper presented a method for improving loop detection performance using semantic information in LiDAR SLAM. Semantic information about the surrounding environment was recognized using RangeNet++, and the SSI and SFPFH were introduced to improve the accuracy of loop detection in NDT-Graph SLAM. Experiments using the Semantic KITTI dataset were conducted to evaluate the performance of the proposed method compared with our previous geometry-based loop detection method.

This paper focused on applying semantic information to loop detection in Graph SLAM. Currently, we are applying semantic information to NDT SLAM in conjunction with Graph SLAM. In addition, semantic information will be applied to map updates and maintenance in the future.

ACKNOWLEDGMENT

This study was partially supported by the KAKENHI Grant #23K03781, the Japan Society for the Promotion of Science (JSPS).

APPENDIX A: GEOMETRY BASED DETECTION OF LOOP CANDIDATES

Loop candidates are detected based on a Geometric Similarity Indicator (GSI) [11][12], which is calculated using LiDAR point cloud data captured at the loop candidate and current place of the vehicle. LiDAR point cloud data are mapped onto the voxel map (grid size of 1 m). Each grid of the voxel map is first classified into three types: line, plane, or other voxels (Figure A). Three eigenvalues ($\lambda_1 \geq \lambda_2 \geq \lambda_3 \geq 0$) are calculated from LiDAR point cloud data in voxels based on principal component analysis, and the following features are calculated:

$$r_1 = \frac{\sqrt{\lambda_1} - \sqrt{\lambda_2}}{\sqrt{\lambda_1}},\ r_2 = \frac{\sqrt{\lambda_2} - \sqrt{\lambda_3}}{\sqrt{\lambda_1}},\ r_3 = \frac{\sqrt{\lambda_3}}{\sqrt{\lambda_1}} \tag{A}$$

When the maximum values are r_1, r_2, and r_3, the voxel is determined as being of line, plane, or other types. Based on the surface normal vector of the plane voxels, the plane voxels are further divided into nine classes which are different directions of normal vectors.

The two feature descriptors $\boldsymbol{A} = (a_1, a_2, \cdots, a_{11})^T$ and $\boldsymbol{B} = (b_1, b_2, \cdots, b_{11})^T$ are defined. $\boldsymbol{A}$ is calculated from LiDAR point cloud data captured at loop candidates, and $\boldsymbol{B}$ is calculated from the LiDAR point cloud data at the current place. a_1 and b_1 denote the numbers of line voxels in the voxel map. $a_2 - a_{10}$ and $b_2 - b_{10}$ denote the numbers of plane voxels divided into nine classes. a_{11} and b_{11} denote the numbers of other voxels.

From the feature descriptors $\boldsymbol{A}$ and $\boldsymbol{B}$, the GSI is given by

$$GSI = \frac{\sum_{i=1}^{11} \{\max(a_i, b_i) - |a_i - b_i|\}}{\sum_{i=1}^{11} \max(a_i, b_i)} \tag{B}$$

Among loop candidates, loops with large GSI values can be accepted.

LiDAR point cloud data are sparse in the vertical direction of the mechanical LiDAR; thus, voxels located far from LiDAR have fewer points in the voxel. This reduces the classification accuracy of surface shape features. To solve this problem, when voxels are located far from LiDAR (35 m or more in this study), adjacent voxels are combined, and all point cloud data of the combined voxels are used for principal component analysis.

APPENDIX B: FPFH FOR GEOMETRIY BASED LOOP DETECTION

Let $\boldsymbol{a}_i$ be the position of feature point A_i in the i-th voxel and $\boldsymbol{a}_j$ be the position of feature point A_j in the j-th voxel around the i-th voxel. As shown in Figure B, Let $\boldsymbol{n}_i$ and $\boldsymbol{n}_j$ be the normal vectors of these feature points and $(\boldsymbol{a}_j - \boldsymbol{a}_i)$ be the difference vector of feature point positions. Using these vectors, the

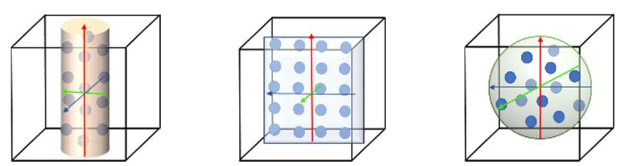

(a) Line (b) Plane (c) Other

Figure A. Voxel classification.

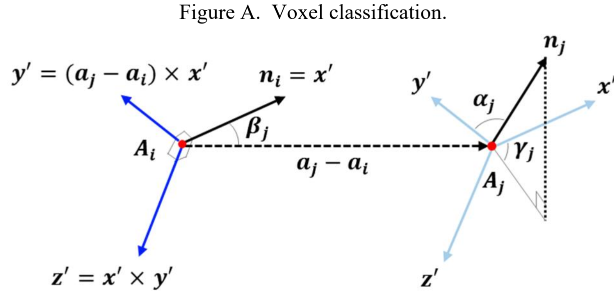

Figure B. Angle features.

Courtesy of IARIA Board and IARIA Press. Original source: ThinkMind Digital Library https://www.thinkmind.org

angular feature (α_j, β_j, γ_j) is defined by $\alpha_j = \boldsymbol{y}' \cdot \boldsymbol{n}_j$, $\beta_j = \boldsymbol{x}' \cdot (\boldsymbol{a}_j - \boldsymbol{a}_i)$,and $\gamma_j = \arctan(\boldsymbol{z}' \cdot \boldsymbol{n}_j / \boldsymbol{x}' \cdot \boldsymbol{n}_j)$.

By obtaining the angle features of the n feature points (A_1, $A_2, \cdots, A_n$) around A_i, a set of angle features is defined. The set is referred to as the Simplified Point Feature Histograms of A_i ($\boldsymbol{SPFH}(A_i)$). Here, n represents the number of voxels that exist within a radius of 2 m from the i-th voxel. Similarly, $\boldsymbol{SPFH}(A_j)$ is calculated for the feature point A_j (j = 1, 2, ..., n). The 33-dimensional point feature histograms related to A_i ($\boldsymbol{FPFH}(A_i)$) are then given by [9]

$$\boldsymbol{FPFH}(A_i) = \boldsymbol{SPFH}(A_i) + \frac{1}{n}\sum_{j=1}^{n} w_j \boldsymbol{SPFH}(A_j) \qquad \text{(C)}$$

where the weight w_i denotes the inverse number of the distance between A_i, and A_j.

REFERENCES

[1] J. Zhao et al., “Autonomous Driving System: A Comprehensive Survey,” Expert Systems with Applications 242, pp. 1–27, 2023.

[2] Y. Fu, C. Li, F. R. Yu, T. H. Luan, and Y. Zhang, “A Survey of Driving Safety with Sensing, Vehicular Communications, and Artificial Intelligence-Based Collision Avoidance,” IEEE Trans. on Intelligent Transportation Systems, Vol. 23, Issue 7, pp. 6142–6163, 2022.

[3] G. Bresson, Z. Alsayed, L. Yu, and S. Glaser, “Simultaneous Localization and Mapping: A Survey of Current Trends in Autonomous Driving,” IEEE Trans. on Intelligent Vehicles, Vol. 2, Issue 3, pp. 194–220, 2017.

[4] E. Arnold, et al., “A Survey on 3D Object Detection Methods for Autonomous Driving Applications,” IEEE Trans. on Intelligent Transportation Systems, Vol. 20, Issue 10, pp. 3782–3795, 2019.

[5] Y. Li, et al., “A Review of Simultaneous Localization and Mapping Algorithms Based on Lidar,” World Electric Vehicle J., 2025, 16(2), pp. 1–29, 2025.

[6] Z. Wang, Y. Shen, B. Cai, and M. T. Saleem, “A Brief Review on Loop Closure Detection with 3D Point Cloud,” Proc. 2019 IEEE Int. Conf. on Real-time Computing and Robotics, pp. 929–934, 2019.

[7] F. Martín, R. Triebel, L. Moreno, and R. Siegwart, “Two Different Tools for Three-Dimensional Mapping: DE-based Scan Matching and Feature-Based Loop Detection,” Robotica, Vol. 32, pp. 19–41, 2017.

[8] M. Magnusson, H. Andreasson, A. Nüchter, and A. J. Lilienthal, "Automatic Appearance-Based Loop Detection from 3d Laser Data Using the Normal Distributions Transform," J. of Field Robotics, Vol. 26, Issue 11-12, pp. 892–914, 2009.

[9] R. B. Rusu, N. Blodow, and M. Beetz, “Fast Point Feature Histograms (FPFH) for 3D Registration,” Proc. IEEE Int. Conf. on Robotics and Automation, pp. 3212–3217, 2009.

[10] B. Steder, R. B. Rusu, K. Konolige, and W. Burgard, “Point Feature Extraction on 3D Range Scans Taking into Account Object Boundaries,” Proc. 2011 IEEE Int. Conf. on Robotics and Automation, pp. 1–8, 2011.

[11] S. Tanaka, C. Koshiro, M. Yamaji, M. Hashimoto, and K. Takahashi, “Point Cloud Mapping and Merging in GNSS-Denied and Dynamic Environments Using Only Onboard Scanning LiDAR,” Int. J. on Advances in Systems and Measurements, Vol. 13, No. 3&4, pp. 275–288, 2020.

[12] R. Nakamura, T. Kambe, M. Hashimoto, and K. Takahashi, “SLAM-based Mapping in Truck-and-Robot System for Last-Mile Delivery Automation,” Proc. the 2023 IARIA Annual Congress on Frontiers in Science, Technology, Services, and Applications, pp. 31–37, 2023.

[13] L. Wang and Y. Huang, “A Survey of 3D Point Cloud and Deep Learning-Based Approaches for Scene Understanding in Autonomous Driving,” IEEE Intelligent Transportation Systems Magazine, Vol. 14, Issue 6, pp. 135–154, 2022.

[14] S. Arshad and G. W. Kim, “Role of Deep Learning in Loop Closure Detection for Visual and Lidar SLAM: A Survey,” Sensors, 2021, 21, 1243, 2021.

[15] L. Li, X. Kong, X. Zhao, T. Huang, and Y. Liu, “Semantic Scan Context: A Novel Semantic-Based Loop-Closure Method for LiDAR SLAM,” Autonomous Robots, Vol. 46, pp. 535–551, 2022.

[16] Y. Fan, et al., “A Semantic-Based Loop Closure Detection of 3D Point Cloud,” Proc. 2021 IEEE Int. Conf. on Robotics and Biomimetics, 2021.

[17] A. Milioto, I. Vizzo, J. Behley, and C. Stachniss, “RangeNet++: Fast and Accurate LiDAR Semantic Segmentation,” Proc. 2019 IEEE/RSJ Int. Conf. on Intelligent Robots and Systems, 2019.

[18] A. Jhaldiyal and N. Chaudhary, “Semantic Segmentation of 3D LiDAR Data Using Deep Learning: A Review of Projection-Based Methods,” Applied Intelligence, 2022.

[19] J. Behley et al., “SemanticKITTI: A Dataset for Semantic Scene Understanding of LiDAR Sequences,” Proc. the IEEE/CVF Int. Conf. on Computer Vision (ICCV), pp. 9297–9307, 2019.

[20] R. Nakamura, I. Inaga, M. Hashimoto, and K. Takahashi, “SLAM-Based Mapping Using Micromobility-Mounted Solid-State LiDAR,” Proc. the 11th IIAE Int. Conf. on Intelligent Systems and Image Processing, pp. 93–100, 2024.

[21] G. Grisetti, R. Kümmerle, C. Stachniss, and W. Burgard, “A Tutorial on Graph-Based SLAM,” IEEE Intelligent Transportation Systems Magazine, Vol. 2, Issue 4, pp. 31–43, 2010.

Courtesy of IARIA Board and IARIA Press. Original source: ThinkMind Digital Library https://www.thinkmind.org